université de BORDEAUX

eman ta zabal zazu
Universidad del País Vasco
Euskal Herriko Unibertsitatea

DOCTORAL THESIS

EXPERIMENTAL AND THEORETICAL INVESTIGATION OF STRONG ACID HYDRATES

by

Sophie ESPERT

Under the supervision of
Daniel SANCHEZ-PORTAL and Arnaud DESMEDT

2023

Research units

Centro de Fisica de Materiales – Universidad del Pais Vasco

Paseo Manuel de Lardizabal, 5

E 20018 Donostia/San Sebastian ESPANA

Institut des Sciences Moléculaires – Université de Bordeaux CNRS UMR 5255
Bâtiment A12, 351 cours de la libération
33405 TALENCE cedex FRANCE

Abstract of the thesis in English

Designing new devices dedicated to energy storage and production is at the center of nowadays concerns. Strong acid clathrate hydrates represent an opportunity as new electrolytes for fuel cells, for which fundamental questions remain open. The most striking property in strong acids hydrates is their super-protonic conductivity due to the abnormal protons mobility in the host water substructure. To get insight into the conductivity mechanism, we have combined experimental and theoretical approaches to study the cases of $HClO_4$ and HPF_6 hydrates – both systems being among the best conductors. Two issues have been addressed: the localisation of the ionic impurities in the clathrate structures and their role in the protonic conductivity as a function of their concentration.

Regarding the HPF_6 hydrates, due to the reactivity of the hexafluorophosphoric anions with water, the existence of impurities in hydrates (e.g., H_3PO_4) is expected. In previous work, the presence of such impurities has been identified using Raman spectroscopy and NMR. Impedance measurements reveal the importance of these impurities in the proton conductivity. Thus, localising these impurities at the molecular scale is a fundamental question for improving the electrolytic properties of strong acid hydrates. Are these impurities located inside the hydrate cages or outside the structure? Here, quantum mechanical calculations at the level of the density functional theory (DFT) are used to investigate this issue. The stability of various impurities at low concentrations is investigated for strong acid hydrates. It was necessary to perform several tests to select the appropriate computational parameters, including the most appropriate DFT functional. Once the DFT parameters were set, relaxation calculations were performed on the HPF_6 hydrate system. The calculations reveal that the HPF_6 hydrate is stabilized by the inclusion of H_3PO_4, HPO_2F_2 or H_2PO_3F impurities within the hydrate structure. These theoretical results, together with existing Raman scattering and conductivity measurements, confirm the role played by ionic defects on this system and its proton mobility.

To better understand the role played by the acid concentration on the protonic conductivity, it is possible to prepare mixed hydrates (i.e., encapsulating two guest species) by co-including

HClO4 acid and tetrahydrofuran (THF) molecules (THF hydrate is a prototypical clathrate hydrate, widely investigated). By varying the THF to HClO4 ratio, such mixed hydrates offer the opportunity to control the concentration of the acidic defects in the hydrate structure. Here the important role played by the acid concentration is investigated by combining X-Ray diffraction and Raman imaging. By X-Ray diffraction, the mixed hydrate structures were identified as a function of their acid fraction and temperature. Their temperature stability was studied and revealed an unexpected behaviour for the hydrate structures. The modification of the hydrate melting temperature might be explained by the possible co-inclusion of HClO4 and THF in so-called type SI structure. To our knowledge, this would be the first observation of the encapsulation of THF in SI structure. Raman imaging is used to study the distribution of the various phases at the micro-scale in the mixed hydrate, highlighting the heterogeneity of the samples. The impedance measurements on the mixed THF/HClO4 hydrates showed that the protonic conductivity is controlled not only by the ionic defect concentration, but also by the formed hydrate structure and the mesoscopic organisation within the sample as revealed by X-ray diffraction analysis and Raman imaging.

Understanding the influence of the hydrate structure on the proton conductivity and the mechanisms involved in forming acid hydrates will be crucial to open the possibility of using hydrates in decarbonised energy applications. The present Thesis project is a contribution towards this aim.

Resumen del Tesis en Castellano

El diseño de nuevos dispositivos dedicados a la producción y almacenamiento de energía es una de las principales preocupaciones en la actualidad. Los clatratos de ácidos fuertes representan una oportunidad única para ser utilizados como nuevos electrolitos en pilas de combustible. Sin embargo, antes de que esto sea posible, muchas de las propiedades de estos hidratos todavía deben ser entendidas. Sin duda la más importante en este contexto es su gran conductividad protónica, asociada a la movilidad anómala de los protones en la subestructura de agua. En esta tesis, para profundizar en los mecanismos detrás de dicha alta conductividad, hemos combinado técnicas experimentales y teóricas para estudiar los hidratos de $HClO_4$ and HPF_6, ambos sistemas se cuentan entre los de mayor conductividad. Dos problemas se han estudiado: la localización de impurezas iónicas en la estructura de los clatratos y su papel en la conductividad protónica en función de su concentración.

Debido a la reactividad del ácido hexafluorofosfórico con el agua, la existencia de numerosas impurezas (e.g., H_3PO_4) en dichos hidratos de HPF_6 es esperable. En la literatura, encontramos algunos estudios en los que la presencia de estas impurezas fue identificada utilizando espectroscopia Raman y NMR. Además, las medidas de impedancia electroquímica revelaron su importancia en la conductividad protónica del material. Por tanto, identificar con precisión la localización de las impurezas en la estructura es una cuestión central para entender y mejorar las propiedades electroquímicas de los hidratos de ácidos fuertes. La pregunta fundamental es si las impurezas se encuentran dentro de las cajas del clatrato o fuera de la estructura. En esta tesis hemos utilizado cálculos mecánico cuánticos al nivel de la teoría del funcional de la densidad (DFT) para investigar la estabilidad de varias impurezas en bajas concentraciones. Para ello debimos primero identificar los parámetros computacionales que nos permitan reproducir de forma adecuada la estructura y propiedades del hidrato de HPF_6. En particular, hemos estudiado diversos funcionales DFT. Nuestros cálculos revelan que el hidrato de HPF_6 resulta más estable cuando pequeñas concentraciones de impurezas como H_3PO_4, $H_2PO_2F_2$ o H_3PO_3F se encapsulan en la estructura. Estos resultados teóricos, junto con los datos existentes de espectroscopia Raman y de conductividad, sirven para confirmar el papel clave que juegan los defectos iónicos en estos sistemas y en su movilidad protónica.

Para mejorar nuestra compresión del papel de la concentración de ácido en la conductividad protónica, en esta tesis decidimos estudiar hidratos mixtos (i.e., que encapsulan dos especies distintas) de $HClO_4$ y tetrahidrofurano (THF) (el hidrato de THF forma un clatrato prototípico, que ha sido investigado ampliamente). Cambiando la concentración relativa de THF y $HClO_4$ podemos controlar la concentración del ácido sin cambiar la ocupación global de las cajas de la estructura. El estudio se realiza combinando las técnicas de difracción de rayos-X y microscopía Raman (medidas Raman con resolución espacial micrométrica). Los rayos-X nos permiten identificar la estructura del hidrato en función de la fracción ácida y la temperatura. En particular, observamos una dependencia con la temperatura con un comportamiento inesperado, distinto de otros hidratos. La peculiar modificación de la temperatura de fusión del hidrato puede explicarse por la captura simultanea de $HClO_4$ y THF en la estructura tipo SI. De hecho, hasta donde conocemos, la nuestra podría ser la primera observación de la encapsulación de THF en la estructura SI. La microscopía Raman se utiliza para estudiar la distribución de las varias fases en la escala micrométrica en nuestro hidrato mixto, revelando la heterogeneidad de las muestras. Las medidas de impedancia electroquímica en los hidratos mixtos de THF/$HClO_4$ demuestran que la conductividad protónica no solo depende de la concentración de ácido, sino también en la estructura del hidrato y su organización mesoscópica en las muestras, tal como se deduce al tener al correlacionar estos datos con la difracción de rayos-X y la microscopía Raman.

Entender la influencia de la estructura del hidrato en la conductividad protónica, y en la formación y estabilidad de los hidratos de ácidos fuertes es necesario para poder usar estos sistemas en pilas de combustible y otras tecnologías descarbonizadas. La presente tesis doctoral es una contribución hacia este ambicioso objetivo.

Résumé de la thèse en Français

Le stockage et la production d'énergie sont au centre des préoccupations actuelles. Les clathrates hydrates d'acides forts représentent une opportunité pour les piles à combustible, pour lesquelles des questions fondamentales restent ouvertes. Une des propriétés majeures des hydrates d'acides forts est leur super-conductivité protonique, due à la mobilité anormale des protons dans la structure de l'hydrate. Afin de mieux comprendre les mécanismes de conductivité, nous avons combiné des approches expérimentales et théoriques pour étudier les hydrates $HClO_4$ et HPF_6^- ; ces deux systèmes étant parmi les meilleurs conducteurs. Deux questions ont été abordées : la localisation des impuretés ioniques dans les structures des clathrates et leur rôle dans la conductivité protonique.

En ce qui concerne les hydrates de HPF_6, en raison de la réactivité des anions hexafluorophosphoriques, l'existence d'impuretés est attendue (par exemple, H_3PO_4). Dans des travaux précédents, la présence des impuretés a été identifiée par la spectroscopie Raman et la RMN. Les mesures d'impédance révèlent l'importance de ces impuretés dans la conductivité protonique. Ainsi, la localisation de ces impuretés à l'échelle moléculaire est une question fondamentale pour améliorer les propriétés électrolytiques des hydrates d'acides. Des calculs de mécanique quantique au niveau de la théorie fonctionnelle de la densité (DFT) sont utilisés ici afin d'étudier la stabilité de diverses impuretés à de faibles concentrations pour les hydrates d'acides forts. Il a été nécessaire d'effectuer plusieurs tests pour sélectionner les paramètres de calcul appropriés, y compris pour la fonctionnelle DFT. Une fois les paramètres DFT définis, des calculs de relaxation ont été effectués sur le système d'hydrates HPF_6. Les calculs révèlent que l'hydrate HPF_6 est stabilisé par l'inclusion d'impuretés H_3PO_4, HPO_2F_2 ou H_2PO_3F dans la structure de l'hydrate. Ces résultats théoriques, ainsi que les mesures de diffusion Raman et de conductivité existantes, confirment le rôle joué par les défauts ioniques sur ce système et sa mobilité protonique.

Pour mieux comprendre le rôle joué par la concentration d'acide sur la conductivité protonique, il est possible de préparer des hydrates mixtes (c'est-à-dire encapsulant deux espèces invitées) en co-incluant de l'acide $HClO_4$ et des molécules de tétrahydrofurane (THF)

(l'hydrate de THF est un hydrate clathrate prototypique, largement étudié). En faisant varier le rapport THF/$HClO_4$, ces hydrates mixtes offrent la possibilité de contrôler la concentration des défauts acides dans la structure de l'hydrate. Nous étudions ici le rôle important joué par la concentration en acide en combinant la diffraction des rayons X et l'imagerie Raman. Par diffraction des rayons X, les structures d'hydrates mixtes ont été identifiées en fonction de leur fraction acide et de la température. Leur stabilité en température a été étudiée et a révélé un comportement inattendu pour les structures d'hydrates. La modification de la température de fusion de l'hydrate pourrait être expliquée par la co-inclusion possible de $HClO_4$ et de THF dans une structure dite de type SI. A notre connaissance, il s'agirait de la première observation de l'encapsulation du THF dans une structure SI. L'imagerie Raman utilisée pour étudier la distribution des différentes phases à l'échelle micro, met en évidence l'hétérogénéité des échantillons. Les mesures d'impédance sur l'hydrate mixte THF/$HClO_4$ ont montré que la conductivité protonique est contrôlée par la concentration des défauts ioniques, mais aussi par la structure de l'hydrate formé et l'organisation mésoscopique au sein de l'échantillon.

Comprendre l'influence de la structure de l'hydrate sur la conductivité protonique et les mécanismes de formation des hydrates d'acides est crucial pour l'utilisation des hydrates dans des applications énergétiques. Le présent projet de thèse est une contribution à cet objectif.

Publications

1. Métais, C.; Petuya, C.; **Espert, S**.; Ollivier, J.; Martin-Gondre, L.; Desmedt, A. Nitrogen Hydrate Cage Occupancy and Bulk Modulus Inferred from Density Functional Theory-Derived Cell Parameters. J. Phys. Chem. C 2021, 125 (11), 6433-6441. https://doi.org/10.1021/acs.jpcc.1c00244.

2. **Espert, S**.; Desplanches, S.; Metais, C. ; Desmedt, A. ; Sanchez-Portal, D. ; Combining NMR and DFT calculations study on the hexafluorophosphoric acid hydrate.study. *In preparation*.

Table of contents

General Introduction

Energy and environmental concerns are significant issues. Due to the diminution of fossil fuel resources, the impact of nuclear energy production and the awareness of environmental and climate problems, it is currently essential to consider alternative solutions. Designing new devices dedicated to energy storage and production is at the centre of nowadays concerns. Renewable energies (solar, wind or hydraulic) is the subject of numerous research and development activities. These intermittent production methods require energy storage solutions, which hydraulic dams or batteries can provide. Fuel cells are also a relevant alternative for electricity production. Fuel cells using hydrogen as an energy carrier have good energy yields and produce no greenhouse gases. They are a clean and efficient solution today and could become a possible substitute for hydrocarbons.

Clathrate hydrates represent systems that offer new opportunities and are relevant to energy and environmental issues. These crystalline solids are composed of 85% water molecules forming a host network with nanoscale cavities capable of trapping guest molecules. In the case of gas hydrates, the guest molecules are gaseous species (CO_2, CH_4, H_2 etc) and offers new opportunities in the broad area of energy and environment. Clathrate hydrates have represented new solutions for numerous applications linked to their molecular encapsulation capacity and their specific thermodynamic properties: storage and transport of gases such as methane or hydrogen, capture and separation of CO2 and other acid gases, refrigeration and cold storage, water purification/desalination, etc. One of the first reasons for the interest in clathrate hydrates was the natural abundance of these compounds in various systems of geological interest like methane hydrates present in permafrost and the ocean floor. The large quantities of natural gas hydrates represent a potential unexploited energy reserve. However, their decomposition is the source of geological hazards (instability of the seabed) and the potential release of encapsulated methane into the atmosphere, impacting climate change (greenhouse effect). Using these reserves as fossil energy brings critical environmental issues as it would contribute to the global carbon balance. Future developments using hydrates systems rely on a fundamental understanding of their specific nano structuration, their

thermodynamic stability and their original physicochemical properties linked to the guests' nature (e.g. molecular selectivity, thermal conductivity, ionic conductivity).

One particular class of hydrate system are the ionic clathrate hydrates. The inclusion of ionic guest species (strong bases, strong acids, …) in the hydrate nanopores leads to the host water substructure containing not only water but also ionic defects (H^+, OH^-, etc.). Ionic hydrates are particularly interesting in the area of energy for their specific physicochemical properties and bring new opportunities due to the structural, dynamic, kinetic and thermodynamic modifications generated by including ionic species.

In the case of strong acid clathrate hydrates, the confinement of acids within the aqueous cages generates an excess of protons capable of delocalised along their aqueous network. A striking property in these acid hydrates is their excellent protonic conductivity, thanks to the super-mobility of protons in the aqueous substructure. The excellent proton conductivity exhibited by these systems is of the same order of magnitude, or even higher, than some currently used fuel-cell membranes. Strong acid hydrates systems represent an opportunity as a new solid electrolyte for fuel cells for which fundamental questions are opened.

To get insight into the conductivity mechanism, experimental and theoretical approaches are combined in the cases of $HClO_4$ and HPF_6 hydrates – both systems ~~being~~ among the best conductors. Two issues have been addressed: the localisation of the ionic defects in the clathrate structures and their role in the protonic conductivity as a function of their concentration.

Hexafluorophosphoric acid hydrate exhibits an ionic superconductivity of up to 10^{-1} $S.cm^{-1}$ for a melting temperature of up to 30°C. Using such a hydrate as a PAC electrolyte was tested in previous work, for which an understanding of its physicochemical properties was investigated. Indeed, these materials were found to possess complex phase transition sequences linked to their hydration number (i.e. the molar ratio between water and acid molecules). The generation of fluorinated impurities in these systems was determined to play an important role in the conductivity. The variability in structure and chemical composition has a significant impact on the dynamic (long-range proton diffusion) and thermodynamic (stability range)

properties of these hydrates. Localising the ionic defects in the hydrate system is one of the objectives of this work.

To better understand the role played by the acid concentration on the protonic conductivity, it is possible to prepare mixed hydrates (i.e., encapsulating two guest species) by co-including $HClO_4$ acid and tetrahydrofuran (THF) molecules (THF hydrate is a prototypical clathrate hydrate, widely investigated). By varying the THF to $HClO_4$ ratio, such mixed hydrates offer the opportunity to control the concentration of the acidic defects in the hydrate structure. Evaluating the influence of the acid concentration on the protonic conductivity and its effect on the hydrate structure and stability is the second objective of this project. The important role played by this concentration is investigated by combining X-ray diffraction, Raman imaging and impedance measurements.

Understanding the links between chemical composition, structure, thermodynamic stability and conductivity in these hydrates is a central issue in this work. The determination of the fundamental process and parameters influencing the protonic conductivity mechanisms in the hydrate will help develop their use in energetic issues.

This manuscript is composed of five chapters, in addition to an introduction and general conclusion. The state of the art is presented in chapter I. This chapter ends with the strategy chosen to answer the fundamental questions on strong acid hydrate properties behind this thesis project. A presentation of the preparation protocol of the hydrate samples of THF and $HClO_4$ and of the different experimental methods used during the PhD is made in chapter II. In this chapter II, the quantum simulation method is introduced with the importance of the parameter determination process to study hydrate structure.

The use of quantum calculations to investigate the localization of the ionic defect in the HPF_6 hydrate is presented in chapter III.

Chapter IV explores the influence of the acid concentration and temperature on the structural properties of the THF/$HClO_4$ hydrates. The role played by these parameters on the crystal structures formed by the hydrate and their formation conditions are studied using X-ray

diffraction (XRD).

Finally, in chapter V, the impedance measurements performed on the mixed hydrates are presented. In addition, the use of Raman microspectroscopy offered the possibility to perform a spatial analysis at the micrometre scale and thus analyse the possible existence of heterogeneities within the sample. Chapter V ends with the proposition of models for the interpretation of the conductivity results in relation to the structural information determined by XRD and Raman spectroscopy. An open discussion on the accuracy and limitation of this model concludes this chapter.

Chapter I. STATE OF THE ART

Table of Contents

A. New materials – Hydrates

1. General introduction and applications

Clathrate hydrates are inorganic crystals forming nanoporous structures in specific thermodynamic conditions [SLO 08]. The crystal structure consists of collection of water molecules, called “host” molecules, forming a hydrogen-bond network and several types of cages. Inside these water cages, different molecular species can be trapped, for example, gas molecules like methane (CH_4) and carbon dioxide (CO_2), which are called “guest” molecules (see Figure I. 1).

Hydrate compounds can occur naturally in both biological and geological systems. Due to their natural occurrence in large quantities and various locations (planets, ocean floors, etc.), many studies are being conducted on this subject. Many types of clathrates exist, and since the discovery of H. Davy [DAV 11], more than 130 compounds have been found as guests in water clathrates [SLO 08]. The diversity of their composition, which gives them specific properties associated with their particular structure (water cages encapsulating molecules), has led to a growing interest in the study of these materials in both the scientific and industrial communities. For example, the large quantities of gas hydrate clathrates found under permafrost and the ocean floor are considered a possible untapped energy reserve [KOH 07].

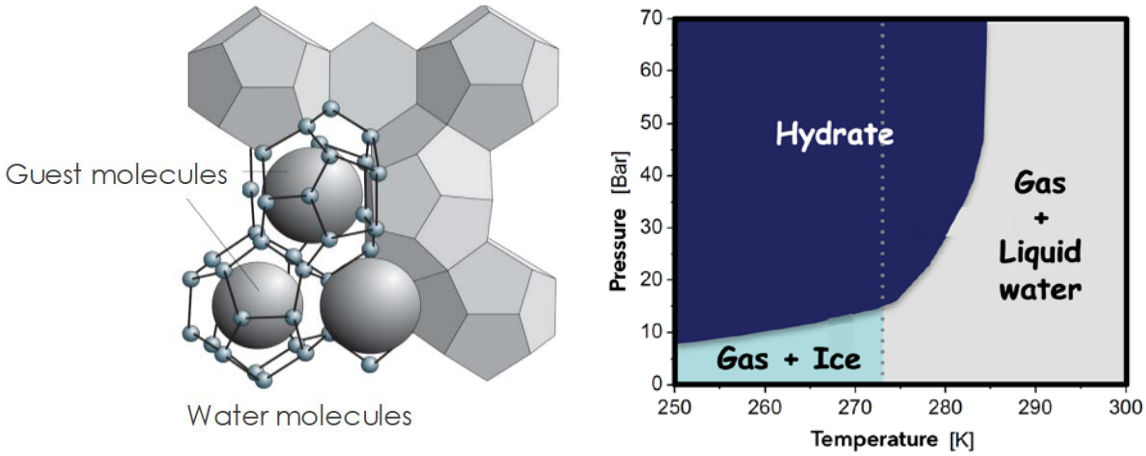

Figure I. 1. Example of the hydrate crystalline structure and the corresponding phase diagram.

i. Natural gas hydrate

Gas hydrates occur naturally on Earth in large quantities. They are located in the Earth's permafrost and the sediments of continental margins [KVE 01]. Figure I. 2 shows the global distribution of hydrate deposits on Earth. Although almost all of the Earth's permafrost contains hydrates, 97% of the natural hydrate reservoirs are included in marine sediments [YAN 19]. Among these natural gas hydrates, hydrates of light hydrocarbons (ethane, propane) or containing inorganic molecules like H_2S, CO_2 and N_2 have been observed. However, these hydrates represent only 10% of the natural samples collected [BOS 11], and methane hydrate is the most common [DIC 95].

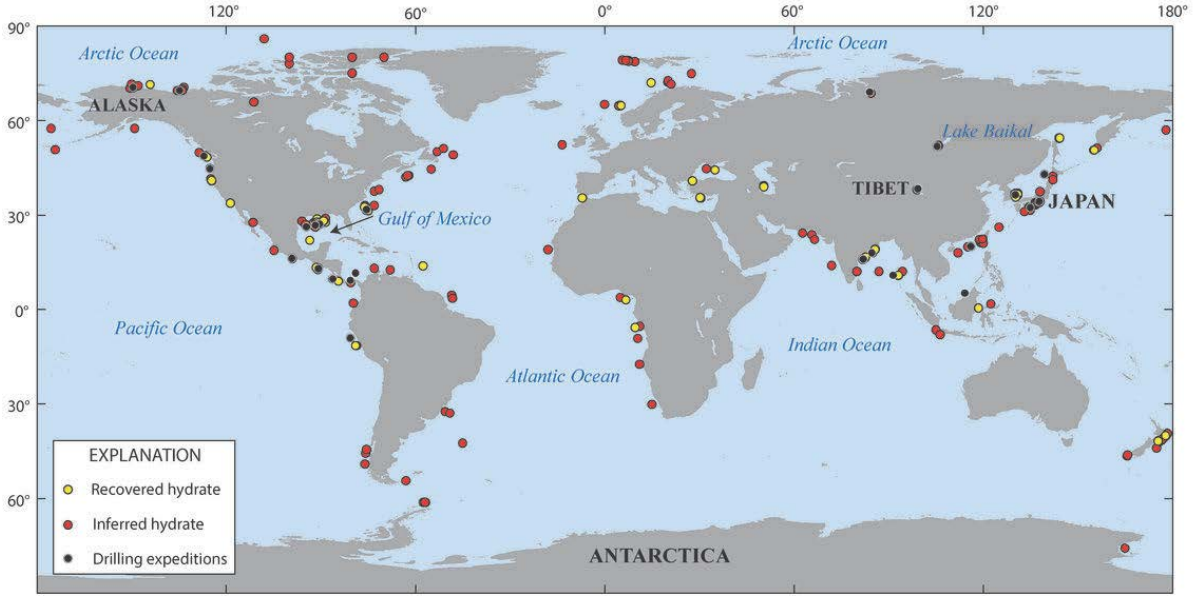

Figure I. 2. Map of the distribution of natural gas hydrates, showing deposits where hydrates have been recovered (yellow), where the presence of gas hydrates is assumed based on seismic data (red), and where drilling expeditions have been carried out in permafrost or deep marine environments, leading to the recovery of gas hydrates (black) [https://www.usgs.gov/media/images/map-gas-hydrates].

A unit of volume of hydrate can contain up to 160 to 180 units of volume of gas under standard temperature and pressure conditions [SLO 98]. Therefore, natural gas hydrates constitute an enormous reserve of potential energy, which has attracted the interest of many industries and research groups worldwide.

ii. The interest of hydrates: Applications

The ability of clathrate hydrates to trap certain gases opens up new possibilities for carbon dioxide sequestration and capture. Greenhouse gases are responsible for global warming, and CO_2 is one of the most critical contributors (it alone accounts for 60% of the global warming power). This capture process would involve trapping carbon dioxide into a stable hydrate under ocean floor conditions. This would offer the possibility of extracting the methane hydrate as an energy source while substituting it with carbon dioxide. This way, CO_2 would be sent to the ocean floor to replace the methane in the clathrates [CHA 05a].

These systems are also used for storing and transporting natural gas under mild conditions, i.e., at near-ambient pressures and temperatures, offering new industrial prospects. A clathrate volume can encapsulate about 160 times its volume of methane gas, and it remains stable at atmospheric pressure and around 250 K, unlike liquefied natural gas, which requires to be maintained at 110 K [SLO 03]. These storage properties are known for methane and, more recently, hydrogen [DES 10, KOH 07, DYA 99]. Due to climate issues, environmental problems and the reduction of fossil fuel resources, hydrogen is now playing an important role. It is envisaged as an energy carrier that can provide an alternative to hydrocarbons and compensate for the intermittence of certain renewable energy sources such as wind power or photovoltaics. However, it remains challenging to store and transport hydrogen due to its low energy density per unit volume, leading to research into developing safer, lighter and more compact storage tanks. Hydrogen storage in the form of hydrates is a possible solution.

These systems, which are still little exploited, are also of interest to industry because the formation of gas hydrates can stop the flow of hydrocarbons in pipelines, which constitutes considerable economic losses. In fact, an increase in pressure due to the formation of hydrate plugs inside pipelines can cause their destruction by an explosion. The hydrate plugs also pose a severe threat of gas pockets being released during drilling (through destabilisation of the gas hydrate layers), which could lead to explosions [CHA 05a]. To solve this problem and prevent clathrate from forming, it is necessary to control the pressure and temperature to avoid clathrate stability conditions or to use inhibitors [KOH 11].

Desalination of seawater is another example of a possible application of clathrate hydrates. The limited supply of natural fresh water for human consumption, irrigation and industrial processes is becoming a crucial problem. Seawater's desalination process consists of the formation and dissociation of hydrates. In 1960, Koppers Co. was the first to develop a desalination process by freezing salt water, using propane as a promoter [KOP 64]. After a phase change from liquid to solid, the hydrate crystals are only formed by pure water and guest molecules, and the pure water is recovered by heating the crystals. Other processes for the desalination of seawater using hydrate have emerged since then [BAB 18]. Understanding the mechanism and improving the efficiency of the different techniques is a constant challenge [KHA 19, ZHE 20].

A safe and profitable application of hydrate systems requires a deep knowledge of these materials' formation, stability, and intrinsic properties. Clathrate hydrates also present specific fundamental properties, and their understanding could offer the opportunity to deepen our knowledge of many physicochemical properties that are still under investigation.

2. The particular structure of hydrates

Hydrate structure consists of a solid network of hydrogen-bonded water molecules. The host structure of hydrate clathrates is composed of water molecules, each of them tetrahedrally connected to four other water molecules through their oxygen atoms giving and accepting two hydrogen bonds each. The crystalline hydrate structure varies depending on the nature of the trapped molecules

For non-metallic compounds, including clathrate hydrates, hydrogen interacts strongly with the electron density of the valence electron of only one or two of the nearest neighbours. The bonds formed between oxygen and hydrogen atoms take place at a distance of the order of 1 Å. In the case where several oxygens are separated by an average distance of between 2.5 Å and 2.8 Å, the hydrogen can be involved in two bonds: a short and strong bond with a proton donor and a long bond with a proton acceptor. This is an asymmetric hydrogen bond (O-H---O) with a directional character. When the oxygens are separated by short distances of about

2.4 Å, strong symmetric hydrogen bonds can also be formed. The hydrogen is then involved in two equivalent bonds [KRE 96].

There are two main crystalline structures: the SI structure and the SII structure. These structures are built with different arrangements of polygons formed by water molecules and hydrogen bonds (see Figure I. 3) [SLO 08]. Small cages (SC) are formed with twelve pentagons. Large cages (LC) are formed with 12 pentagons (noted 5^{12}) and 2 or 4 hexagons (noted 6^2 or 6^4), respectively, for SI and SII structures. The SI structure has a cubic lattice parameter $a \approx 12$ Å, space group *Pm*3*n,* containing 46 water molecules per unit cell. The structure called SII, with cubic lattice parameter $a \approx 17$ Å and space group *Fd*3*m*, contains 136 water molecules per unit cell, contains 16 SC and 8 LC.

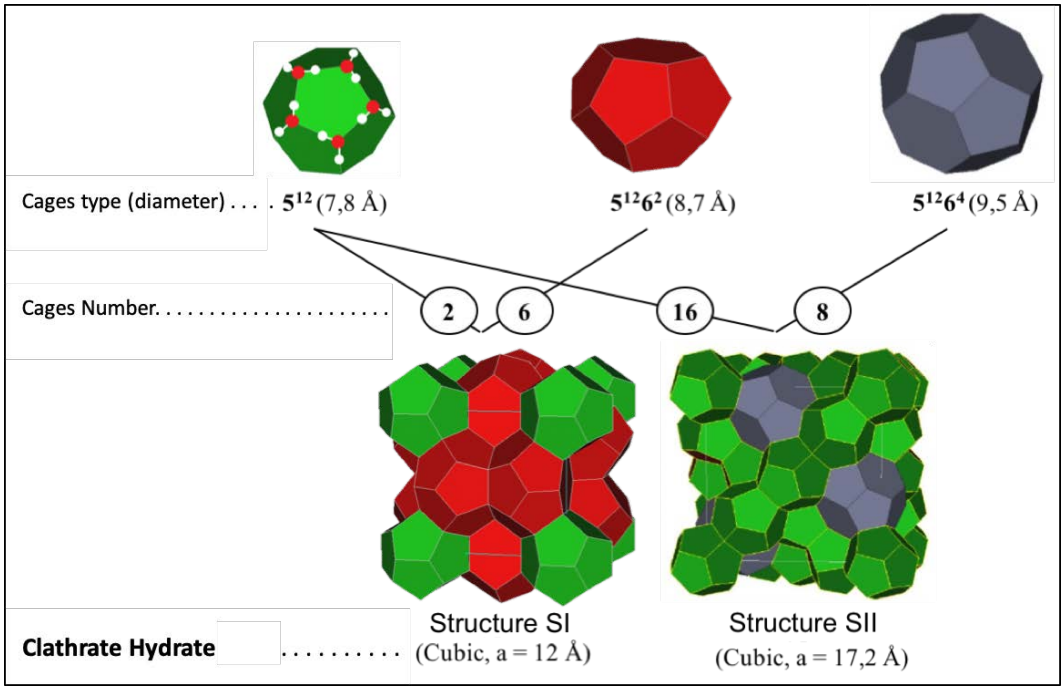

Figure I. 3. Most common hydrate structures: SI and SII structures where the vertices of the cages are occupied by oxygen atoms and the edges represent the hydrogen bonds [modified from DES 12].

The hydrate cages' shape, size and overall structure depend on the guest molecules, as well as the hydrate stability temperature and equilibrium pressure [SLO 08]. Not all hydrate structures can be formed depending on the nature and size of the guest molecules. For example, molecules like Tetrahydrofuran (THF), which is relatively large, can only occupy the

large cages, noted $5^{12}6^4$ in Figure I. 3, forming the SII hydrate structure. Molecules with smaller Van der Waals diameters tend to create the SI structure.

Despite the similarity of the hydrate structure with the ice structure, they have different properties. For example, clathrate hydrates have lower thermal conductivity than ice and, in the case of acid or base guest molecules, much higher proton conductivity.

3. Hydration number

Hydrate structures can be stable without filling all their cages with guest molecules. They are considered non-stoichiometric compounds [SLO 03]. Their stoichiometry is defined by the ratio of water molecules over guest molecules, called the hydration number *n*. This parameter corresponds to the guest occupation in the hydrate cages.

As examples from the literature show, this parameter can be determined experimentally by X-ray diffraction [UCH 02], nuclear magnetic resonance (NMR) [RIP 88] or Raman spectroscopy [SUM 97] [UCH 99]. When all their cages are filled, the SI and SII hydrate structures have a hydration number of 5.75 and 5.67, respectively. These two types of cubic structures have an ideal guest molecule concentration of almost 15%, corresponding to a composition of about 85% water.

Since large molecules cannot fill the cavities, it is common to find hydrate clathrates in which only the large cavities are filled. The values of the hydration number are then higher than the ideal values.

In addition, other phenomena are also likely to deviate the hydration number from its ideal value. For example, it sometimes happens that atoms substitute some of the water molecules in the crystal lattice, which is the case of certain clathrates known as semi-hydrates or salt hydrates [FOW 40]. Unlike simple clathrates, semi-clathrates accommodate the associated anion (fluoride, chloride, etc.) within the aqueous structure in a hydrophilic inclusion pattern.

B. Ionic hydrates

Hydrate crystalline structures can also be formed with ionic species, called ionic hydrates. Ionic hydrate clathrates are hydrate clathrates with anionic or cationic guest species in a cationic or anionic host network, respectively.

1. Generalities

For ionic hydrates, where the guest molecules are charged molecules (anionic or cationic), the corresponding counter ion must be incorporated to the water network of the hydrate structure, making it, respectively, cationic or anionic in response to the guest. Frequently this implies that a proton or an hydroxide ion will incorporate to the host structure. As a consequence, some of the water molecules in the aqueous lattice are substituted by hydronium H_3O^+ or hydroxide HO^- ions. This might result in the introduction of so-called Bjerrum defects as illustrated in Figure I. 4 in the case of tetrahedral lattice. A Bjerrum L defect corresponds to the absence of a hydrogen bond due to missing hydrogen, while a D defect qualifies two hydrogen atoms facing each other [BJE 57].

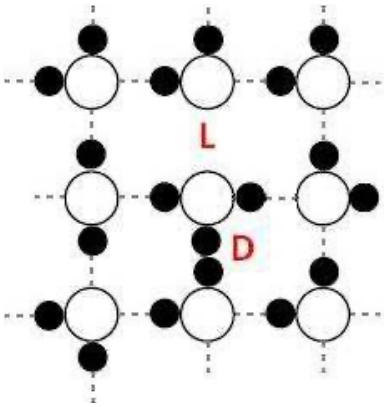

Figure I. 4. Schematic representation of a network of water molecules linked tetrahedrally by hydrogen bonds (dotted line) and showing Bjerrum L and D defects [BJE 57]. The empty and full circles represent the oxygen and hydrogen atoms, respectively.

Ionic guest molecules can form hydrogen bonds with the water molecules from the host hydrate's network and even be sometimes included in it. These structures can be called semi-hydrates or salt hydrates and were first identified by Fowler in 1940 [FOW 40]. These

compounds are formed from salts, mainly quaternary ammonium salts with butyl or isoamyl groups, consisting of an organic cation with hydrocarbon chains capable of inserting into cavities in the aqueous network (hydrophobic inclusion). Unlike simple clathrates, semi-clathrates also accommodate the associated anion (fluoride, chloride, bromide, hydroxide, etc.) within the aqueous structure in a hydrophilic inclusion pattern. Taking the example of the elementary crystal lattice of tetrabutylammonium bromide hydrate (TBAB), corresponding to the formula TBAB.38H_2O, the TBA^+ cation is thus located at the intersection of four large cavities (two cages 5^{12} 6^2 and two cages 5^{12} 6^3) where the four butyl groups are inserted, while the Br^- anion substitutes for a water molecule in the crystal lattice.

i. Cationic guests

In the case where the guest molecules are strong base molecules, the formed clathrate hydrate consists of an anionic host aqueous structure and cationic guest molecules. A proton deficit is therefore introduced into the aqueous network and resulting in the loss of a hydrogen bond and the presence of oxygens connected to not four but only three other oxygens. The study of the first reported examples of strong base hydrate clathrates [MOO 90], those of tetramethylammonium hydroxide TMAOH.10H_2O, β-TMAOH.7.5H_2O and β-TMAOH.5H_2O (β designating the high-temperature phase of these clathrates in the case of structural transitions), revealed such a deficit of proton in their aqueous network.

However, the oxygen atoms, water molecules and OH^- ions all appeared to be connected four times. This was explained by the existence of significant dynamic proton disorder within their anionic network, resulting in the observation of four proton sites, each with an occupancy probability of 1⁄2, around the oxygen atoms.

Furthermore, examples of the coexistence of two clathrate phases adopting different crystal structures have also been noted. Thus, when their water concentration is increased, tetramethylammonium hydroxide (TMAOH) and dihydrogen clathrate hydrates present in parallel an SI structure phase and an SII structure phase [CHO 07].

ii. Anionic guests

When the guest molecules are strong acids, the clathrate hydrate forms a cationic host aqueous structure in which anionic guest molecules are encapsulated [BOD 55, DAV 72]. The encapsulated acid molecules are deprotonated, and the excess protons participate in the structure of the cage [MOO 87, WIE 86].

Similar to basic hydrate clathrates, the acidic proton of the guest molecule can delocalize spontaneously onto the cationic aqueous matrix [WU 05]. The extra protons form hydronium ion H_3O^+ in the hydrate sub-structure alongside water molecules. The substitution of certain water molecules by hydronium ions H_3O^+ introduces ionic defects in the aqueous network, having an impact on the physicochemical properties of the system.

The precise structural determination of acid hydrates is a challenge due to the proton disorder within their host lattice. The first studied examples of strong acid hydrates were HPF_6-$7.67H_2O$, HBF_4-$5.75H_2O$ and $HClO_4$- $5.5H_2O$ hydrates, and only the structure of HPF_6 hydrate was determined by differential thermal analysis and X-ray diffraction [MOO 87].

The structure of the acid hydrate clathrate formed depends strongly on the size and valence of the encapsulated anion as well as the temperature and hydration number. The water content is likely to play a significant role in inducing structural transformations since hydrate can form structures without all their cavities necessarily being occupied by guest molecules.

Structure of the HPF_6 hydrate

The hexafluorophosphoric acid clathrate $HPF_6.nH_2O$ (where n is the hydration number) is able to form in two types of crystal structures (SI and SVII) with different physical properties (see Figure I. 5) [CHA 08]. This hydrate illustrates the influence of the hydration number parameter onto the hydrate structure.

The study of HPF_6-$7.67H_2O$ by differential thermal analysis and X-ray diffraction identified it as having a SI hydrate structure at 111 K [MOO 87]. This structure, shown in Figure I. 3, has a

cubic unit cell of 11.774 Å described by the space group Pm3n. The lattice consists of 46 water molecules forming two pentagonal dodecahedra (cages 5^{12}) with a diameter of 7.8 Å and six polyhedral (cages $5^{12}6^2$) with a diameter of 8.7 Å. Due to the diameter of the PF_6^- ion, only the largest cages $5^{12}6^2$ are occupied while small cavities remain vacant. Its structure appeared disordered with hydrogen atoms distributed between two positions of 1⁄2 occupancy probability.

The SVII structure has been studied by X-ray diffraction [BOD 55, WIE 86] for the hexafluorophosphoric acid clathrate $HPF_6.6H_2O$. This structure has a cubic elemental lattice of 7.678 Å, described by the space group $Im3m$. The mesh is composed of 12 oxygen atoms which form truncated-octahedral cages of type $4^6\ 6^8$. Considering that the distance is taken between the centers of mass of the oxygens, a diameter of 7.678 Å is measured between two opposite square faces. For this structure, all cages are occupied by PF_6^- ions.

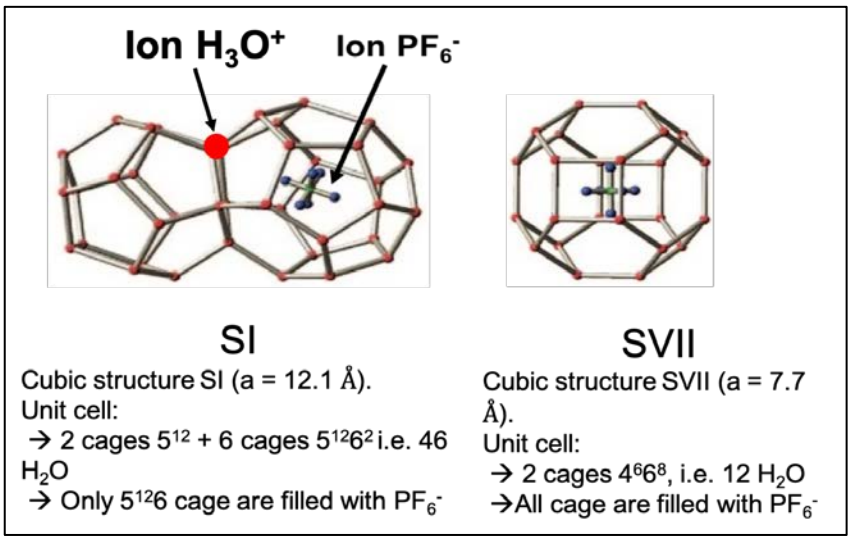

Figure I. 5. SI and SVII hydrate structures adopted by hexafluorophosphoric acid clathrate, adapted from [CHA 08].

By differential scanning calorimetry (DSC) measurements [CHA 08], in addition to X-ray diffraction (XRD) measurements [BOD 55, WIE 86, MOO 87, CHA 08], it has been shown that the temperature influences the formed structure of the hexafluorophosphoric acid hydrate. It was also observed that the melting temperature of the hydrate varies with the hydration number. A maximum is observed for the $HPF_6.6H_2O$ clathrate ($T_{melting}$ = 29.5°C).

Clathrate hydrates HPF_6-nH_2O with a hydration number *n* lower than 6 adopt, whatever the temperature, a SVII structure. In the case where the hydration number is equal to or higher than 6, the hydrate presents a structural transition in the vicinity of 230 K. It adopts a SI structure at low temperatures, then evolves towards a SVII structure at high temperatures.

In Cha *et al.* [CHA 08], differential scanning calorimetry curves were taken for the HPF_6·nH2O hydrate as a function of the hydration number. The SI to SVII structure transition temperature was determined to increase with the hydration number. It should be noted that for hydration number n=6, the result obtained in this study is contradictory to previous XRD results [BOD 55, WIE 86], the latter indicating that this hydrate has a unique SVII-type structure. Another contradiction appears for the low-temperature phase of the hydrate $HPF_6.7{,}67H_2O$: Cha et al [CHA 08] performed an X-ray diffraction analysis revealing a mixture of SI and SVII structures at 93 K, while Mootz et al [MOO 87] only observed the SI structure at 111 K.

It is therefore interesting to note that small adjustments of the amount of water can modify the structure of the clathrate. Nevertheless, it should be kept in mind that the thermodynamics of clathrate formation remains complex and that the information obtained here is dependent on the speed of the temperature ramp chosen to perform the DSC measurements. In fact, studies by pulsed field gradient proton nuclear magnetic resonance spectroscopy (PFG-1H-NMR) and quasi-elastic neutron scattering (QENS) experiments have highlighted a thermal dependence of the SI-SVII phase structural transition by the observation of a hysteresis in the proton scattering process [BED 14].

Compared to other acid hydrate clathrates such as HBF_4-$5.75H_2O$ and $HClO_4$-$5.5H_2O$, which can be formed only in the SI structure and have melting temperatures of -66 °C and -45 °C respectively [MOO 87], the SVII structure adopted by the HPF_6-$6H_2O$ hydrate allows a much higher melting temperature (29.5 °C), close to ambient. This thermodynamic characteristic may be of great importance for the possible application of this solid proton conductor as an electrolyte.

2. Properties of ionic hydrates

In contrast to non-ionic hydrate clathrates stabilized by Van der Waals interactions between guest molecules and host lattice alone, an important contribution in ionic hydrate clathrates comes from the ionic interaction between their guest molecules, either cationic or anionic, and the aqueous lattice balanced by counter ions [JEF 84]. Most of the ionic hydrate clathrates are known to form unique structures, largely dependent on the size and valence of the cations or anions as well as the hydration number. In particular, as discussed above for the HPF_6 hydrate, their water content has been shown to play a significant role in inducing structural transformations and consequently affecting their phase behaviour and physical properties [JEF 84].

Some of them present the particularity of having their guest molecules taking part in the aqueous network. For example, in the crystal structures of ionic hydrate clathrates of tetra-butyl-ammonium halide (TBA) or tetra-isoamyl-ammonium (TIA), water molecules and halogen anions form a network of water molecules and anions linked by hydrogen bonds [ROD 10].

There are two types of protonated host structures depending on the nature of the acid. One host network can contain hydrogen fluoride (replacement of water molecules by HF); this option is known to be suitable for clathrate hydrates of structure VII such as HPF_6, $HAsF_6$ or $HSbF_6$ hexahydrates [WIE 86, DAV 72, DAV 81]. The other host structure is free of hydrogen fluoride (HF) but contains defects in the hydrogen bonding network, which are responsible for the protonation of the host network, such as the hydrates of HBF_4 or $HClO_4$. In this case, the vacant sites are considered to be occupied by the F or O atoms of the BF^- or ClO_4^- anions which lead to an eccentric and partial occupation of the anions, increasing the degree of disorder in the crystals [MOO 87].

The presence of these ionic defects in the aqueous substructure results in a modification of their intrinsic physico-chemical properties and gives them specific properties. Ionic hydrate clathrates can exhibit a higher average melting temperature (above room temperature) than non-ionic hydrate clathrates, which can be attributed to the strength of ionic interactions

between guest molecules and the aqueous network.

In addition, strong acid clathrates are known to have high proton conductivity. Indeed, the confinement of strong acids in cages such as HPF_6, HBF_4 or $HClO_4$ generates an excess of protons that delocalise along the aqueous network. These dynamically delocalised ionic defects give rise to proton diffusion. They are then at the origin of an ionic superconductivity which can reach 10^{-1} $S.cm^{-1}$ for hexafluorophosphoric acid clathrates (HPF_6) at room temperature [CHA 08]. The proton conductivity is comparable or even higher than that of commercial Nafion membranes (0.09 $S.cm^{-1}$ [SON 96]), currently used as electrolytes in fuel cells.

Due to their specific properties, these types of hydrates are, therefore, very interesting solid proton conductors with promising applications [SHI 10]. Despite the fact that the ionic behaviour of the loaded host lattice of these clathrate hydrates has been the subject of particular attention in recent years, little work has been carried out to identify and optimize the conditions (hydration number and temperature) to growth the structures with the largest proton conductivity.

C. Protonic Conductivity

The ionic hydrate clathrates characteristics can make of them functional materials with promising applications. The conductivity resulting from the ionic behaviour of the charged host matrix is the subject of particular attention in connection with the development of proton conductors.

Both polyatomic complexes and single monoatomic ions incorporated in the lattice cages could function as proton conductors [CHO 07, BOR 98, PRO 01]. However, although the large conductivity values associated with the fairly free movement of protons in the "frozen" water structure are attributed to the delocalization of their proton excesses or defects, the mechanisms governing this delocalization need to be investigated.

1. Conductivity Principle

The conduction of protons is a matter transport phenomenon corresponding to the diffusion process of H^+. In general, this migration of species takes place in systems out of equilibrium, e.g., where the particles are heterogeneously distributed, and happens from regions of high concentration to regions of lower concentration. Diffusion tends to make the medium homogeneous and its composition uniform.

The law that relates the flow of particles (the effect) and the inhomogeneity of the concentration of the particles (the cause) in the linear approximation was established in the 19th century by A. Fick. The kinetics of the phenomenon is quantified by the diffusion coefficient. The flow of matter, represented by the particle flux density vector $\vec{j}_D$ generated by this transport phenomenon, is proportional to the particle concentration gradient *n* via the diffusion coefficient *D*, according to Fick's law.

$$\vec{j}_D = -D\overrightarrow{grad}(n) \qquad (I.1)$$

The negative sign of this expression reflects the fact that the particle flow is from the regions with higher concentrations to regions with lower concentrations. The diffusion coefficient *D* is always positive and corresponds to the square of the average distance travelled by the particles per unit of time.

This mesoscopic interpretation has been based on different diffusion mechanisms of microscopic origin, particularly in the case of protons. The different models of diffusive mechanisms proposed in the case of aqueous systems will be explained first. We will later discuss them in relation to the proton conduction properties of ionic hydrates.

Several scientists have tried to model proton conduction by different models of diffusive mechanisms to describe the conduction of the H^+ ion in water. These mechanisms are generally related to the nature of the hydrogen bonds. It was possible to demonstrate the existence of two main modes of proton conduction, the Grotthuss-type mechanism and the

vehicular transport mechanism.

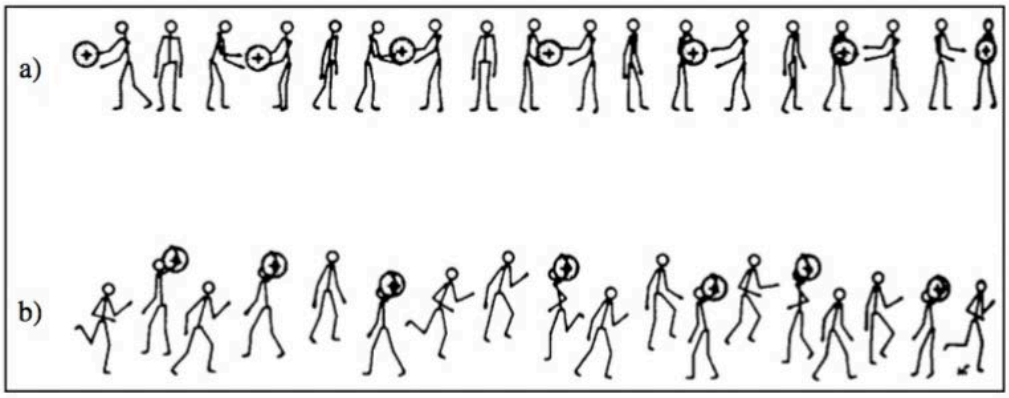

Figure I. 6.Illustration of the different proton transport mechanisms: a) cooperative transport or Grotthuss mechanism and b) vehicular transport mechanism [KRE 82].

When the interactions between the water molecules and their direct environment are weak, the protons move bound to a water molecule in the form of the hydronium ion H_3O^+, as shown in Figure I. 6.b) [KRE 82, KRE 96]. This is the vehicular mechanism. The water molecule is used as a "vehicle" by the proton to diffuse (e.g., H_3O^+). The water molecules not bound to a proton, the "empty vehicle", move in the opposite direction, as shown in Figure I. 6.b). This type of mechanism is at the origin of the phenomenon of electro-osmosis, in which water molecules are transported by the proton flow.

In the case of strongly bonded water molecules, protons H^+ jump directly from one water molecule to another, which become alternately donors and acceptors. This is a cooperative transport mechanism called the Grotthuss mechanism [GRO 06]. As illustrated in Figure I. 6.a), one water molecule receives a proton from its previous neighbour, becoming H_3O^+, then transfers one of its 3 protons to its next oxygen neighbour. This mechanism requires, during the transfer, a reorientation by rotation of the water molecules and the rearrangement (breaking and forming) of hydrogen bonds [KRE 82]. For this so-called structural diffusion model, the transport of protons does not require the diffusion of the carriers (water molecules). However, the mechanisms governing these proton exchanges are complex. In reality, the most stable form of the aqueous proton involves the passage through the

formation of intermediate structures which are larger complexes such as Eigen ($H_9O_4^+$) and Zundel ($H_5O_2^+$) cations [KRE 04, AGM 95]. The Grotthuss mechanism is a collective transport process.

Due to the solid structure of hydrates (oxygens are at "fixed" positions), the Grotthuss mechanism is the most likely to be at work.

i. Conductivity in hydrates.

The superconductivity of ionic acid hydrates has been identified as resulting from the delocalisation of hydrogen bond defects due to an excess of protons along their aqueous host network. This delocalisation occurs according to the Grotthuss-type diffusion mechanism [DIP 91, ASC 94, CAP 94, DES 04, BED 14], which includes, during proton diffusion, two phenomena simultaneously. This model involves both the rapid and successive transfer of protons from one oxygen in the hydrate lattice to another, complemented by the reorganisation of the molecules surrounding the proton (reorientation of neighbouring water molecules).

Pulsed field gradient NMR and quasi-elastic neutron scattering experiments probed these proton dynamics, both in the spatial and temporal domains. Thus, the combination of these two techniques revealed the existence of these two types of processes within ionic clathrate hydrates and allowed their characterisation. The slower dynamic process was associated with long-range translational proton transfer between oxygen sites and the faster process with reorientations of water molecules [BED 13, BED 14, DES 04, DES 13]. This long-range proton diffusion is generated by the transfer of protons between first neighbour oxygens, which then leads to the formation of uninterrupted trajectories favourable to proton migration.

2. Strong acid hydrates

In the case of strong acid guest molecules, the acidic proton delocalization within the cage sub-structure generates super-protonic conductivity due to the super-mobility of protons in

the host substructure [DES 18]. They can exhibit excellent proton conductivity of the same order of magnitude, or even higher, than that of some fuel-cell membranes currently in use. Thus, ionic hydrates constitute an opportunity as new electrolytes for fuel cells. The best conductivity to date is known for HPF_6 hydrates (strong acid) [CHA 08].

i. Protonic conductivity of strong acid hydrates

Several studies using NMR measurements of deuterium [HUA 88] and conductivity by impedance spectroscopy [HUA 88, ASC 94, CAP 91, CAP 94, BOR 92] have been reported on $HClO_4$-$5.5H_2O$, HPF_6-$7.67H_2O$ and HBF_4-$5.75H_2O$ as a function of the temperature. These results made it possible to obtain values of the activation energies of the proton conductivity and revealed that, even at very low temperatures (frozen state), the protons of the clathrate structure are very mobile. All these hydrates exhibit the SI structure but have different cage occupancy. The anions fill only the large cages of the structure for hexafluorophosphoric acid, whereas for tetrafluoroboric and for perchloric acids, both types of cages are filled. In spite of this, the conductivity measurements have a very similar behaviour. Therefore, it appears that the conductivity is more influenced by the structure adopted by the clathrate hydrate than by the nature of the guest anion or the way the cages are occupied. In the liquid state, hydrates behave like concentrated solutions of electrolytes and have a high conductivity that changes very little with temperature. The conductivity of the acid hydrates $HClO_4$-$5.5H_2O$, HBF_4-$5.7H_2O$, and HPF_6-$7.67H_2O$ does not change abruptly at the point of crystallisation (respectively at 228 K, 207 K, and above room temperature) but then shows a stronger temperature dependence when in the solid form.

Their conductivity is thus apprehended, according to different works [HUA 88, ASC 94, CAP 94, BOR 92], with several activation energies according to their state. An activation energy that is relatively low (about 0.05 eV) is found for the liquid state. For the solid state, the determined activation energies depend on the nature of the hydrates and are much higher (0.67 eV for HPF_6-$7,67H_2O$ and 0.75 eV for HBF_4-$5,7H_2O$). The transport of the proton itself, from the hydronium ion to the oxygen of a neighbouring water molecule, can also be explained according to a quantum model.

The two crystallographic structures, SI and SVII, provide a different environment for ionic movement, which could have an impact on proton mobility. It has been shown by Cha *et al.* that the difference in these two structures has an influence on the conductivity behaviour [CHA 08].

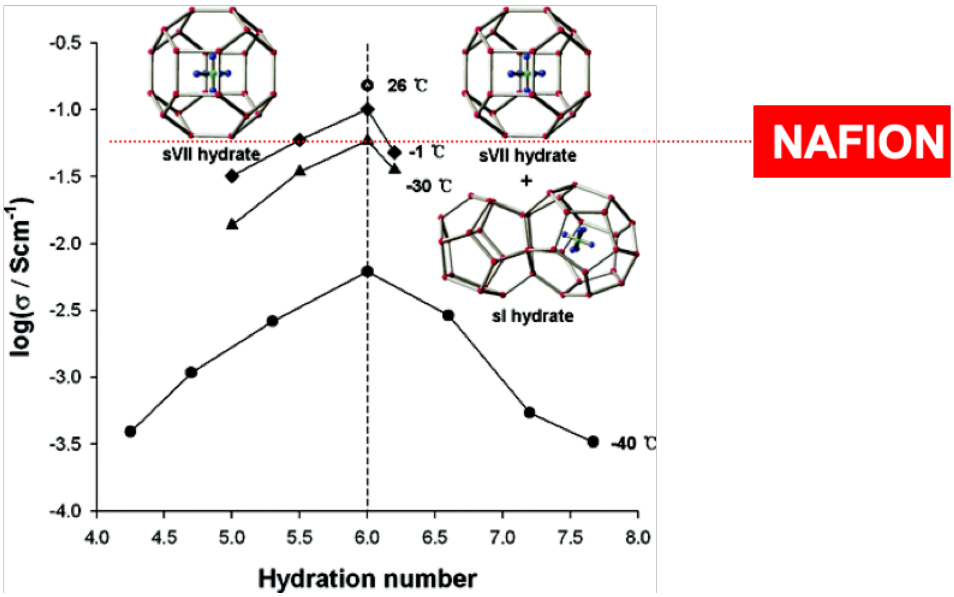

Figure I. 7. Ionic conductivity measurements of hexafluophosphoric acid hydrate with variation hydration number x to -78,5 °C (full circles), -30 °C (triangles), -1 °C (rhombuses) et 26 °C (empty circles). [CHA 08].

Figure I. 7 shows conductivity measurements from Cha *et al.* [CHA 08] for HPF_6-$n H_2O$ clathrate hydrate samples at different hydration numbers (n = 4.2; 4.7; 5.3; 6; 6.6; 7.2; 7.7). These data allow to understand the behaviour of ionic conductivity as a function of water content. Measurements carried out at -78.5 °C (solid circles) show that an increase in the hydration number favours the ionic conductivity, reaching a maximum value for HPF_6-$6H_2O$ of 6.18×10^{-3} $S.cm^{-1}$. On the contrary, for hydration numbers higher than 6, the ionic conductivity decreases considerably, reaching the lowest value at the largest explored hydration number n = 7.7. At the same temperature, the ionic conductivity of the clathrate hydrate HPF_6-$6H_2O$ is almost 20 times higher than those of the samples with n = 7.7 and n = 4.4. Two other isotherms at -30°C and -1°C confirmed the observation of a conductivity maximum for the hydration number n = 6.

Unlike the conductivity behaviour of polymeric and liquid electrolytes, which increases with

membrane hydration [BER 13], these systems show a maximum at an intermediate hydration number, n = 6, according to the results of Cha *et al.* It is interesting to note that this hydration number (n = 6) corresponds to the ideal molar ratio of water to acid for the formation of the SVII structure. In other words, it is the amount of water required for the stoichiometric composition of this structure. For this hydration number, the evolution of the conductivity as a function of temperature was also studied [CHA 08, ASC 94] and revealed that it increases with temperature, reaching a value of the order of 10^{-1} S.cm^{-1} at 26 °C.

It has been shown that the structural transformation of the acid hydrate HPF_6 from SI to SVII improves the ionic conductivity and leads to a higher conductivity than other strong acid hydrates that form in an SI structure [SHI 10]. These conductivity measurements suggest that the SVII crystal structure is more favourable for charge carrier transport. Cha *et al.* [CHA 08] have provided several arguments as to why the SVII structure would strongly favour ionic conduction. On the one hand, this could be due to the greater symmetry of cage $4^6 6^8$ in the SVII structure compared to cage $5^{12}6^2$ in the SI structure. This would allow, when stacked along their hexagonal or tetragonal faces, to create continuous diffusion pathway patterns in the crystalline hydrate matrix. On the other hand, Cha *et al.* pointed out that cage 4^6 has a larger diameter than cage 5^{12}, which could lead to a weaker interaction between the PF_6^- anion and the proton and contribute to higher ionic conduction through the water networks.

However, this hypothesis provided by Cha *et al.* [CHA 08] on the size of the cages is in disagreement with the diameters determined in previous scientific publications [BOD 55, WIE 86, MOO 87], which show a larger cage diameter for cages $5^{12}6^2$ than for cages 4^6 6^8. The origin of the high conductivity might not necessarily be only a question of the arrangement of the cages within SVII structure. It could also be due to the presence of an excess of water which coexists with the solid phase following the transformation from SI to SVII structure. Indeed, as explained previously, the ideal molar ratio between water and acid, necessary for the formation of SVII structure, corresponds to the hydration number n = 6. Whereas for the formation of SI structure, n = 7.67 is needed. Thus, for a hydration number higher than 6, when the temperature increases and the hydrate undergoes the structural transformation (SI to SVII), part of the water contained in SI is found in excess during the formation of SVII.

In conclusion, the water content of the hydrate plays a very important role since the addition or removal of a small amount of water can induce a structural transformation that affects its phase behaviour and physicochemical properties.

D. Proposed investigation of strong acid hydrates

The importance in the broad area of energy of ionic clathrate hydrates is gaining interest. The ionic hydrates open up several technological opportunities derived from their specific physicochemical properties. These materials have a complex sequence of structural phase transitions that are related to their hydration number (i.e., the molar ratio between water and acid molecules). This variability in structure and chemical composition has a significant impact on the dynamic (long-distance proton diffusion) and thermodynamic (stability domain) properties of these hydrates.

For this reason, we propose here an investigation of some strong acid hydrates. The final goal of our project is to determine whether different crystal structures are associated with specific chemical composition of the samples, as well as to clarify the impact of both the chemical composition and the structure on the proton dynamics in the hydrates.

1. Complementing experimental studies on HPF_6 hydrate

Desplanche *et al.* [DES 18] performed Raman spectroscopy and X-Ray Diffraction on HPF_6 hydrate. The complementarity of these techniques allowed us to better understand the influence of the hydration number on the formation of the different structures presented before (SI and SVII), and also to observe the chemical modifications of these hydrates associated with the SI-SVII structural transition [DES 18].

The study by Desplanche *et al.* [DES 18] revealed that for samples with a hydration number n > 6 and at high temperature ($T \gtrsim 230\ K$), the PF_6^- anions felt a new molecular environment, different from the anion encapsulated in the SVII structure. Raman spectroscopy with

micrometer resolution revealed the presence of PF_6^- anions in the surface of the samples. Furthermore, these measurements also revealed the presence of other species, such as H_3PO_4, H_2PO_3F, HPO_2F_2 and HF, derived from the hydrolysis of HPF_6 acid (reaction of HPF_6 with water). This surface layer did not seem to show any crystalline organisation. The formation and evolution of this micro-structure was analysed by studying its thermal stability and formation kinetics. During thermal cycles, it was observed that the appearance of this layer was correlated with the structural transition between SI to SVII at T ~230 K. This phenomenon, causing the micro-structuring of the sample, was observed only for hydration numbers above 6.

All the information gathered by Desplanche *et al.* [DES 18] during the characterisation of the HPF_6-$n$$H_2O$ systems by the different techniques allowed to propose a structural model as a function of the hydration number and temperature, shown in Figure I.8.

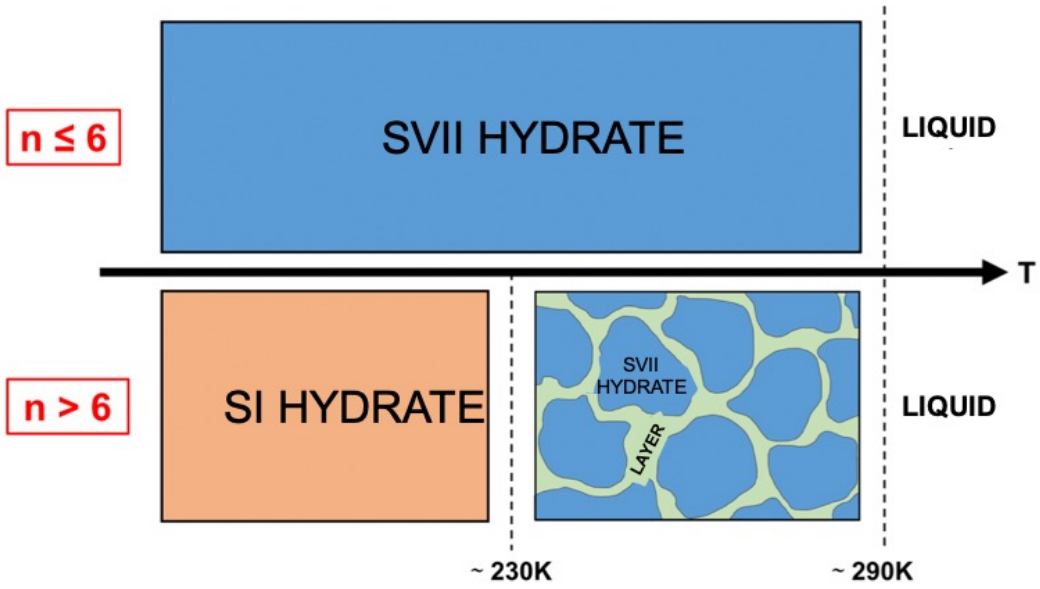

Figure I. 8. Study recollection of the HPF_6 hydrate structure depending on the hydration number and the temperature [DES 18].

By the NMR of fluorine and phosphorus, Desplanche *et al.* [DES 18] were able to partially determine the nature, concentration and location of the chemical species present in the

samples, such as the PF_6 - anions and the species associated with the impurities: H_3PO_4, H_2PO_3F, HPO_2F_2 and HF. For the sample with n > 6, it was observed that the presence of these impurity species is more important. Desplanche *et al.* [DES 18] identified that some of them have an environment close to an acid solution in the liquid state. These results confirmed the partial presence of impurities in the layer between grains of the hydrate structure (see Fig. I 8). As shown by Desplanche *et al.* [DES 18], the presence of this layer influences the protonic conductivity of the samples.

Since only some of the impurities were localized within the micro-structure layer [DES 18], the hypothesis that these species can be incorporated in the hydrate structure was formulated. Due to their nature and molecular size, the encapsulation of the impurities within the HPF_6 hydrate seemed possible.

In order to study the possible co-inclusion of HPF_6 molecules with impurities species (H_3PO_4, H_2PO_3F, HPO_2F_2) in hydrate structure, quantum calculations have been used in this work. Quantum simulations allow us to reproduce the hydrate crystalline structure and study the structure stability depending on the various guests.

Simulations have already been used to study hydrate systems [CHO 19, COS 15, HIR 15, DES 15, SUN 17, and ZHA 18]. Van der Waals interactions between the water molecules and the guest molecules ensure the stability of the structure [HAS 06]. The accuracy of using quantum calculation and, specifically, the Density Functional theory (DFT) for hydrate structure simulation will be discussed in Chapter II.

As a complement to the very complete experimental work on the study of the HPF_6 hydrate structure by Desplanche *et al.* [DES 18], DFT calculations with HPF_6 hydrate will be detailed in Chapter III. As will be described there, our calculations confirm the hypothesis formulated by Desplanche et al. that the above-mentioned impurities can be incorporated inside the HPF_6 hydrate structure.

2. Structural study of hydrate with co-included guest

To investigate the influence of the acid concentration on the conductivity, we explore tuning the acid concentration by co-including various species. When different guest molecules are encapsulated in the same hydrate structure, the hydrate is called a mixed hydrate.

First, a neutral molecule with an acidic one needs to be carefully selected so that there are no chemical reactions between them and that their molecular sizes allow both of them to be encapsulated (hydrate cages are smaller than 10 Å). Then by playing on the initial ratio of the species in solution, the composition inside the hydrate structure will be tuned. The molecules selected are tetrahydrofuran (THF) and perchloric acid ($HClO_4$). These molecules are known to form hydrate structures when taken separately. The THF hydrate is well known and has already been studied [CON 09, PRA 07, ALA 12]. The $HClO_4$ hydrate structure is also known [MOO 87], but the particular properties due to its ionic nature have been less investigated [BRI 49, RAT 84, DES 04, DES 13].

The mixing of a neutral species (THF) with an acidic species ($HClO_4$) to form a hydrate structure has already been studied by Desmedt *et al.* [DES 15]. The SII hydrate structure, mixing tetrahydrofuran (THF) and perchloric acid guest molecules, is synthesized and investigated by means of calorimetric, X-ray diffraction, and Raman scattering measurements together with a computational structure relaxation in the density functional theory approximation.

In the paper by Desmedt *et al.* [DES 15], the formation of the mixed clathrate hydrate with perchlorate anion included in the large cage of the cationic host-substructure of the THF SII hydrate requires the cooling of a solution at $(1-\alpha)THF - \alpha HClO_4 - 17H_2O$ with α less than 0.125. Above this limitation, a multiphasic regime is observed in the formation of the hydrate (mixture of SI and SII). The substitution of a THF molecule per perchlorate anion allows the modification of the melting of the SII hydrate by preserving the clathrate structure. Shrinkage of the SII unit cell is measured together with a softening of the host lattice mode. This study reveals the key role played by acidic defects existing in the host substructure on the physicochemical properties of clathrate hydrate [DES 15].

The study on the HPF_6 hydrate [DES 18] highlighted the positive influence of the presence of mixing in structuration as well as the hydrate structure influence on the protonic conductivity.

The co-inclusion of THF and $HClO_4$ in the same hydrate structure in principle should allow to isolate the influence of the acid concentration on the protonic conductivity [DES 15]. The mixing of hydrate structures (SI and SII), taking place as the acid concentration increases [DES 15], might open new possibilities to improve the conductivity of these materials.

In this Thesis work, the structure of the mixed hydrate THF-$HClO_4$ has been studied for various acid concentrations. The sample preparation and the experimental techniques used are presented in Chapter II. The investigation by X-ray diffraction of the crystalline structure of the various samples and their stability are described in Chapter IV.

Once the hydrate structures have been identified for the various concentration, the next step is to investigate their effect on the protonic conductivity. In the last chapter of this dissertation, models linking the conductivity to the acid fraction and the temperature are presented. These models highlight the importance of the arrangement of the various phase in the mixed hydrates. Raman imaging experiments provide some answers regarding such micro-structuration. Finally, the conductivity measurements performed on the mixed hydrate for various acid concentrations are interpreted on the bases of the structural data obtained by XRD in Chapter IV and the Raman imaging in Chapter V.

Chapter II. Methods

Table of content

In this chapter, we describe the scientific methods used during this work. We combined experimental and theoretical approaches to investigate the physico-chemical properties (conductivity, structure, vibrational properties, etc) of strong acid hydrates. We will start by presenting the experimental techniques used to study samples of the mixed hydrate of THF and $HClO_4$. The specificities of the various set-ups are highlighted. Then, we will focus on the theoretical simulation method: Density Functional Theory (DFT) and the specificities of the used code, the SIESTA package.

A. Experimental approach

1. Sample preparation

The studied system for the experimental approach is the mixed hydrate of THF and $HClO_4$. The water/guest ratio needs to be controlled carefully to form the hydrate structure. Solutions are prepared with 99,9% pure Tetrahydrofuran (THF) ($M_{THF} = 72{,}11\ g/mol$) and 70%wt perchloric acid ($HClO_4$) ($M_{HClO_4} = 100{,}46\ g/mol$) purchased from Sigma-Aldrich and with Milly Q water. Samples with various acid fractions were made by tuning the acid concentration while keeping the water to guest molecule ratio expected for the SII structure, i.e., according to the following chemical formula:

$$(1-\alpha)\mathrm{THF}\cdot\alpha\ \mathrm{HCl}O_4\cdot 17\mathrm{H_2O} \qquad (II.2)$$

The prepared solutions are then kept in a freezer at 250 K (-23°C). Mixed samples were prepared with α ranging from 0 to 0.833 (see Figure II. 1), corresponding to acid fractions from 0 %mol to 4.628 %mol $\left({}^{\alpha}/_{n_{tot}}\right)$. The mixed hydrate samples will be referred to their acid fraction in the rest of this work.

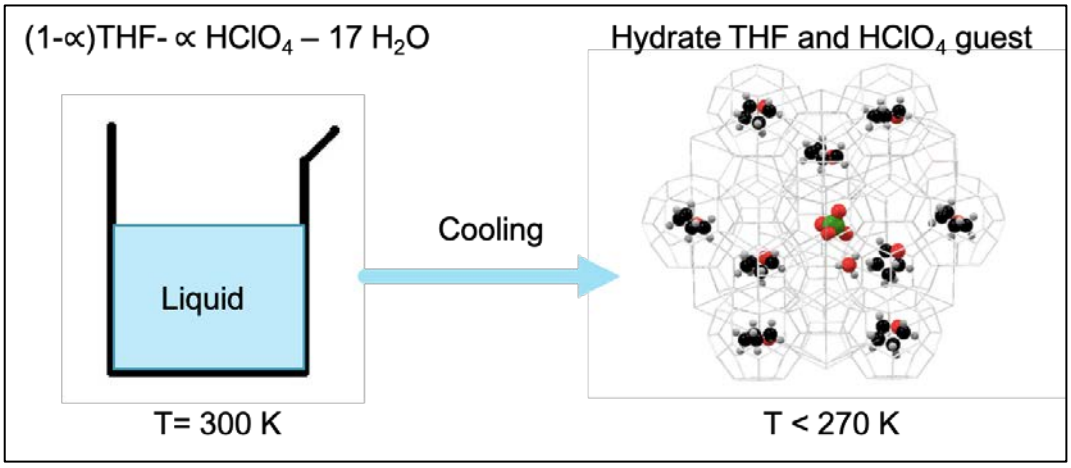

Figure II. 1. Illustration of the sample preparation.

Depending on the experimental analyses, we will also specify how the samples were cold transferred and the set-ups used to guarantee the sample's integrity during the experiments.

2. Raman spectroscopy

i. Principle

Raman spectroscopy is a non-destructive technique, based on the detection of inelastic scattered photons following the interaction of the sample with a monochromatic light beam. The incident photons are scattered in all space directions with a total intensity 10^{-3} to 10^{-4} lower than the incident beam. The scattered light is mainly composed of photons of the same wavelength as the incident one, this is the Rayleigh scattering (elastic). A tiny part of the scattered beam (typically 10^{-7} %) is scattered at a different wavelength, this polychromatic beam is called Raman scattering. The difference of energy between the incident photon and the scattered photon corresponds to the difference in energy between the initial and final states of the samples and provides information on the excitation spectrum of the sample. Typically, this corresponds to the vibrational excitations of the sample and can be used to get information on the chemical nature of the probed molecule. Raman scattering is observable

with incident wavelengths (laser source) ranging from UV to near IR, through the visible.

The Raman effect is based on the interaction between the "electron cloud" of the sample and the external electric field of the monochromatic light, which can create an induced dipole moment within the molecule based on its polarizability.

Under the external electric field $\vec{E}$ of the incident light, the molecules will be at the origin of an induced dipole moment $\vec{P}$ through the polarizability tensor $\bar{\bar{\alpha}}$.

$$\vec{P} = \bar{\bar{\alpha}}\vec{E} \qquad (II.3)$$

The incident electric field $\vec{E}$ is characterised by its amplitude E_0 and it frequency υ_0 which can be written as:

$$\vec{E} = \overrightarrow{E_0}.\cos(2\pi\upsilon_0 t) \qquad (II.4)$$

The polarizability tensor $\bar{\bar{\alpha}}$ express the deformation properties of the molecular electronic cloud under the electric field. This rank 2 tensor depend on the molecule geometry. The vibration coordinates are then defined by:

$$Q = Q_0.\cos(2\pi\upsilon_Q t) \qquad (II.5)$$

In the harmonic approximation, the polarizability tensor $\bar{\bar{\alpha}}$ is express as following with $\overline{\overline{\alpha_0}}$ the molecular polarizability at equilibrium.

$$\bar{\bar{\alpha}} = \overline{\overline{\alpha_0}} + \left(\frac{\delta\bar{\bar{\alpha}}}{\delta Q}\right)_{Q=0}.Q \qquad (II.6)$$

The induced dipole moment $\vec{P}$ depend on the vibration coordinate Q. Combining the equation (2), (3), (4) and (5), one obtain:

$$\vec{P} = \overline{\overline{\alpha_0}}\overrightarrow{E_0}\cos(2\pi\upsilon_0 t) + \frac{1}{2}\left(\frac{\delta\bar{\bar{\alpha}}}{\delta Q}\right)_{Q=0} Q\overrightarrow{E_0}\left[\cos\left(2\pi(\upsilon_0+\upsilon_Q)t\right) + \cos\left(2\pi(\upsilon_0-\upsilon_Q)t\right)\right] \qquad (II.7)$$

Within a quantum mechanics description, the molecule is excited by a photon of energy $h\upsilon_0$ to a virtual metastable state to fall back in vibrational levels. The allowed level can be the same as the starting level, meaning the scattered frequency is the same as the incident one (i.e. Rayleigh scattering). However, if the end level has higher or lower energy than the starting level, we talk about Raman Stokes and Raman Anti-Stokes, respectively (Figure II. 2). The colours in the dipole moment equation (5) match the colours of the phenomena in Figure II. 2.

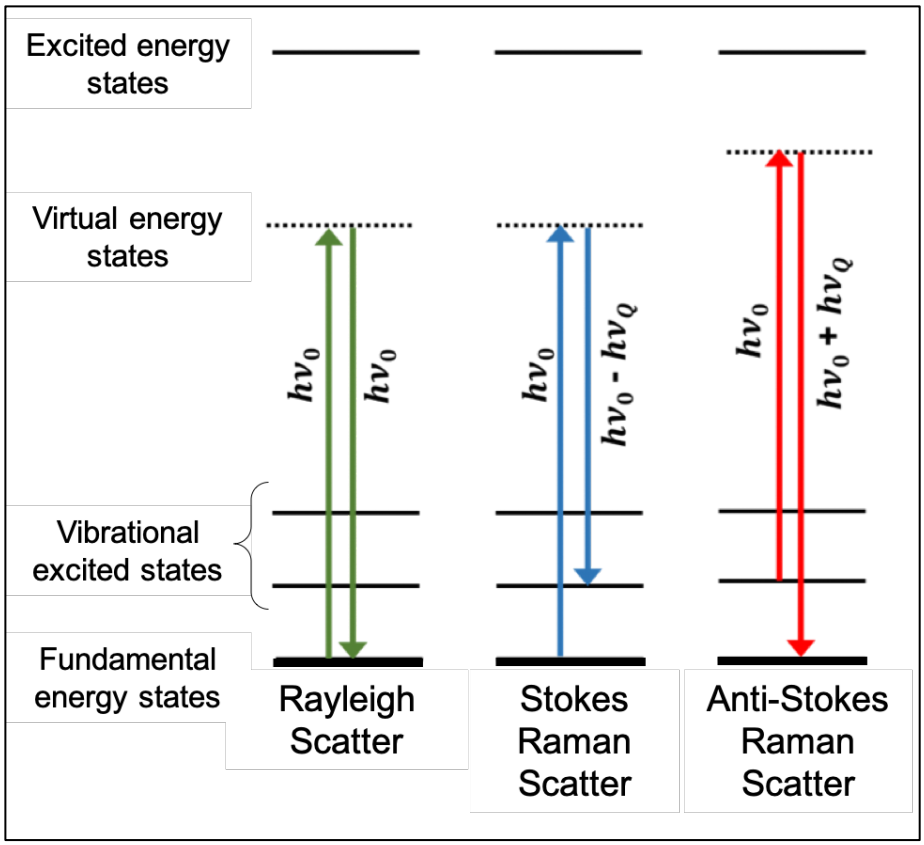

Figure II. 2. Representation of the various scattering phenomena.

The transition vibration modes are said to be active (detectable) in Raman if the molecular polarizability changes with the excitation of that particular mode (Equation (7)). In the case of the harmonic oscillator, the vibrational transition needs to obey $\Delta\upsilon = \left|\upsilon_0 - \upsilon_Q\right| = \pm 1$, where υ is vibrational quantum number.

$$\left(\frac{\delta\bar{\bar{\alpha}}}{\delta Q}\right)_{Q=0} \neq 0 \qquad (II.8)$$

An analysis of the molecular symmetries allows to predict which vibrational modes will be detectable.

The molecules mode give a certain frequency and the resulting scattered light will be collected by a detector (details of the set-up in the next part). The collected data will be given as an intensity according to the frequency, called a Raman spectra. The intensity of Raman scatter light is usually directly proportional to the number of molecules in the sample volume probed by the Raman instrument. With a calibration procedure, the intensity of a spectrum is then directly proportional to the concentration of the species. With mixtures, relative peak intensities provide information about the relative concentration of the components [PEL 03].

All materials can be analysed by Raman spectroscopy, whatever the state they are in (solid, liquid or gas) and without any particular preparation.

ii. Experimental details

The Raman spectrometer used during this study is an HR Evolution (Horiba Jobin Yvon) presented in Figure II. 3. The Raman spectroscopy technique uses a laser source (diode) with the incident wavelength $\lambda = 532\, nm$. The laser passes first through an interferential filter which is wavelength selective. With the help of various optical elements (mirrors and lens), the monochromatic light beam is focused on the sample to be studied. The scattered light goes through the same lens in the case of backscattering. As the Raman process is not very intense, a holographic filter of type ''notch'' or ''edge' ' is used to separate the scattered signal of interest from the much more intense Rayleigh signal. The scattered light meets another lens and passes through a Pinhole (150 μm, in our case). The light is then diffracted by a grating. The size of the grating determined the spectral resolution of the Raman spectra. A better resolution is obtained with higher grating which will better diffract the light but the spectral acquisition will take longer due to the limited detector's surface. The intensities are

measured with a multichannel CCD detector, cooled by Peltier effect at 200 K (-70 °C), allowing to recover the data after the transformation of the light signal to electric signal.

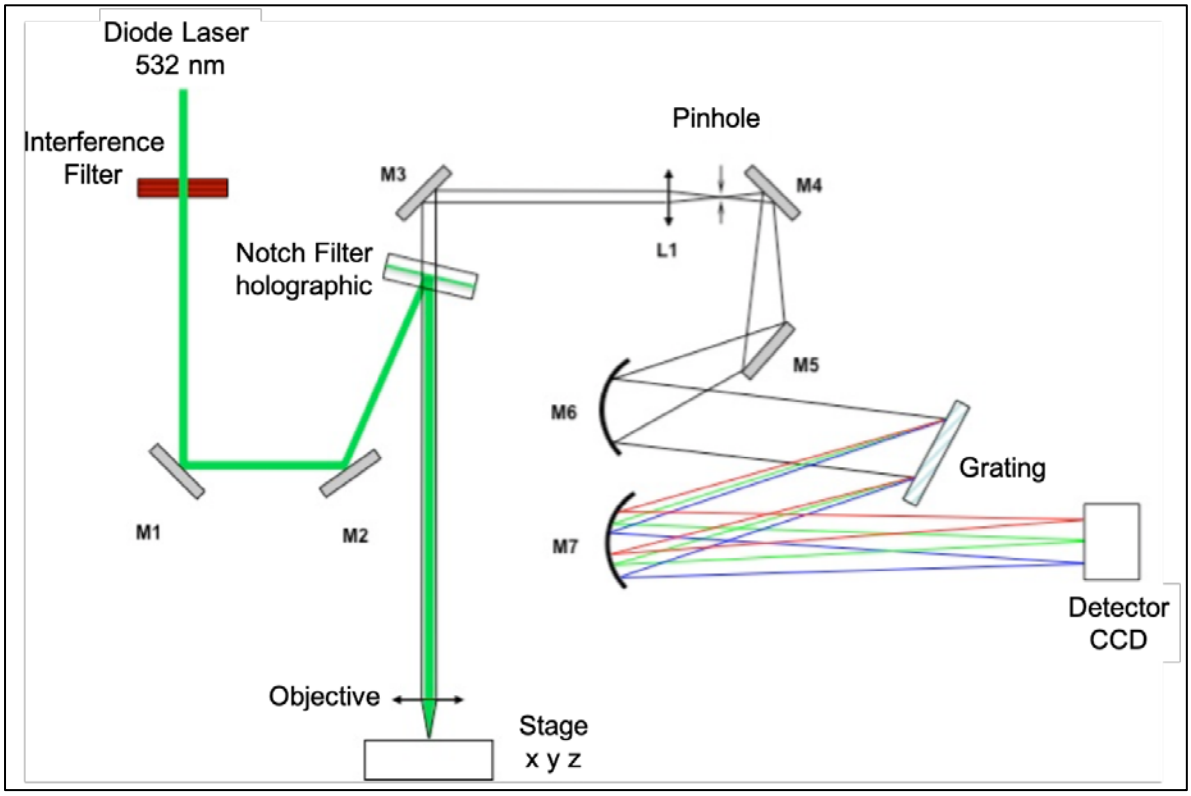

Figure II. 3. Sketch of the Raman spectrometer LabRam HR evolution (Horiba Jobin Yvon, France) [PET 17 a].

Depending on the grating, the spectral resolution RS varies. The spectral resolution is inversely proportional to the number of lines N in the diffraction grating and to the focal F of the monochromator.

$$RS \propto \frac{1}{N.F} \qquad (II.9)$$

The spectral resolution becomes better as the focal length of the monochromator increases, as well as with the number of features of the diffracting grating. The measurement procedure is sequential: it is necessary to rotate the grating to change the wavelength detected on the

CCD device. A calibration is needed before every experiment with the silicon sample possessing a vibration mode at 520.7 cm^{-1}.

The set-up of the spectrometer coupled with an optical microscope adds experimental parameters that we need to consider. When the beam is focalized on the sample, the focal point is in fact a cylinder, also called «waist», because of diffraction effects. The focal volume is shown in Figure II. 4, characterised by its diameter d and length L that depend on the laser beam diameter D, its focal f and its incident wavelength λ. The sample refraction power also affects the shape of the «waist». The focal volume is determined by:

$$d = \frac{4\lambda f}{\pi D} \; and \; L = \frac{\pi d^2}{\lambda} \qquad (II.10)$$

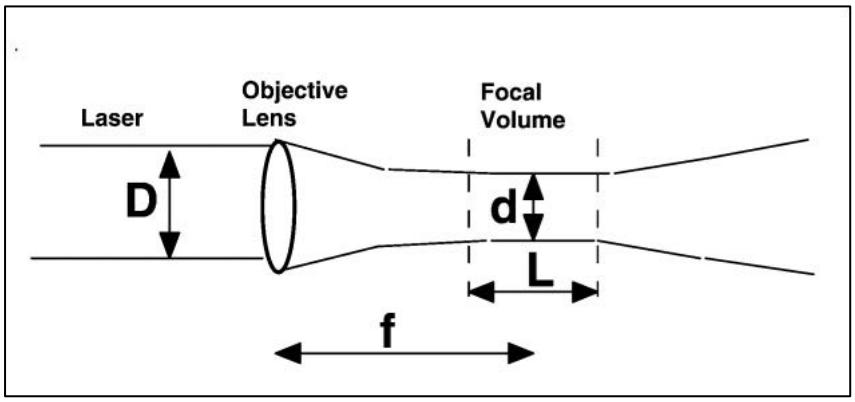

Figure II. 4. Shape of the focal volume called «waist».

Coupling the spectrometer to a microscopic confocal set-up improves the radial resolution. The radial resolution is determined by the Numerical Aperture (NA) of the lens. The NA is defined from the maximum angle of the demi-aperture α and the refractive index n, has:

$$\boldsymbol{NA} = n.\sin(\alpha) \qquad (II.11)$$

An increase in the numerical aperture leads to an increase in the splitting power of the lens d_{min}, also called the radial resolution:

$$d_{min} = 0.61\,\lambda/NA \qquad (II.12)$$

The spectrometer in a confocal set-up has many advantages such as the improvement of the radial and axial resolution. The depth of the «waist» or the focalisation is given by the following equation where n is the sample's refractive index:

$$\Delta Z = 1.4\,\lambda\, n/NA^2 \qquad (II.13)$$

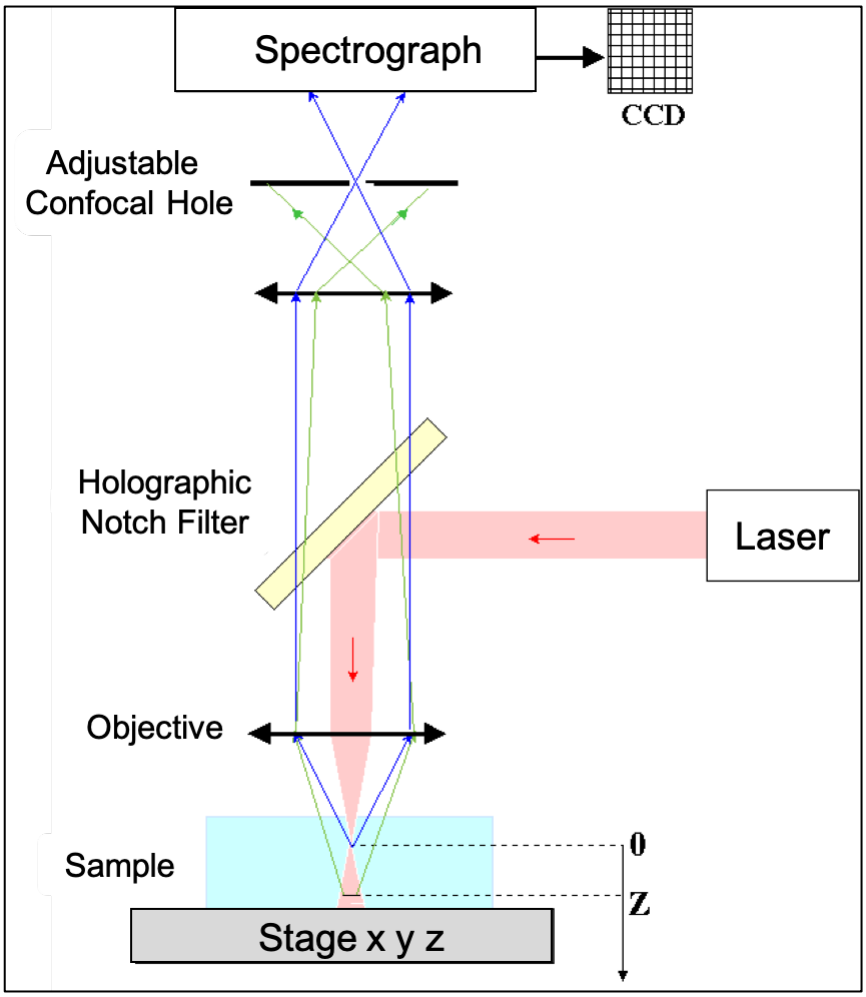

Figure II. 5. Confocal Raman Spectromety [PET 17 b].

The confocal set-up also cancels unwanted light from external origin (outside the focal volume). After passing through the lens and Notch filter, the scattered light from the sample, is spatially filtered by an adjustable confocal hole of small diameter placed at the confocal

image plane of the microscope (see Figure II. 5). This spatial filter allows to detect only the signals from the confocal plane and blocks the scattered light, as well as to limit the fluorescence and luminescence from sample regions outside the focal volume. The confocal technique allows to focus on the desired signal, increasing the contrast for a better study of the sample at a micrometer scale. The best resolution is obtained when the confocal hole is the smallest; however, by decreasing the size of this hole, we might decrease significantly the intensity of the signal arising from the sample. The aperture of the confocal hole also determines the axial resolution. Therefore, a compromise needs to be made for an optimum resolution without losing scattered local information when using the confocal set-up.

In our setup, the incident laser beam was focused onto the sample through a microscope with a 50× objective with NA = 0.55 (Olympus), allowing the sample to be probed with a micrometric spatial resolution. Scattered light was dispersed by a 600 grooves/mm holographic grating system and collected in the backscattered geometry with a CCD detector. The spectral resolution was *ca.* 1.3 cm^{-1}.

The various hydrate samples in liquid state are cooled down into a glass cell placed into the cryogenic stage THM600 (Linkam Scientific Instrument Ltd., UK), in an inert nitrogen atmosphere. This allows the sample temperature to be controlled between 80 K to 300 K. The set-up is shown in Figure II. 6

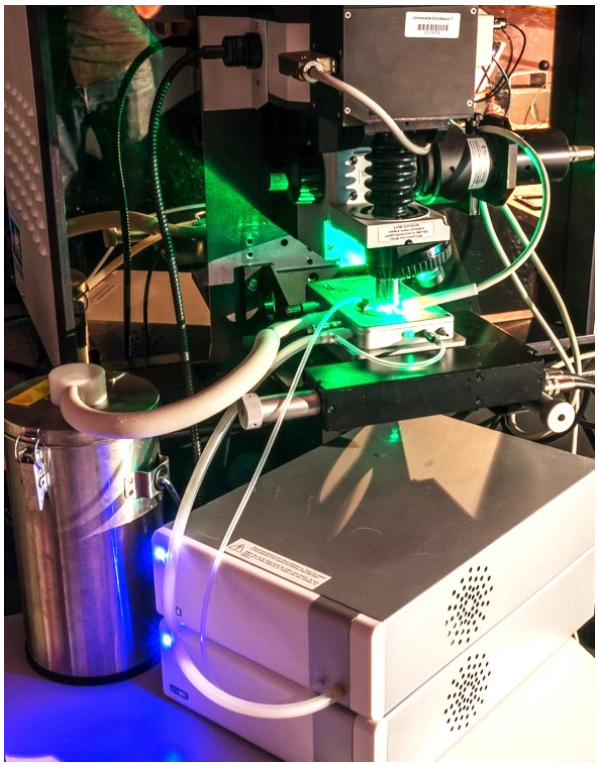

Figure II. 6. LinKam stage connected to temperature control system with nitrogen reservoir under Raman microscopic spectrometer objective.

Raman spectra were recorded under inert atmosphere for specific temperatures from 150K to 300K. The temperature control system allows a study of the samples' structural stability (structural change, melting temperature). We also performed Raman mapping in the (x y) plane of the sample surface thanks to the confocal set-up. The resulting spectra are called maps and are presented in Chapter IV.

3. X-Ray Diffraction.

i. Principle

The X-ray diffraction technique provides information on the crystalline structure of a sample. It allows the symmetry of the crystal to be identified and the lattice parameters to be determined. This analysis technique is based on an elastic scattering phenomenon (without

energy loss). A monochromatic and parallel X-ray beam is considered. The wavelength of the X-rays is of the order of magnitude of the interatomic distances (a few Å). The X-rays are scattered by the electron cloud of the atoms and interfere with each other. Their interference can be destructive or constructive. The flux of photons is collected as a function of their propagation direction in space or scattering angle θ. The scattering angles for which the different scattered beams are in phase (constructive interference) or diffracted satisfy Bragg's law.

$$2d \sin\theta = n\lambda \qquad (II.14)$$

where d is the inter-reticular distance (i.e. the distance between two reticular planes defined by the Miller indices (h k l)), θ is the diffraction angle, n is the diffraction order, and λ is the X-ray wavelength.

The collected data formed a diffractogram where the intensity I with respect to the position (2θ) is represented as $I = f(2\theta)$. The position (2θ), intensity I and width of the diffraction peaks provide structural information.

ii. X-ray diffraction Set-up

The X-ray diffraction was performed at the European Institute of Chemistry and Biology (IECB-University of Bordeaux) with the expert collaboration of Brice Kauffmann. The set-up used is a diffractometer $2\theta/\ 2\theta$ of Rigaku brand (Rigaku FRX 3kW) equipped with a microfocus rotating anode having a monochromatic radiation at the wavelength of copper Cu Ka (l=1.54 Å) and a Dectris Pilatus 200K detector (see Figure II. 7). Studies on capillaries were carried out under cryogenic conditions from 150K to 300K. The liquid sample of mixed hydrate of THF and $HClO_4$ were transferred by capillarity into quartz capillaries of 200 nm radius and then cooled down using liquid nitrogen and sealed with an oxygen and propane torch. Data processing was carried out using HighScore software (PANatycal).

Figure II. 7. Picture of the X-Ray Diffraction set-up used in IECB, France

X-ray diffraction is used in this work to determine the hydrate structure present in the samples of the mixed THF-$HClO_4$ hydrate with various $HClO_4$ acid fraction. The thermal structure stability has also been analyzed. In literature, the structure of THF-$17H_2O$ and $HClO_4$-$5{,}5H_2O$ are well-known and formed, respectively, the SII and SI hydrate structure [CON 09] [MOO 87]. These hydrates are chosen as reference to test the cryostat and to identify the various crystalline structure. The results obtained for the structural investigation are presented in Chapter IV.

4. Impedance measurement

i. Principle

Electrochemical impedance spectroscopy (EIS) is a characterisation technique that allows the study of the impedance of a working cell at a steady state point. The principle consists of measuring the response of an electrochemical system to an alternating disturbance of variable frequency and low amplitude.

For this study, an alternative voltage $E_\omega = E_0 \exp(i\omega t)$, of small amplitude E_0 and variable angular frequency ω ($\omega = 2\pi\upsilon$ where υ is the frequency), is applied across the electrochemical cell. The alternative current (AC) $I(\omega) = I_0 \exp(i\omega t + \varphi)$ passing through the cell is measured. The impedance of the system, noted $Z(\omega) = |Z| \exp(-i\varphi)$, is then defined as the ratio of the applied voltage to the measured current:

$$Z(\omega) = \frac{E(\omega)}{I(\omega)} \qquad (II.15)$$

$Z(\omega)$ is a complex number which can be expressed in polar coordinates by its modulus $|Z|$ and its phase φ or in Cartesian coordinates by it real $Re(Z)$ and imaginary $Im(Z)$ parts:

$$Z(\omega) = Z' + iZ'' = |Z| \cos\varphi + i|Z| \sin\varphi \qquad (II.16)$$

Several representations exist to describe the impedance (Nyquist representation, Bode representation...). The one used for the measurements carried out on our electrolyte is the representation of the impedance in the Nyquist complex plane where, at each frequency, the opposite of the imaginary part of the impedance $-Z''$ is plotted as a function of the real part Z' in an orthonormal reference frame: $-Im(Z) = f(Re(Z))$. The impedance vector, as a function of the frequency, describes in the complex plane a curve characteristic for the studied system. It is from this diagram that the resistance R_e of the electrolyte, and thus its electrical (ionic) conductivity σ_e, can be determined by the following relation:

$$\sigma_e = \frac{1}{R_e} . \frac{l}{S} = \frac{1}{R_e} . K_{cell} \qquad (II.17)$$

where l and S are respectively the electrolyte thickness and the section. These parameters are specific for the cell used in the measurement, and can be group in the cell constant K_{cell}.

ii. Experimental conditions for low-temperature measurements.

In order to perform the conductivity measurements on the mixed hydrate with various acid fraction at controlled temperatures, a dedicated cell was developed at the Institut des Sciences Moléculaires (UMR5255 CNRS – Univ. Bordeaux) by digital cutting with the help of Julien Sanchez. The resulting home-made cell, in Teflon with silver electrodes of size (3x10x2.5 mm) and set-up as shown in Figure II. 8.

Before using the cell with the hydrate samples, the resistivity of the cell, called the cell constant, needs to be determined. The nature of the cell (Teflon), as well as the electrodes composition (silver) and its size influence the resistivity of the system. To know the cell constant characteristic, impedance measurements were done with a reference solution of KCl at a concentration of 0.1 mol/L. The resistivity $R_{KCl(exp)}$ and the literature well-known conductivity of KCl solution σ_{KCl} allows to find the value of the cell constant K_{cell} corresponding to the particular geometry of our home-made cell.

$$K_{cell} = \frac{\sigma_{KCl}}{R_{KCl(exp)}} \qquad (II.18)$$

The various hydrate sample are transferred in liquid state between the two silver electrodes of thickness 0.15 mm. To avoid leaks the core cell is shaped from a Teflon sheet of 3mm thickness. The cell has a size of 3x10x2.5 mm to fit into the cryogenic stage THM600 (Linkam Scientific Instrument Ltd., UK). To connect the cell to the EIS instruments, a special connection box previously designed by Sarah Desplanche and Julien Sanchez was used [DES 19].

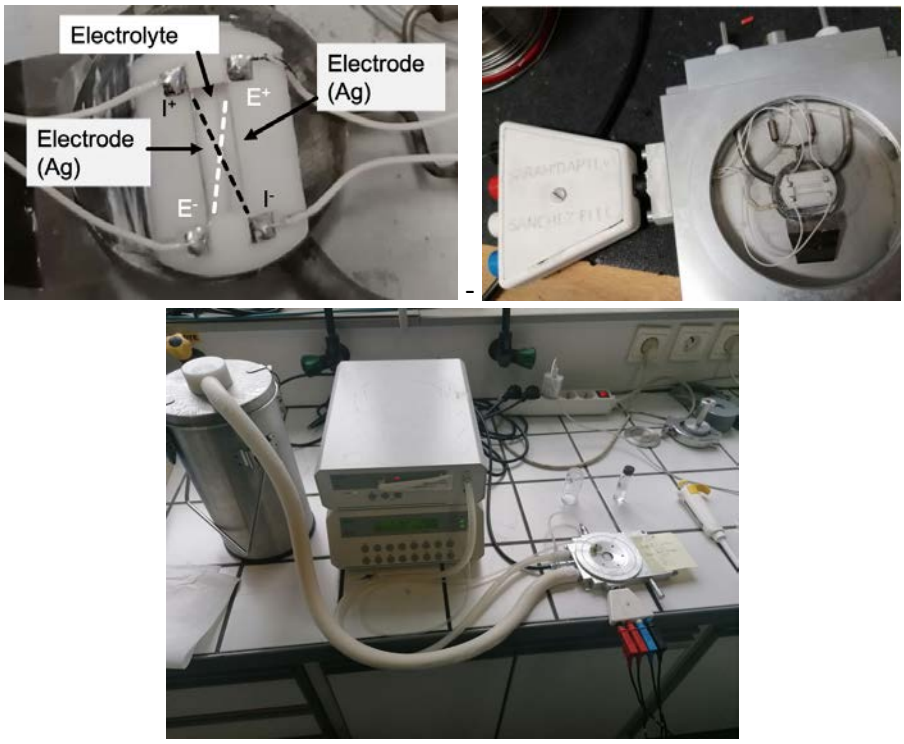

Figure II. 8. Impedance measurement, from left to right, Cell – Cell in LinKam with connection box [DES 19]- LinKam connected to nitrogen.

The protonic conductivity is measured in a two electrodes configuration, called “fake 4 points”. The measurements are made using an Autolab PGSTAT 302 equipped with a frequency response analyzer (FRA) in the range 10 Hz to 100 Hz with an amplitude signal of 50 mV and a continuous courant intensity of zero. The data were recorded at temperature from 150 K to 300 K in 10 K steps and a stabilization time of 30 minutes at each temperature.

For each temperature, the impedance diagram in the Nyquist plane is obtained as shown in the example of Figure II. 9. The sample’s resistance R_e is determined when the imaginary part of the Impedance is zero.

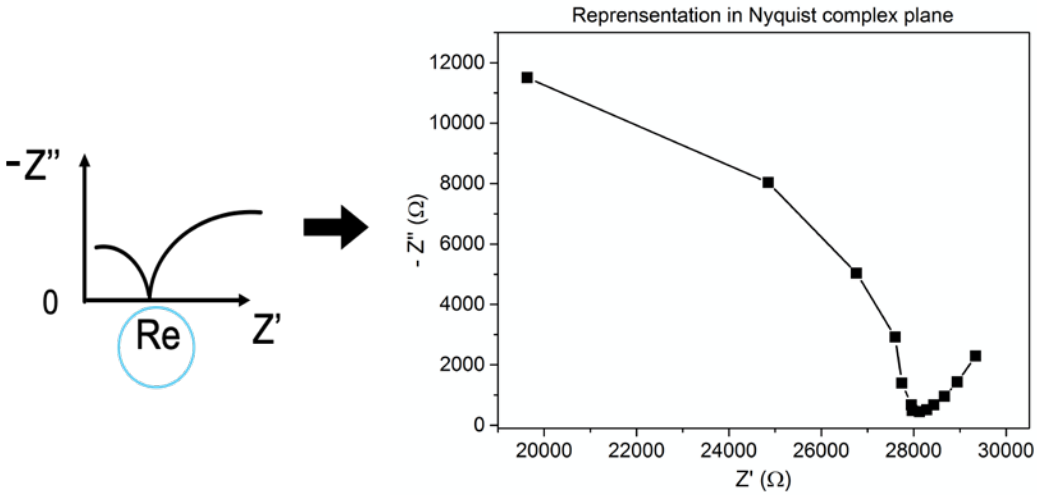

Figure II. 9. Left. Determination of the resistivity. Right. Example of Impedance diagram obtained for the mixed hydrate THF-HClO4 at acid fraction 2.7 %mol at 170 K.

As indicated in the figure, the resistance is found when the impedance curve cuts the horizontal axis: $-Im(Z) = 0 = f(Re(Z))$. The conductivity σ_e is then determined for the sample studied from the following equation with the cell constant K_{cell} determined with the reference solution and the resistivity $R_{e(exp)}$ of the sample.

$$\sigma_e = \frac{K_{cell}}{R_{e(exp)}} \qquad (II.19)$$

The study of the impedance diagram allows to determine the protonic conductivity of the mixed hydrate with various acid fractions at various temperatures. The obtained data are discussed in Chapter V.

B. Modelling strategy

1. Density Functional Theory simulation

Density Functional Theory calculations were done using the SIESTA program. SIESTA is both a method and its computer program implementation, to perform efficient electronic structure calculations and ab initio molecular dynamics simulations of molecules and solids.

i. Basic Principle: From Quantum Machanics to Density Functional Theory

When performing quantum mechanics calculations, we look for solutions to the Schrödinger Equation, most commonly, the non-relativistic, time-independent Schrodinger equation (TISE)

$$\hat{H}\psi = E\psi \qquad (II.20)$$

where $\hat{H}$ is the Hamiltonian, a differential operator that represents the total energy of the system, and the wave function ψ are a set of eigenfunctions that are solutions of the corresponding differential equation. The solutions ψ are usually referred to as eigenstates. Each eigenstate ψ_n has a corresponding eigenvalue called E_n , which is a real number. $E_n$is the energy of the system in a state described by the wavefunction ψ_n.

The TISE provides a lot of information about the system, such as the kinetic energies and potential energies for all particles and the most stable geometry of the system in its ground state, as well as information about the energies and character of the electronic and vibrational excitations. The details of the Hamiltonian depend on the system we wish to describe. It is only possible to solve this equation exactly for very simple systems like a single particle in a box. However, for systems like molecules, where many electrons are interacting with many nuclei and among them, the solution is much more complicated. The Hamiltonian is

$$\hat{H} = -\mathrm{KE}_{elec} - \mathrm{KE}_{nucl} - \text{Nucl.-Elec.}_{\text{attract.}} + \text{Elec.-Elec.}_{repuls.} + \text{Nucl..-Nucl.}_{repuls.} \qquad (II.21)$$

where the kinetic energies of the electrons and nuclei are noted KE_{elec} and KE_{nucl}respectively,

and the potential energies include the Coulomb attraction between electrons and nuclei, and the corresponding electron-electron and nucleus-nucleus repulsion. To solve such Hamiltonian, all interactions and the concerted dynamics of electrons and nuclei must be considered simultaneously, which is quite complicated. Thus, it is necessary to perform crucial simplifications. A very standard one is the so-called Born-Oppenheimer Approximation, which derives from a simple but powerful observation. The mass of an electron is smaller than that of a nucleus by at least three orders of magnitude. This implies that, according to the classical definition of kinetic energy, with a comparable value of the kinetic energy, the electrons are around thirty times faster than nuclei:

$$velocity = \sqrt{\frac{2E_{KE}}{mass}} \qquad (II.22)$$

Therefore, from the electrons perspective, nuclear positions appear as static or very slowly changing. On the contrary, from the nuclear perspective, electron positions are updated almost instantaneously. This sets two different time scales for the electron and nuclear dynamics, which can be considered approximately decoupled. This allows simplifying the problem, which can be split into an electronic part and a nuclear part that can be solved separately. Furthermore, given their large mass, nuclei are frequently treated as classical particles. In such scheme, the quantum electronic problem is solved by treating the nuclei as classical particles at well-defined, fixed positions. This solution is repeated as a function of the nuclear positions, i.e., as they slowly change along their classical trajectory. The energy of the system can then be mapped as a function of the nuclear coordinates to produce a potential energy surface. The motion of the nuclei can be obtained using such potential energy surface, e.g., nuclear positions can be optimized in such potential to obtain the most stable molecular geometry. The separation of the electronic and nuclear part is known as the Born-Oppenheimer Approximation that, as explained above, is usually combined with a classical treatment of the massive nuclei.

To solve the quantum electronic problem, we can concentrate in the electronic part of the Hamiltonian, for which we disregard the negligible kinetic energy contribution of the nuclei.

Since the nuclei are considered at fixed positions, the constant Coulomb repulsion term between nuclei can be added at the end of the calculation. Thus, we can define a Hamiltonian for the electrons as:

$$\widehat{H_{elec}} = \hat{T} + \widehat{V_{Ne}} + \widehat{V_{ee}} \qquad (II.23)$$

with $\hat{T}$ the kinetic energy of the electrons, $\widehat{V_{Ne}}$ is the electrostatic attraction of the electrons to the nuclei and $\widehat{V_{ee}}$ is the electrostatic repulsion between electrons.

The solution to the Schrödinger equation with an electronic Hamiltonian is the electronic wave function ψ_{elec} with the eigenvalues E_{elec}:

$$\widehat{H_{elec}}\,\psi_{elec}(\overrightarrow{r_1}, \dots, \overrightarrow{r_N}) = E_{elec}\,\psi_{elec}(\overrightarrow{r_1}, \dots, \overrightarrow{r_N}) \qquad (II.24)$$

The electronic wave function ψ_{elec} depends on the electron's spatial coordinates and spin, although for simplicity the electron spin is neglected in the discussion below. The electronic wave function giving the lowest energy is called the ground state of the system, and its eigenvalue E_{elec} is the ground-state energy. However, the electronic wave function of a many electron system is hard to compute. Due to the electron-electron interaction term, $\widehat{H_{elec}}$ described a many-body problem where each electron experiences simultaneously the electrostatic repulsion from all other electrons, i.e., the movements of all the electrons in the system are correlated.

The wave function cannot be directly measured but the probability of finding our *N* electrons at a particular set of coordinates when our system is in a state ψ is given by:

$$|\psi(\overrightarrow{r_1}, \dots, \overrightarrow{r_N})|^2 = \psi^*(\overrightarrow{r_1}, \dots, \overrightarrow{r_N})\psi(\overrightarrow{r_1}, \dots, \overrightarrow{r_N}) \qquad (II.25)$$

It is interesting to notice here that, if we would switch off the electron-electron repulsion term, the electrons would move as independent particles and the wave function could be approximated as a product of single-particle wave-functions for individual electrons. This is

the so-called Hartree product. However, we also need to take into account that electrons are indistinguishable particles and fermions, i.e., they obey the Pauli exclusion principle. Therefore, any physically meaningful many-electron wavefunction must change sign when the coordinates of any two electrons r_i through r_j are exchanged. Such a properly antisymmetrized version of the Hartree product can be obtained using the so-called Slater determinant construction, and provides the wavefunctions used in the Hartree-Fock theory. At first, it might seem that a solution of the problem based on the assumption of a negligible interaction between electrons cannot be very useful to study any realistic situation. However, quite on the contrary, Hartree-Fock theory and other mean-field theories provide a good starting point to understand the electronic structure of materials. The key idea here is that, rather than neglecting the electron-electron interactions, we replace the many-electron repulsion term by an effective potential that includes the average effect of that repulsion. As an obvious first approximation, we can take the electrostatic potential (usually called Hartree potential in this context) created by the electron density for such an effective potential,

$$V_{eff}(\vec{r}) \approx V_H(\vec{r}) = \frac{1}{4\pi\epsilon_0}\int dr_2^3 \ \frac{\rho(\vec{r}_2)}{|\vec{r}-\vec{r}_2|} \qquad (II.26)$$

with the electron density $\rho(\vec{r})$ given by

$$\rho(\vec{r}) = \int dr_2^3 \ldots \int dr_n^3 \ |\psi(\vec{r}, \overrightarrow{r_2} \ldots, \overrightarrow{r_N})|^2 \qquad (II.27)$$

and the electronic Hamiltonian takes the form

$$\hat{\mathrm{H}}_{elec} \approx \sum_{i=1}^{N} \hat{T}_i + \ \hat{V}_{Ne}(\overrightarrow{r_i}) + \hat{V}_{eff}(\overrightarrow{r_i}) = \ \sum_{i=1}^{N} \hat{H}_{elec}^{eff}(\overrightarrow{r_i}) \qquad (II.28)$$

Interestingly, now the approximate many-body Hamiltonian becomes the sum of N identical copies of an effective single-electron Hamiltonian, N being the number of electrons in the system. Using a properly antisymmetrized product of the solutions of this effective Hamiltonian we can construct an approximate many-electron wavefunction

$$\psi(\overrightarrow{r_1}, \ldots, \overrightarrow{r_N}) = \mathcal{A}[\phi_1(\overrightarrow{r_1}).\phi_2(\overrightarrow{r_2}).\phi_3(\overrightarrow{r_3}) \ldots \phi_N(\overrightarrow{r_N})] \qquad (II.29)$$

with $\mathcal{A}$ the antisymmetrizing operator and the ϕ_i satisfy

$$\hat{H}_{elec}^{eff}(\vec{\mathrm{r}})\phi_i(\vec{\mathrm{r}}) = \varepsilon_i\phi_i(\vec{\mathrm{r}}) \qquad (II.30)$$

In particular, if we take the N lowest-energy single-electron orbitals (N/2 for a spin degenerate system) this will be an approximation to the many-electron ground-state wavefunction. It is also interesting to note that the effective potential that defines the effective single-electron Hamiltonian depends on the electron density (and in general on the orbitals $\phi_i(\vec{\mathrm{r}})$). This poses a problem because the electron density it is not known a priori. Therefore, the problem has to be solved self-consistently, i.e., we must find an effective potential that generates a collection of orbitals and a density that, in turn, produce the same effective potential. This non-linear problem is usually solved iteratively: we start with an initial guess for the density and the effective potential; we solve for the corresponding single-electron orbitals and, with these solutions, we find a new density that usually differs from the previous one; this information is used to generate a new effective potential, and the process is iterated until the input and output orbitals and density are identical.

The Hartree-Fock theory is an example of such a mean-field theory. In the case of Hartree-Fock we assume that the many-electron wavefunction takes the form of an antisymmetrized Slater determinant $\mathcal{A}[\phi_1(\vec{r_1}).\phi_2(\vec{r_2}).\phi_3(\vec{r_3})\ldots\phi_N(\vec{r_N})]$ and request that it minimizes the total energy defined as the expected value of the original many-electron Hamiltonian $\hat{\mathrm{H}}_{elec}$. This variational procedure gives rise to the so-called Hartree-Fock equations in which the effective potential $\hat{V}_{eff}(\vec{\mathrm{r}})$ includes a non-local exchange term $\hat{V}_{ex}(\vec{r},\vec{r}')$ in addition to the local electrostatic potential

$$\left[\hat{T} + \hat{V}_{Ne}(\vec{\mathrm{r}}) + \hat{V}_H(\vec{\mathrm{r}})\right]\phi_i(\vec{r}) + \int dr'^3\,\hat{V}_{ex}(\vec{r},\vec{r}')\phi_i(\vec{\mathrm{r}}') = \varepsilon_i\phi_i(\vec{\mathrm{r}}) \qquad (II.31)$$

where

$$V_{ex}(\vec{r},\vec{r}') = \frac{-1}{4\pi\epsilon_0}\frac{\rho^{HF}(\vec{r},\vec{r}')}{|\vec{r}-\vec{r}'|} \qquad (II.32)$$

and the density matrix is constructed from the N lowest (occupied) single-electron orbitals

$$\rho^{HF}(\vec{r},\vec{r}') = \sum_{i=1}^{N} \phi_i^*(\vec{\mathrm{r}})\phi_i(\vec{\mathrm{r}}') \qquad (II.33)$$

It is interesting to notice that, among other things, the exchange term leads to a self-interaction free theory, in which a given electron does not feel the repulsion created by its own charge distribution.

In recent years, the Density Functional Theory (DFT) method for electronic structure calculations has gained a lot of popularity to study large molecules and solids. This is mostly due to its computational efficiency as compared to high-level many-body methods and even compared to Hartree-Fock. The idea behind DFT is that the ground-state electron density $\rho_{GS}(\vec{r})$ contains enough information to compute the properties and the energy of the ground state of a given system. Obviously, $\rho_{GS}(\vec{r})$ is a much simpler object than the many-body wavefunction. Furthermore, in principle DFT has a solid foundation that rest on two fundamental mathematical theorems by Kohn and Hohenberg [HOH64]:

1. The ground-state energy E_{GS} of a system is a unique functional of the electronic density

$$E_{GS} = E[\rho_{GS}(\vec{r})] = F[\rho_{GS}(\vec{r})] + \int d\vec{r}^3 \;\; V_{ext}(\vec{r})\rho_{GS}(\vec{r}) \qquad (II.34)$$

where $F[\rho(\vec{r})]$ is a universal functional and $V_{ext}(\vec{r})$ is the potential that characterizes the system, e.g., usually the attraction of the electrons by the static classical nuclei.

2. The electron density that minimizes the energy of the functional is the true electron density of the ground-state, corresponding to the full solution of the Schrödinger equation.

The Density Functional Theory principle is reducing the quantum problem of solving the

Schrödinger equation from finding a function of 3N variables, the many-electron wave function, to finding a function of only 3 variables, the electron density, independently of the system size (see Figure II. 10).

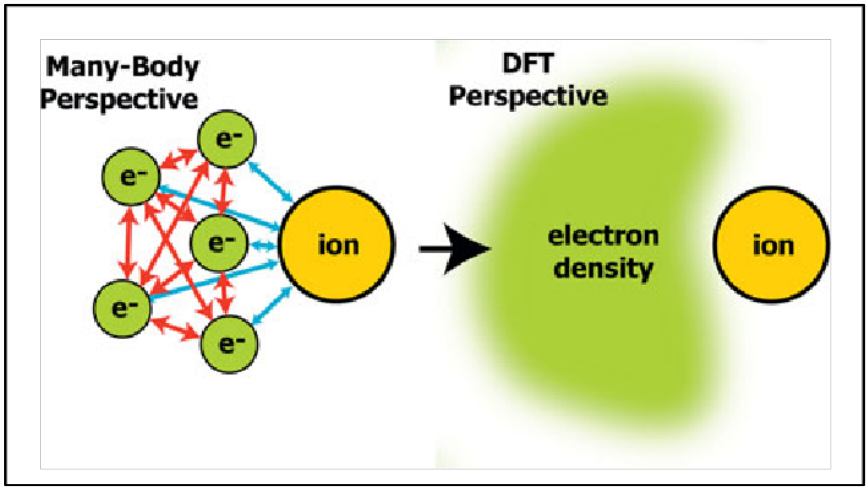

Figure II. 10. Density Functional Theory principle.

The universal functional $F[\rho(\vec{r})]$ contains information about the kinetic energy and the electron-electron repulsion. It is customary to divide this functional into a kinetic energy, a classical electrostatic and an exchange-correlation contributions

$$F[\rho(\vec{r})] = E_{kin}[\rho(\vec{r})] + \frac{1}{8\pi\epsilon_0}\int dr_1^3 \int dr_2^3 \frac{\rho(\vec{r}_1)\rho(\vec{r}_2)}{|\vec{r}_1 - \vec{r}_2|} + E_{XC}[\rho(\vec{r})]\,. \qquad (II.35)$$

DFT is, in principle, an exact method. Unfortunately, neither the kinetic energy nor the exchange-correlation energy can be easily obtained from the density and the exact expressions of the functionals are unknown. Therefore, it is necessary to use approximate expressions. This is particularly involved in the case of the kinetic energy contribution. A practical solution to this problem was given by Kohn and Sham [KOH65]. In Kohn-Sham approach the many-electron problem is mapped into a problem of independent electrons moving in an effective potential that contains the effects exchange and correlation. Within

such an approximation, the kinetic energy term is approximated by the kinetic energy of a collection of independent electrons, with further corrections to the kinetic energy being included in the so-called exchange-correction functional. The exchange-correlation remains to be defined in this approach. However, as discussed below, some approximations can be obtained for this quantity.

Thus, according to the description above, in Kohn-Sham method the universal density functional reads

$$F[\rho(\vec{r})] = \frac{-\hbar^2}{2\mathrm{m}_e}\sum_{i=1}^{N}\int d\vec{r}^3\, \phi_i^*(\vec{r})\,\nabla^2\phi_i(\vec{r}) + E_H + \tilde{E}_{XC}[\rho(\vec{r})] \qquad (II.36)$$

where m_e is the electron mass, N is the number of electrons, the $\phi_i(\vec{r})$ are the N lowest energy Kohn-Sham orbitals (see below), E_H is the electrostatic (Hartree) energy of the electron density and $\tilde{E}_{XC}[\rho(\vec{r})]$ is the exchange-correlation potential. Here, in addition to the effects of exchange and the correlation motion of electrons on the interaction energy, $\tilde{E}_{XC}[\rho(\vec{r})]$ also contains many-body corrections to the kinetic energy of the electronic system. The Kohn-Sham orbitals are single-electron wavefunctions found as solutions of the following Schrödinger-like equation,

$$\left[\frac{-\hbar^2}{2\mathrm{m}_e}\nabla^2 + V_{ext}(\vec{r}) + V_H(\vec{r}) + V_{XC}(\vec{r})\right]\phi_i(\vec{r}) = \varepsilon_i\phi_i(\vec{r}) \qquad (II.37)$$

where $V_{XC}(\vec{r})$ is the exchange-correlation potential, obtained as the functional derivative of the corresponding energy with respect to the density $V_{XC}(\vec{r}) = \frac{\delta\tilde{E}_{XC}[\rho(\vec{r})]}{\delta\rho(\vec{r})}$. The Kohn-Sham equation is obtained by minimizing the total energy of the system with respect to Kohn-Sham orbitals. In principle, under very general conditions, if the exact exchange-correlation functional would be known, the ground-state density can be obtained from the N lowest Kohn-Sham orbitals, $\rho_{GS}(\vec{r}) = \sum_{i=1}^{N}\phi_i^*(\vec{r})\,\phi_i(\vec{r})$.

As commented above for the Hartree-Fock method and, in general, for so-called mean-field schemes, the solution of the Kohn-Sham equation requires applying a self-consistent condition. To solve the Kohn-Sham equation, we need to find the Hartree and exchange-correlation potential. However, to find those potentials we need the electron density, which is computed from the Kohn-Sham orbitals. Thus, we need to use an iterative method where a first trial electron density is determined (step1), then the Kohn-Sham equation is solved with this electron density (step 2). We recomputed the electron density with the newly obtained Kohn-Sham orbitals (step3). We compare this output electron density to the initial one, if they differ more than a certain threshold value the electron density is updated (usually mixing the input and output densities) and we repeat steps 1, 2 and 3 again with the new electron density. Eventually, if we are sufficiently lucky and our mixing scheme was properly chosen, the input and output densities only differ by a negligible amount and we can consider the process to be converged. In such case, we say that the self-consistency condition has been reached.

The exact form of the exchange-correlation term being unknown, different functional forms has been proposed over the years and optimized depending on the studied systems. The most pertinent ones for hydrate systems will be presented in part 2.i

ii. SIESTA particularities

SIESTA is a pseudopotential-based density functional theory (DFT) software whose strength lies in the use of strictly-localised atomic-orbitals as a basis set [SOL 02]. SIESTA uses atomic orbitals with finite support. The use of orbitals with a finite range is key for the efficiency of the method and the favorable scaling of the calculations (see below). SIESTA is specifically designed and optimized to deal with large simulation cells containing hundreds or thousands of atoms. The utilized basis set can contain multiple-zetas (different radial functions to represent the orbitals corresponding to a given atomic shell), polarization orbitals (orbitals with angular momenta larger than occupied in the atomic ground-state), and off-site orbitals

(orbitals not centered at atomic positions). Therefore, it is possible to use from small (so-called minimal) basis, that allow computing very large systems, to quite complete basis sets, in principle capable of producing results of a quality comparable to plane-wave methods (an example of an widely used plane-wave method is VASP, Vienna Ab-initio Simulation Package [KRE 96].

SIESTA implements density functional theory with the standard Kohn-Sham formulation briefly described above. Using of strictly-localized atomic orbitals, it is possible to effectively tune the balance between accuracy and computational cost, and efficiently treat large systems. In particular, the use of finite support orbitals leads to sparse Hamiltonian and overlap matrices, thus enabling the use of reduced-scaling methods. In fact, the construction of the Hamiltonian from the density matrix in SIESTA is always done linear-scaling algorithms, i.e., the computational cost of this operation scales linearly with the number of atoms in the system. For wide band-gap materials it is also possible to solve the Hamiltonian in a linear-scaling fashion. However, this entitles a delicate and fairly unstable iterative procedure. For this reason, for the sizes of the systems considered here we find it more convenient to use standard diagonalization techniques to solve the Hamiltonian.

The functionalities of SIESTA include, amongst others, the calculation of energies and forces, density distributions, band structures and (projected) densities of states. It is possible to perform molecular-dynamics and real-time time-dependent DFT simulations. SIESTA is also coupled to the TranSIESTA method [BRA 02], allowing to perform calculations with open boundary conditions and for electron transport properties using the non-equilibrium Green's function formalism. SIESTA implements many different density-functionals including van der Waals corrected functionals and, in the latest development version, hybrid functionals. The spin-orbit coupling and a Hubbard U term (DFT+U) for correlated systems can be included. The newest development versions also include the possibility of using density-functional perturbation theory to compute phonons. SIESTA has been used in a wide range of applications, encompassing materials science, nanotechnology, catalysis, biological sciences (including interaction between organic and inorganic materials), geology and materials under high pressure, materials for nuclear reactors, and astrophysical and atmospheric systems.

Two types of files are necessary to run a SIESTA simulation. The main input file is in the so-called "Flexible Data Format" and has a .fdf extension. This file contains all the information about the system under consideration (number of atoms, chemical species, atomic coordinates, etc..), as well as information about the technical parameters of the simulation: basis set, density functional, number of k-points, values of the different parameters determining the accuracy and the self-consistency thresholds, etc. In the FDF format, the different inputs are identified by a label and, thus, can appear in an arbitrary order in the input file. In fact, most of the technical parameters have appropriate default values that are used by the code if the corresponding value does not appear in the input file. The other files needed are those containing the different pseudopotentials, one for each chemical species.

DFT calculations were carried out for the hydrate structure with impurities in the case of HPF_6 hydrate and for different types of guest molecules in the case of the mixed hydrate THF-$HClO_4$.

2. Input Method

i. Siesta parameters

(1) Exchange-correlation density Functional

In practical DFT calculations different approximations can be used for the exchange-correlation functional. This is a crucial point because, depending on the system under study, some interaction needs to be better described than others and accuracy issues might become more important. The simplest family of functional are those based on the so-called Local Density Approximation (LDA), where the exchange-correction energy functional is assumed to depend only on the value of the electronic density at each point in space. The LDA functionals are parametrized using information about the exchange-correlation energy of the homogeneous electron gas at different values of the density n. If $\epsilon_{XC}^{hom}(n)$ is the exchange-

correlation energy per electron in a uniform gas as a function of its density parameter *n*, the exchange-correlation functional for the non-uniform system can be defined as

$$E_{XC}^{LDA}[\rho(\vec{r})] = \int d\vec{r}^3\, \rho(\vec{r})\epsilon_{XC}^{hom}\big(\rho(\vec{r})\big) \qquad (II.38)$$

The corresponding exchange-correlation potential is easily evaluated since $\epsilon_{XC}^{hom}(n)$ is a normal function (not a functional) of the value of the density at each point and, therefore, the functional derivative corresponds to a standard derivative:

$$V_{XC}^{LDA}[\rho(\vec{r})] = \epsilon_{XC}^{hom}\big(\rho(\vec{r})\big) + \rho(\vec{r})\left.\frac{\partial\epsilon_{XC}^{hom}(n)}{\partial n}\right|_{n=\rho(\vec{r})} \qquad (II.39)$$

The homogeneous electron gas is a very convenient reference since several asymptotic behaviors are exactly known and, furthermore, it is possible to perform high-level numerical simulations that allow computing and parametrizing $\epsilon_{XC}^{hom}(n)$ with for a large range of densities [CEP 80]. LDA is also easy to implement and unexpensive to compute. In spite of this simplicity, LDA functionals can successfully describe the electronic properties of many systems, particularly solids and metallic system. However, LDA functionals tend to overestimate the de-locatization of electrons and severely fail in systems where electrons are highly localized, the description of which requires a more accurate description of exchange. This is related to the problem of self-interaction, which affects LDA functionals. In relation to the systems studied in this thesis, LDA is not able to describe the hydrogen bonds with the required accuracy. It is therefore necessary to use somewhat more sophisticated functionals.

The following level of complexity corresponds to the Generalized Gradient Approximation (GGA). In addition to the information about the local electronic density, these functionals also use information about the gradients of the density. For this reason, these functionals are frequently known as semi-local functionals, in contrast to the fully non-local description of exchange in the hybrid functionals (see below). GGAs do a better job at describing the non-

homogeneity of a realistic density distribution than LDA functionals. Furthermore, GGA functionals tend to have a somewhat improved description of exchange as compared to LDA functionals. Finally, some GGA functionals are known to provide a reasonably accurate of hydrogen bonds in many situations [IRE 04]. There are many popular GGA functionals (and, additionally, many of them have different variants). Two of the most widely used are the PBE, developed by Perdew, Burke and Ernzerhof [PER 96] [PER 97] and the BLYP, developed by A. D. Becke, [BEC 88] functionals. A better description of exchange can be achieved using the so-called hybrid functionals. These functionals, following the original proposal by A. D. Becke [BEC 93], combine non-local exact exchange from Hartree-Fock with a local GGA description of exchange using an empirical mixing parameter. Hybrid functionals improve the description of small molecules and system with localized electrons, which are very sensitive to the description of exchange and to the problem of self-interaction. Unfortunately, the hybrid functionals are less appropriate to describe systems with delocalized electrons. For example, hybrids tend to worsen the description of some metallic systems, e.g., simple metals, as compared to semi-local GGAs.

While semi-local GGA functionals provide a somewhat better description of exchange and local correlation effects than LDA, the effect of non-local correlations, like those that give rise to dispersion forces, is completely absent. These effects are also absent from hybrid functionals, since correlation effects in hybrids are usually described at the GGA or LDA level. However, van der Waals (vdW) forces are crucial to describe many systems like molecular crystals and hydrates systems similar to those described in this thesis [ROM 10]. For these reasons, there have been many efforts over the years to introduce vdW interactions in DFT calculations. The traditional approach has been to add empirical pairwise interaction potentials among atoms. The DFT-D method developed by S. Grimme and co-workers [GRI 10] is one of the most popular schemes following this approach. More recently, the so-called ab initio vdW corrected functionals have been developed after the work of Langreth, Lundqvist and co-workers [LAN 05]. These functionals do not include empirical parameters depending on the specific chemical species in the system, but rather they contain a term in the correlation energy exhibiting a fully non-local dependence on the electronic density. This term is the same for all system and only depends on the properties of the electronic density. The first successful

functional of this type was due to Dion et al. [DIO 04]. Following this original proposal several other ab initio corrected DFT-vdW approaches have been developed. This includes functionals like the one developed by Klimeš et al. [KIL 11] which that are claimed to be particularly adequate for solids and to describe the weak interactions at work in hydrates. In our simulations, we will compare the performance of some of the existing vdW functionals and will choose the one that provides the best description of the relaxed geometry of our system. Finally, it is worth noting that fully self-consistent calculations using vdW functionals became only practical thanks to the algorithm developed by Román-Pérez and Soler [ROM 09] that we will use in our simulations. This algorithm, using fast Fourier transforms and the convolution theorem to perform the six-dimensional integrals, makes the computational cost of ab initio vdW corrected DFT calculations comparable to those performed with plain semi-local GGAs.

(2) Basis set

To check the effect of the basis set on our simulations, we made calculations using basis of different types and sizes and check their ability to describe the equilibrium geometry of our target systems as one of the guides to select the most appropriate basis set. A critical parameter for the computational cost of the simulations is the size of the basis set, i.e., the number of localized basis functions used to describe the molecular orbitals. Furthermore, SIESTA uses a collection of strictly localized functions as a basis set. Thus, the efficiency and the accuracy of the calculations also depend crucially on the cut-off radius of the orbitals. Strongly localized functions are much more efficient in terms of computational time and memory usage. However, in order to describe systems like our hydrates, composed of molecules, we cannot use too tightly confined orbitals. Relatively extended orbitals are necessary instead to reach accurate results. In the following we describe some of the tests performed to choose the basis set used in our simulations. Some other tests and calculations are described in more detail in the results sections of this dissertation.

In this specific check, we focus on the N_2 hydrate in structure SI [MET 21]. We chose the N_2 hydrate because, before considering the additional complication of the acid hydrates (e.g.,

the extra protons in the water network), we need to make sure that we can represent adequately hydrogen bond network in the hydrate. The cell parameter (volume) and the general connectivity of the structure is a good guide to judge the quality of such a description.

We use the van der Waals corrected functional with the particular parametrization of the exchange- correlation developed by Dion *et al.* [DIO 04], labelled as DRSLL in SIESTA (vdW-DF in VASP). This functional is known to provide a sensible description of the hydrogen bonds and the hydrates systems (see, for example, [ROM 10]. As shown later in Chapter III, our checks performed in HPF_6 hydrates confirm that the DRSLL functional provides a good description of this type of systems.

The default basis set in SIESTA is the so-called double-zeta polarized (DZP) basis. This basis set contains two different radial functions (two different "zetas") to describe each valence shell occupied in the ground-state configuration of a particular atomic species. Additionally, it contains polarization orbitals, i.e., a shell of orbitals with an angular momentum higher than necessary to describe the atomic ground-state. For example, for oxygen the DZP basis contains 2 and 6 orbitals to describe the 2s and 2p shells, respectively, and a 3d polarization shell containing 5 orbitals. In total the DZP basis for oxygen has 13 orbitals and 5 orbitals for hydrogen. In our test, we have also considered the triple-zeta basis (TZP) that, for oxygen, contains respectively 3 and 9 orbitals for the 2s and 2p shells plus the 3d polarization shell, amounting to 17 orbitals in total (6 for hydrogen). Finally, we have considered the so-called double-zeta double-polarized (DZP2) basis, with 18 orbitals for oxygen and 8 orbitals for hydrogen. These basis sets were automatically generated using the algorithms in SIESTA, with a relatively large cut-off radius determined by an *Energy.Shift* parameter (see below) of 20 meV. We also performed tests with a DZP and a TZP specifically optimized for liquid water and ice by Corsetti and collaborators [COR 13]. For Nitrogen, we used a basis set optimized for molecular Nitrogen [SIMUNE].

Among other indicators, in our tests we have mainly focused on the equilibrium geometry and the cell parameters found for free cell-volume relaxations. In Chapter III we will also show that the combination of the chosen basis set and energy functional is able to satisfactorily reproduce the relative stability of different clathrate structures for the HPF_6 hydrate. The

relaxation of the cell disrupts the crystalline symmetry, which is not perfectly cubic any more. The obtained cell parameters, as well as its mean value, are given in Table II. 1.

Table II. 1. Simulation with DRSLL functional and different basis set.

Basis size used with DRSLL functional	Mean Cell parameter (Å)	a (Å)	b (Å)	c (Å)
DZP-set optimised	~ 12.03	12.023	12.025	12.050
DZP2- set auto-generated	~ 11.9	11.939	11.898	11.899
TZP-set optimized	~ 12.1	12.102	12.109	12.103

The hydrate N_2 in structure SI has a cell parameter of 12.1 Å [MET 21]. The DZP and TZP basis size optimized for Oxygen, Hydrogen and Nitrogen gave the most accurate relaxed cell volume comparing to experimental data in literature. The TZP basis having a larger number of orbitals per atoms, the simulation takes substantially longer than with the DZP basis size. However, analyzing the structure, we find that the improvement in the description does not justify the extra computational costa as compared to the TZP basis. Thus, after these tests and also taking into account the additional tests and calculations shown in Chapter III, we decided to use the optimized DZP basis [COR 13] for the rest of this work.

(3) Others parameters

There are other several parameters that determine the quality of the SIESTA simulations and we will discuss some of them in the following. All the simulation parameters are chosen taking into account the balance between accuracy and cost.

In general, a good calculation will need a sufficiently large number of k–points, a low Electronic Temperature (since we are aiming at representing the ground-state and a low temperature experimental situation), a small *SCF.H.Tolerance* parameter, determining the self-consistent solution has been reached, and a high enough value of the *Mesh.Cutoff* (see below). These options need to be carefully tested and the used values will depend on the studied system.

The *Mesh.Cutoff* is an important parameter in SIESTA. In addition to a basis set of numerical atomic orbitals of finite support, SIESTA uses a 3D grid of points in real space to for the calculation of some integrals, the representation of charge densities and the calculation of the exchange-correlation potential and some components of the Hartree potential. Its fineness is determined by its plane-wave cutoff (*Mesh.Cutoff*), meaning that only plane-waves with kinetic energies lower than this cutoff can be represented in the grid without aliasing. In turn, this implies that if a function (e.g., the electron density or the effective potential) can be faithfully represented using plane-waves within such cutoff energy, then it can be Fourier transformed back and forth to such grid without any loss of information. The existence of a real-space grid breaks translational invariance, given rise to small ripples in the calculated energy. In the SIESTA community, this is usually known as the egg-box effect, and it is an indication that the density and potential do have plane wave components above the mesh cutoff. This symmetry break manifest most clearly when moving one single atom in an otherwise empty simulation cell. The total energy and the forces oscillate with the grid periodicity when the atom is moved, as if the atom were moving on an eggbox. In the limit of a very fine grid this effect becomes negligible and eventually disappears. For reasonable values of the mesh cutoff, the effect of the eggbox on the total energy, forces and the relaxed structure is very small. However, it can affect substantially the process of relaxation, by increasing the number of steps considerably, and can also spoil the calculation of vibrations, usually much more demanding than relaxations. In our case, depending on the specific simulation to be performed, the *Mesch.Cutoff* is set at values between 200 Ry and 300 Ry. The specific value will be specified in each case.

The *Energy.Shift* is another important parameter that serves to determine the confinement radii of the atomic orbitals in SIESTA. It is interesting to recall here that SIESTA uses pseudopotentials and, thus, core electrons are replaced by an effective potential between the core and the valence electrons known as pseudopotentials. The pseudopotentials used in this work are either computed by us or obtained from the literature and open-source repositories. In all cases, these pseudopotentials are thoroughly tested. In SIESTA, the main shell (first zeta) of the numerical atomic orbitals for a given atomic species is obtained finding the solutions of the screened atomic pseudopotential. This so-called Pseudo-Atomic Orbitals (PAOs) are not

computed at the energies of the atomic eigenvalues, but at slightly higher energies. This excess energy is called the "Energy Shift" and corresponds to the parameter discussed here. As a result, the found solutions do not go to zero smoothly at infinity but rather get to at a finite distance from the nucleus that determines the confinement radius of the orbital. This allows defining the cutoff radii of all the orbitals in all the atomic species using a single parameter and in a balanced way [ART 99]. Standard values for the *Energy.Shift* parameter run from 200-100 meV to a few tens of meV. In the present case, as mentioned above, we are dealing with a system composed of molecules and, therefore, it is important to have orbitals that decay smoothly into vacuum. For this reason, in our case we use a value of 20 meV for the *Energy.Shift* parameter.

The Siesta parameter called *Max.Force.Tolerance* is the maximum residual value of the force accepted in a coordinate optimization to consider the structure as relaxed. The calculation stops if all the component of the force in the system is smaller than the *Max.Force.Tolerance* that we set at 0.01 eV/Ang. Structural relaxations can be performed in SIESTA using different methods. In our simulations we used the Conjugate Gradient algorithm, with an adequate preconditioning for cell relaxations [PRE 07].

The fineness of the k-point sampling of the Brillouin zone is selected using the *kgrid.MonkhorstPack* data block. In our case, the utilized cells are sufficiently large that it is possible to use only the Gamma point for sampling. This has been proven with extensive tests. Furthermore, giving the localized character of the molecular orbitals in our systems, it is expected that they will not be very sensitive to the k-point sampling.

ii. Structural model

To perform our simulations, we need an initial guess for the coordinates of the atoms in the hydrate crystalline structure. Fortunately, the crystalline structure of the hydrates studied in this work is well-known. The oxygen positions in the different structures were already determined by X-ray diffraction [SLO 08]. The position of the hydrogens, however, are not directly accessible to the experiment. The hydrogen atoms in the hydrate network need to

respect the ice rules, i.e., each water molecule accepts and donates two hydrogen bonds. Still there are many possible configurations consistent with the structures of the clathrates and the ice rules. Here we have used structures from previous works, relaxed with VASP simulations, for the HPF_6 hydrate in structure SVII [BED 14] and various gas hydrates in structure SI and SII (like CO_2, CH_4 and N_2) [MET 21]. We always considered bulk structures, meaning that we always considered crystalline periodic structure using periodic boundary conditions. We did not study the surface of the hydrates in our simulations.

The unit cell of the structure SVII is formed of two cages (cages type: $4^6\,6^8$, see Chapter I). For the HPF_6 systems, the simulation box contains 8 unit-cells (16 cages in total). This supercell was created by duplicating the unit-cell in all three periodic directions (see Figure II. 11). We choice of such large supercell is required to have realistic concentration of dopants in our simulations of the doped hydrates. We have a ratio of 1 impurity for 15 HPF_6 molecules, which is in the experimentally observed range. For convenience, the impurity is typically located close to the center of the simulation box.

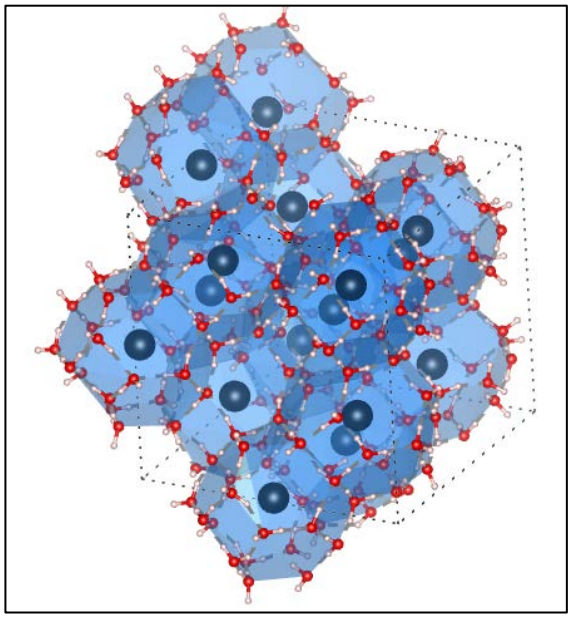

Figure II. 11. Simulation box with 8 unit-cells of HPF_6 hydrate.

The THF and $HClO_4$ hydrates exhibit the SII and SI structures [SOL 08, MET 21]. The guests are

usually placed at the centre of the simulation box. The structure SII with THF and $HClO_4$ guest are presented in Figure II. 12

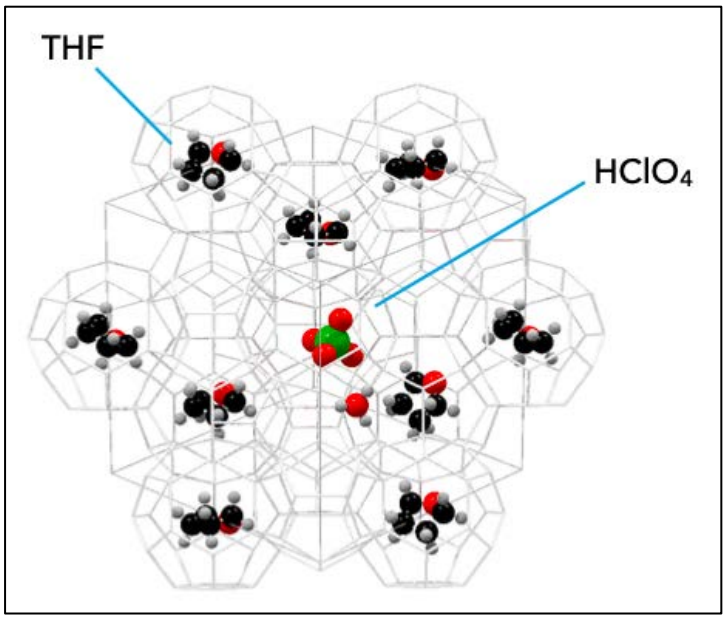

Figure II. 12. Simulation box with 1 unit cell of hydrate THF-$HClO_4$ in structure SII.

iii. Dealing with the excess proton

The acid hydrates present extra protons participating in the water network. The hydrate host structure now has H_2O molecules and H_3O^+ species. The presence of H_3O^+ species disrupts the hydrogen bond network of the clathrate structure, which is governed by the so-called ice rules. Thus, adjustments are necessary.

The number of H_3O^+ depends on the number of acid molecules and their charges (X^-, X^{2-}, …). The mobility of the extra protons makes it difficult to find their exact, energy minimal, equilibrium positions. The protons move according to the Grotthus mechanism [KRE 82]: jumping from nearby oxygens along the hydrogen bond (presented in Chapter I). In previous simulations [BED 14], a thermal treatment was applied to solve this problem and find a favourable relaxed structure. The hydrate structure for the acid is built from a standard hydrate structure, the oxygen positions are fixed and then, the necessary extra protons are added in "reasonable" positions in the cages. A high temperature molecular dynamics simulation is then performed while keeping the positions of the oxygen atoms fixed. Once the

system has thermalized, the temperature is slowly reduced until we finally reach a stable structure at low temperatures. This structure is further relaxed at zero temperature. This simulation allows all the protons to have enough energy to move in the calculation box and find their place, respecting the ice rules as much as possible. [BED 14]. The structure found with this technique was used as a starting point, in this work, for the HPF_6 and $HClO_4$ acid hydrates. For the simulations with the THF hydrate structure (exhibiting the SII structure), there is no extra proton in the structure except when we replace THF molecules by $HClO_4$. However, at most, we replace one THF by one $HClO_4$ by unit cell (see Figure II. 13). Thus, in the simulation box of one unit cell, we will only have one extra proton. Due to the mobility of the protons and the small amount of the protons, the protons are placed by hand in appropriate locations in the cages sub-structure surrounding the acid molecules. A subsequent relaxation brings the proton to a stable position in the hydrogen-bond network without further difficulties.

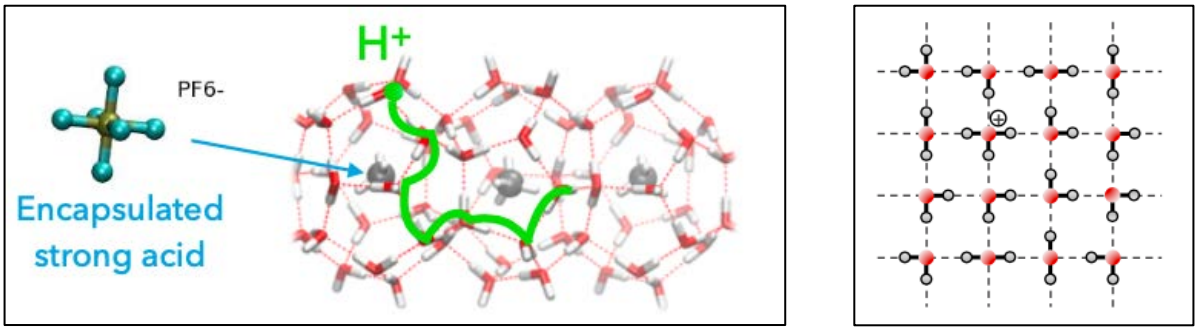

Figure II. 13. Left. Hexafluophosphoric acid hydrate in structure VII. Right. Position of the extra proton in the hydrate water network from the encapsulation of anion species.

Electronic structure methods working with periodic boundary conditions have problems to deal with charged systems. In principle, the only way to deal with a periodic system is to enforce its neutrality. In the case of the SIESTA method, and many other periodic methods, an homogeneous neutralizing background of charge is added to the simulation box to ensure its neutrality. Although the full hydrate structure is always neutral, we will need to consider charged situations in our analysis as we will see below.

3. Simulation Output.

i. Cell parameter relaxation

The relaxed cell parameter corresponds to the lowest relaxed energy. Its value is best determined in a set of sequential calculations for different cell parameters. We start the relaxation process using a reasonable value (e.g., close to the experimental observation) for the hydrate cell parameter and constructed the simulation box. The atomic coordinates of the atoms in the structure are then relaxed for this initial cell parameter. Then, the cell volume is changed in small steps, with the atomic structure being fully relaxed in each step. We change the cell parameter step by step in a range of approximately a 10 % of its initial value, calculating the relaxed energy at each point. It is important that the cell volume is changed by small amounts. Otherwise, we face the risk of severely distorting the structure and, thus, finding discontinuities in our computed relaxed energy. This step-by-step process gives the relaxed energy as a function of the cell parameter, see Figure II. 14. A minimum of the energy is observed. The data are fitted using the Birch−Murnaghan equation of state, which is a relationship between the volume of a body and the pressure to which it is subjected,

$$E(V) - E_0 = \frac{9V_0B_T}{16}\left\{\left[\left(\frac{V_0}{V}\right)^{2/3} - 1\right]^3 B'_T + \left[\left(\frac{V_0}{V}\right)^{2/3} - 1\right]^2 \left[6 - 4\left(\frac{V_0}{V}\right)^{2/3}\right]\right\} \qquad (II.40)$$

where E_0correspond to the minimal energy associated to the volume V_0, B_T is the elasticity module and B'_T is the derivate of the elasticity module in relation with the pressure.

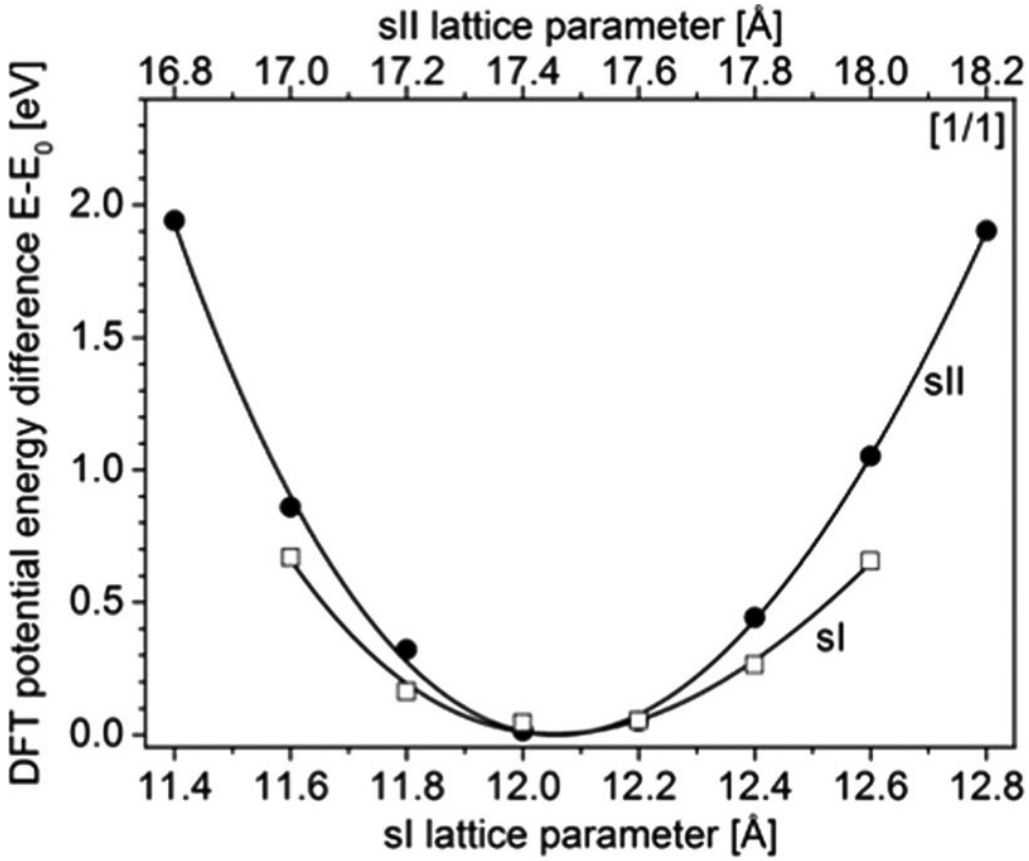

Figure II. 14. Example of cell relaxation method. DFT potential energy difference E − E0, as a function of the lattice parameter from DFT calculations obtained using VASP with the vdW-DF functional for both sI (empty squares) and sII (filled circles) structures. Continuous lines represent the fitted curves using the Birch–Murnaghan EOS [MET 21].

ii. Estimation of the stability of the different impurities in the hydrate

The energies of systems containing different number of atoms and chemical species cannot be directly compared to determine the relative stability. In our case, we study hydrates containing different guest molecules and we want obtain a measure of the relative stability of the different dopant molecules inside the hydrate.

To compare the stabilization energy of the different systems, we perform two types of calculations. First, a system with a single anion ***(A)***: E_{anion} with anion = PF_6^-, $H_2PO_4^-$, HPO_3F^- or $PO_2F_2^-$, which gives the energy of the free anion outside the water cage. It is important to use a very large unit cell in this first calculation to minimize any possible spurious effects due to

the neutralizing charge in the simulation box. We have carefully checked the convergence of E_{anion} with the size of the simulation box. Second, we considered hydrate systems containing 2 by 2 by 2 unit cells (see Figure II. 11): ***(B)*** A hydrate with all cages filled with PF_6^- that we label E_{hyd} in the following; ***(C)*** A hydrate similar to (**B**) but containing 1 anionic impurity replacing one PF_6^- in the supercell that we label E_{hyd_imp}.

In order to estimate the different of the binding energy of the different anions we now define these two quantities (which do not have a simple interpretation):

$$E_{hyd_B} = E_{hyd} - E_{PF6} \qquad (II.41)$$

$$E_{hyd_C} = E_{hyd_{imp}} - E_{impurity}\,. \qquad (II.42)$$

Here $E_{impurity}$ is the energy of one molecule of $H_2PO_4^-$, HPO_3F^- or $PO_2F_2^-$ depending on the impurity used to replace one of the PF_6^- in the hydrate.

We can now estimate the difference of stabilization energies of the different dopants, relative to the binding energy of a PF_6^- anion in the pure HPF_6 hydrate, taking the difference

$$E_{diff} = \mathrm{E}_{hyd_C} - \mathrm{E}_{hyd_B} \qquad (II.43)$$

Thus, this energy difference serves as an indicator of the relative stability of the structure depending on the guest trapped inside the hydrate cages.

A similar method to compare the energy is applied for the mixed hydrate of THF and $HClO_4$.

The simulation results are presented in Chapter III for the hydrate of HPF_6 and in Chapter IV for the mixed hydrate of THF and $HClO_4$.

Chapter III. Simulation of the HPF6 hydrate

Table of content

A. Optimised simulation parameters for Hydrate Structure

Clathrate hydrates are nanoporous ice-like structures where H_2O molecules form cages with trapped guest molecules [SUM 09]. In the case of strong acid guest molecules, one generates a super-protonic conductor due to the delocalization of acidic protons within the cage sub-structure (see Chapter I). These systems constitute an interesting opportunity as new electrolytes for fuel cells. Among the strong acid hydrates, the largest conductivity is known for HPF_6 hydrates [CHA 08, DES 18]. The HPF_6 hydrate grows in the well-known SI structure as well as in the SVII structure, both shown in Figure III. 1, depending on the hydration number and the temperature [MOO 87].

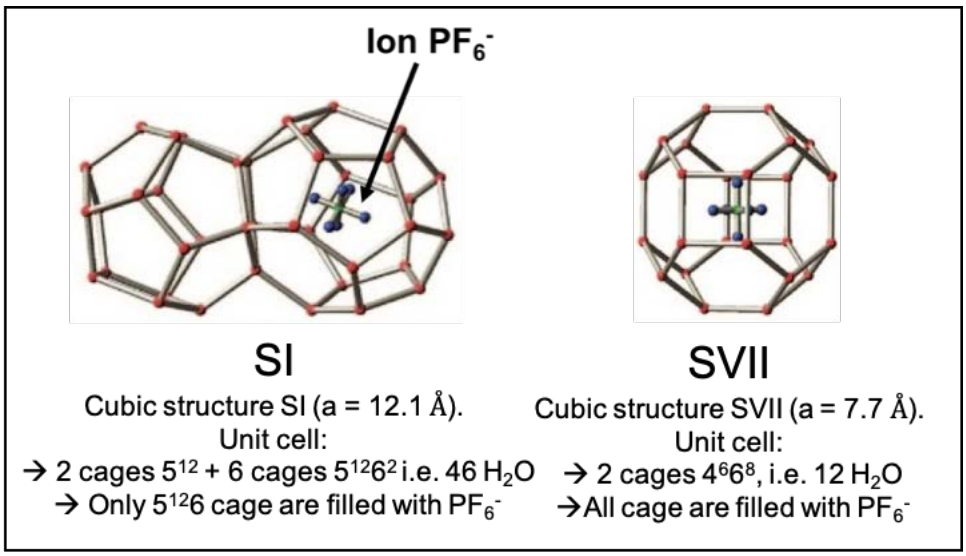

Figure III. 1 HPF_6 hydrates in SI and SVII crystalline structure

From Raman spectroscopy experiments done in a previous PhD project in the group of Prof. A. Desmedt [DES 18], evidence of the presence of impurities such as H_3PO_4, H_2PO_3F, HPO_2F_2 in those hydrate samples was found. These impurities are the product of the high reactivity of HPF_6 with water. They were expected to strongly influence the properties of the hydrate samples. Thus, it is important to study the localization of the impurities in the sample, determining if they occupied positions inside or outside the cages.

To answer this question on the localization of the guest impurities in the HPF_6 hydrate, we

used first-principles DFT calculations to study the stability of different impurities inside the structures. The calculations were performed using SIESTA program. SIESTA is both a method and its computer program implementation to perform efficient electronic structure calculations. As discussed in Chapter II, SIESTA uses a basis set of strictly-localized atomic orbitals that allows tuning the accuracy and the cost of the simulations in a wide range. This methodology, which is freely distributed under a GPL open-source license, has opened the possibility of carrying out first-principles electronic structure calculations for large systems with relatively modest computational resources, and it is currently used by many research groups worldwide [SOL 02]. The trade-off between accuracy and computational cost highlights the importance of using the right computational parameters and optimizing them for the systems of interest. In particular, for acid hydrates, the hydrogen bonds in the hydrate cages and the ionic interactions associated with the guest molecules need to be addressed carefully. In the following (as well as in Chapter II), we present information about how the computational parameters have been optimized using results from the literature for the HPF_6-nH_2O ionic clathrate hydrate as a benchmark. Once the optimal computational parameters have been determined, we will use them to study the relative stability of different impurities in the HPF_6 hydrate.

1. Choice of DFT Functional

i. A short review of the existing literature

Density functional theory (DFT) is known to be a good simulation method have been claimed to be appropriate for studying molecular crystals [BUR 12]. The interactions at work in typical hydrate structures are mostly host-host interactions between water molecules via H-bonds and guest-host interactions between the trapped molecules and the water cage due to van der Waals dispersion forces. To describe these interactions correctly, the choice of the DFT functional is essential.

The generalized gradient Approximation (GGA) uses information about the local electronic

density and their local gradient, which allow a better description of the non-homogeneity of the real density than the LDA functionals. For this reason, all the functional tests are chosen inside the GGA family of functionals.

Although all functionals present some shortcomings for the hydrate systems, some systematic studies have been performed, and some functionals that performed well for these systems have been found [COX 14, GIL 16]. For example, PBE-GGA functional [PER 96] is widely used for its accuracy in describing the hydrogen bonds between the water molecules forming the cages. Due to the dispersive forces, the guest-host interaction requires the inclusion of the vdW interactions. In this regard, it has been shown that ab initio vdW corrected functionals performed reasonably well [COX 14, ROM 10], although they tend to over-stabilize the hydrate structure [GIL 16].

Several previous studies focused on the structural stability of gas hydrate. Different functional were tested to determine the equilibrium unit-cell volume. One of these studies [VAL 16] showed that the experimental cell parameter is best reproduced by revPBE functional (revised Perdew-Burke-Ernzerhof). In a second study performed on SI and SII gas hydrate structures [PET 19], the functional PBE [PER 96] and vdW-DF [DIO 04] were used to test the effect of the dispersion forces on the hydrate structure stability. The optimised cell parameters were compared to that found by neutron diffraction, and a good agreement was found between the theoretical and experimental results, confirming that PBE and vdW-DF (labelled in the following DRSLL, according to the nomenclature used in the SIESTA package) provide good results for the structural properties of standard hydrates.

However, more information is needed on ionic hydrates. In addition to the “normal” hydrate interactions, ionic interactions between the anion guest and the host structure must be addressed. The presence of the charged guest, and the corresponding acidic proton, creates a defect in the hydrate sub-structure. The extra protons participate in the cages of the host structure, forming hydronium molecules H_3O^+. While in standard hydrate structures, the oxygen atoms forming the cages have 4 hydrogen sites, each with ½ occupation probability, the extra protons add a local charge and break the structure organised according to so-called ice rules.

In our test for the HPF_6 hydrate, we have tested three different functionals:

- PBE, a semi-local (GGA) functional by Perdew, Burke and Ernzerholf [PER 97]. Probably the most widely used functional to study crystalline solids and condensed matter systems.
- DRSLL, an ab-initio van der Waals-corrected density functional by Dion *et al.* [DIO 04] with the efficient implementation of [ROM 09)]
- BH, a van der Waals density functional similar to DRSLL but with a modified description of exchange as described in Ref. [BER 14].

We mostly focus on vdW-corrected functionals because they have already been identified in the literature as accurate in describing water systems. Since the hydrate structure is mainly determined by hydrogen bonding, these functionals can be expected to provide a reasonable description of hydrates. Furthermore, vdW functionals can describe dispersion forces that are important in the interaction of the guest molecules with the water cages. For acid hydrates, however, it is also crucial to describe accurately the anionic guest and the associated ionic interactions. The accurate description of the anions might be a challenge for vdW functionals based on a GGA-like (semi-local) exchange. For this reason, we have considered two functionals with different descriptions of exchange. As a guide to determine the most suited vdW functional for our acid hydrates, simulations were made to obtain the equilibrium volume of the cell and later compare it to the experimental data.

ii. Test of the functionals for the hydrate structures

Next, we studied the HPF_6 hydrate in structure SVII to test the performance of different functionals on acid hydrate systems. The hydrate structure is taken from the work of Bedouret *et al.* [BED 13], where the simulation unit cell is constructed from the spatial positions of the oxygen atoms and guest molecules extracted from X-Rays diffraction experiments [BOD 55]. The optimized hydrogen and fluorine positions were found after molecular dynamic simulation with a velocity scale thermostat that allowed the motion of atoms to their most

stable positions while preserving the integrity of the hydrate structure by fixing the oxygen and phosphor [BED 13]. This procedure was briefly explained in Chapter II. The system studied is a supercell constituted of 8 unit-cell in periodic conditions of the SVII hydrate structure corresponding to 16 cages ($4^6 6^8$), as represented in Chapter II. The nominal cell parameter of this supercell is 15.4 Å, corresponding to 2 times a, with a=7.7 Å the experimental cell parameter of the structure SVII unit-cell.

The cell parameter is a fundamental parameter describing the structural integrity of the hydrate. Looking at the cell volume resulting from the relaxation calculations will confirm that our simulations are able to describe the system correctly. We performed full structural relaxation that include the relaxations of the cell parameters. The obtained equilibrium cell parameters will be used to select, among the three functionals mentioned above, the functional that describes most accurately the HPF_6 hydrate.

The relaxation calculations are made with the basis set the optimized double-zeta polarized (optimized DZP, see Chapter II Method). The relaxed cell parameters are presented in Table III. 1. The considerable variations confirm the different description of the system by different functionals.

Functional	**Relax Cell volume parameter** (Å)			**Mean Cell Parameter** (Å)
PBE	15.750	15.875	15.543	15.723
DRSLL	16.013	16.197	15.752	15.987
BH	15.526	15.626	15.256	15.469

Table III. 1. Cell parameter of the super-cell HPF_6 hydrate in structure SVII with different functional.

From these simulations, we can conclude that the BH van der Waals functional, with an average cell parameter of 15.469 Å, gives the closest cell parameter to experimental value of 15.4 Å. Therefore, in the following we will use the BH functional to study the relative stability of dopant molecules on the HPF_6 hydrate.

2. Relaxed structure of the HPF_6 hydrate with the BH functional.

Before considering the structural stability of the HPF_6 hydrate with impurities, we consider in more detail the stable geometric structure obtained with the BH functional. Furthermore, we will also check the adequacy of other simulations simulation parameters. Here, the relaxation is performed keeping the cubic symmetry of the hydrate structure and changing the lattice parameter in steps of 0.1 Å (~1%). We start at 15.4 Å, we find the relaxed structure, record the corresponding energy and then change the cell parameter to 15.5 Å (in doing so we re-scale all the atomic coordinates). The procedure is repeated several times, also contracting the lattice parameter, so we can trace the energy of the relaxed structure as a function of the cell volume (see Figure A2 below). We must change the lattice parameter in little steps to avoid the distortion of the hydrate structure, which could lead to a spurious energy minimum and the wrong relaxed coordinates.

The simulations are performed with the BH functional, an optimized DZP basis set and a *MeshCutoff* set to a nominal value of 200 Ry. The *MeshCutoff* defines the fineness of the real-space grid in SIESTA by specifying the energy cutoff of the plane-waves that can be exactly represented in such grid. The *MeshCutoff* parameter in the SIESTA input in fact only defines a minimum value for the plane-wave cutoff. The variation of the simulation box size can give rise to an effective change of the "actual" mesh cutoff as we change the lattice parameter, since the grid can only accommodate an integer number of points compatible with the Fast Fourier Transform algorithms used in SIESTA. This can potentially lead to discontinuities in the energy versus lattice parameter curve. Therefore, it is instrumental to use a large enough *MeshCutoff* value to avoid noticeable jumps in the energy.

Figure III. 2 shows the relaxed energy for a perfectly cubic unit cell as a function of the cell parameter. The curve is fitted with a Birch-Murnaghan equation (see Chapter II - Methods). The corresponding minimum energy is found for a cell parameter equal to 15.47 Å, identical to the average lattice parameter that we found previously in full relaxations, including the parameters defining the cell shape and volume.

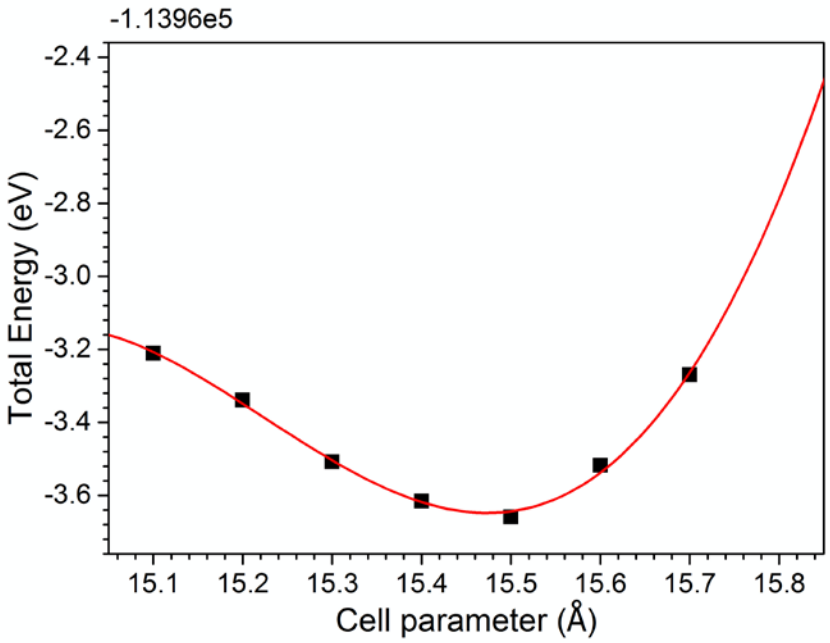

Figure III. 2. Cell parameter relaxation and fitting curve by Birch-Murnaghan [BIR 47].

B. Substitution of HPF_6 by Impurities

1. Systems

To complete the experimental finding [DES 18] and provide answers to the localization of the impurities in the PF_6^- hydrate system and their influence on the electrostatic interactions in the hydrate, we use here DFT calculations of the doped system.

The interactions involved in the clathrate hydrate are interactions between water molecules through hydrogen bonding (host−host interactions) and between the host cages and the guest molecule through possibly hydrogen bonding and van der Waals interactions (guest−host interactions). When an acid is included in a cage, an ionic bonding could occur between a hydronium ion present in the aqueous substructure and the anion. These interactions are, therefore, sensitive to the particular anionic species (depending on its size, geometry, charge,

etc.)

We fixed the cell parameter to the experimental value of 15.4 Å (2x7.7Å unit cell), which as shown above, is very close to the calculated equilibrium result. Because of the large size of the cell, all calculations were performed using only Gamma point k-sampling. Relaxations were performed with a threshold force of 0.01 eV/Å as a criterium for convergence.

Similar to the previous section, we used a double-zeta polarised basis for Oxygen and Hydrogen optimized for water systems [COR 13], while we used a similar optimized DZP basis set for Phosphor and Fluor as given by the SIMUNE group [SIMUNE] As discussed above, van der Waals-corrected BH functional [BER 14] was used.

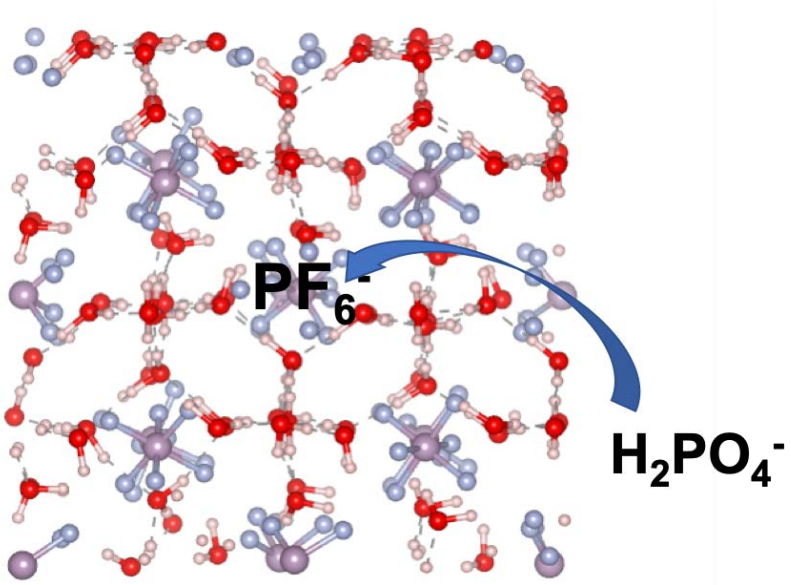

Figure III. 3. Simulation box (composed of 8 unit-cells) of HPF_6 hydrate in structure S VII, with all cages full with PF_6^- guest anions except for one cage, which can either have a PF_6^- or an impurity guest like $H_2PO_4^-$.

The simulation strategy then proceeds as described previously in Chapter II. We perform calculations for the pure HPF_6 hydrate and for a doped hydrate with a 6.3 % concentration of impurities, corresponding to a 1 to 15 ratio for impurity versus PF_6^- anions (see Figure III. 3). We also need to compute the energies of the isolated anions in a vacuum as a reference energy to compare the relative stability of the different species inside the hydrate. This last

calculation requires considering explicitly negatively charged systems, which requires the use of neutralization background of charge (see Chapter II) and the use of sufficiently large cells to converge the value of the total energy of the anion.

2. Relative stability of acid dopants in the SVII HPF6 hydrate

To determine whether the different acid impurities are likely to substitute PF_6^- anions inside the cages we performed simulations $H_2PO_4^-$, HPO_3F^- or $PO_2F_2^-$. The structure of the corresponding systems and a sketch of the procedure is presented in Figure III. 4.

As explained in detail in Chapter II, with our calculations, we estimate the relative stabilization energies of the different anionic species inside the hydrate structure with respect to their energy in a vacuum (as isolated anions). This parameter that we simply call E_{diff} estimates for the different anionic species the relative binding energy of one anion to the hydrate (with all the other cages full with PF_6^- molecules). The binding energy of the PF_6^- anion is used as a reference.

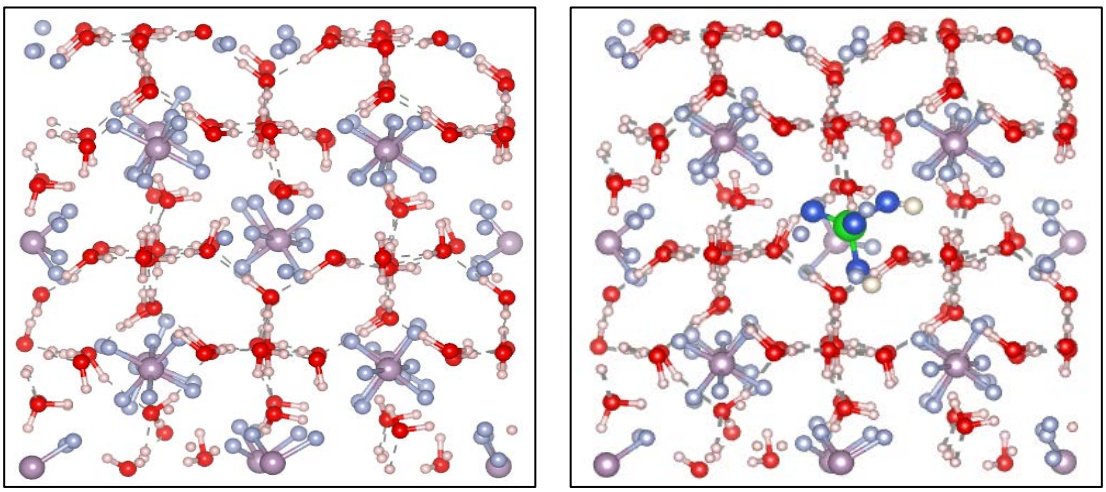

Figure III. 4. Super cell of the HPF6 hydrate in structure SVII. Left: all cages full with PF6-. Right: one PF6- replaced by a H2PO4- impurity.

The results for the energy difference E_{diff} are shown in Figure III. 5.

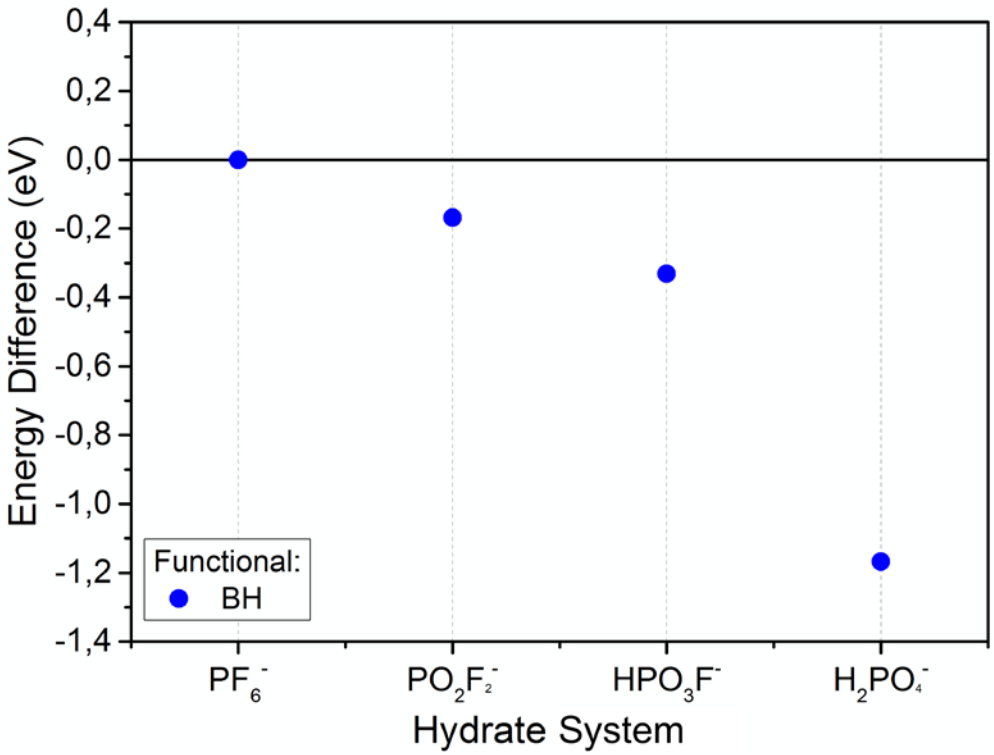

Figure III. 5. Relative stabilization energy (E_{diff}) for several anionic species inside the HPF_6 hydrate in structure SVII. Data computed for 6.25 % concentration of impurities using an optimized DZP basis set and the van der Waals-corrected BH functional [BER14].

The simulations show that $H_2PO_4^-$ is the impurity that has the largest affinity towards the HPF_6 hydrate in structure S VII. In general, all the considered species show a larger binding energy to the (full) hydrate structure than PF_6^-, indicating that, in principle, the substitution of PF_6^- anions by $H_2PO_4^-$, HPO_3F^- or $PO_2F_2^-$ is always a favourable process, at least for the concentration consider here. In other words, our theoretical results indicate that these impurities, if present in the sample, are likely to appear in small quantities inside the cages of the SVII HPF_6 hydrate.

3. Comparison with experimental observations.

Experimentally, depending on the hydration number *n* and the temperature, HPF_6-*n*H_2O

samples exhibit structures SI and SVII [CHA 08]. A structural transition takes place from the SI to SVII when increasing the temperature for samples with a hydration number higher than 6 [CHA 08].

Desplanche *et al.* [DES 18] performed NMR experiments on HPF_6 hydrates in order to study their formation process and the possible presence of impurities. Detection of fluorine and phosphorus in NMR studies allowed probing the composition of the HPF_6-$n H_2O$ samples and thus monitoring the influence of the hydration number on the structure. These studies also allowed concluding that, besides PF_6^-, other acid species like H_3PO_4, $H_2PO_2F_2$, H_3PO_3F and HF were also present in the samples. For temperatures between 230 K and 270 K, when all samples (HPF_6-$n H_2O$) adopted the SVII structure, the largest number of impurities was observed for a hydration number n = 7.67. Qualitatively, the concentration of impurities was observed to increase with the hydration number.

Part of the impurities was localized by Nuclear Magnetic Resonance to be in a liquid state. The NMR spectra of the clathrate HPF_6-7.67H_2O have shown that the line widths associated with the chemical species called impurities are close to those observed for an acid solution. The other part of the impurities present in the samples, in opposition to the liquid ones, seems to be in a solid state. This observation corroborates the results of Raman spectroscopy studies by Desplanche *et al.* [DES 18]. Raman spectroscopy revealed the presence of a new molecular environment for PF_6^- (different from that observed when it is part of the clathrate structure), corresponding to the liquid phase detected by NMR, and also the presence of characteristic bands of the H_3PO_4 species for n > 6 clathrates adopting the SVII structure (T > 230 K).

Therefore, the experimental information points towards the affinity of acid impurities present in the initial solution to occupy, at least partially, positions inside the cages of the SVII HPF_6 hydrate, substituting some of the PF_6^- anions. The DFT simulations presented here seem to support this interpretation of the experimental findings. The total energy calculations show the stabilizing effect of the presence of low concentrations of $H_2PO_4^-$, $HPO_2F_2^-$ and $H_2PO_3F^-$ impurities inside the cages of the HPF_6 hydrate in SVII structure.

C. Conclusion

To complement previous experimental findings and get insight into the location of acid impurities in the HPF_6 hydrate system, we have performed theoretical calculations using density functional theory.

Describing the hydrate system by DFT brings several challenges. It is necessary to accurately describe the interaction of the water molecules in the hydrate structure and the interaction between the water cage and the trapped guest molecules, as well as the distribution of charge associated with the presence of anions and the neutralizing protons.

Here, we first discussed the choice of the density functional and other simulation parameters within the SIESTA method to compute the properties of the HPF_6 hydrate in structure S VII. We then studied the relative stability of different acid species as substitutional impurities of PF_6^- at low concentrations. We found that at ~6.3 % concentration of $H_2PO_4^-$, $HPO_2F_2^-$ or $H_2PO_3F^-$ impurities stabilize the SVII structure with respect to the pure HPF_6 hydrate. In other words, if present in the initial solution, these impurities will tend to replace some of the PF_6^- inside the cages. The concentration of the impurities is likely to be an important factor in the question of the stability of the hydrate structure. In this study, we have only considered one concentration within the experimentally observed range. This issue must be considered more carefully in future work.

In summary, using information from line widths and chemical shifts of the NMR experiments [DES 18] and from the DFT stability calculations performed in this work, we can conclude that the insertion of acid impurities like $H_2PO_4^-$, $HPO_2F_2^-$ or $H_2PO_3F^-$ within the clathrate structure in the case of the HPF_6-$6H_2O$ hydrate in structure SVII.

Chapter IV. Structural study of the mixed hydrate of THF-HClO4

Table des matières

A. Introduction

In the case of protonic conductor materials like Nafion, hydration is of primary importance since the water molecules are responsible for transporting the protons throughout the material [KER 82]. For hydrate compounds, the trapped acid is responsible for the charge displacement and the proton excess leading to the protonic conductivity [MOO 87, WIE 87]. As explained in Chapter I, knowing the conductivity mechanism in hydrate raises the question of the influence of the acid concentrations beyond its nature and the impact of the hydrate structure.

To address the acid concentration effect on the conductivity, we turn ourselves to mixed hydrate compounds. Mixed hydrates have a structure co-including several molecules. Here, we study the mixed hydrate of Tetrahydrofuran THF and perchloric acid $HClO_4$ with various fractions to tune the acid concentration in the formed hydrate.

The mixed hydrates will be investigated by X-ray diffraction. We studied the temperature stability of the various structures and the relative fraction of the structures within the sample for various acid fractions. Finally, the use of quantum simulations at the level of the Density Functional Theory approximation (DFT) is discussed to address issues regarding the cage filling and the guest position within the hydrate sub-structure when the co-inclusion of guests is considered.

B. Influence of the acid concentration on the hydrate structure in mixed hydrate

1. Hydrate structure identification

As shown in Chapter I, hydrate structure depends strongly on the encapsulated guest. With

two types of guests, the fraction of each guest will determine the structure formed.

The part of the structure of the mixed hydrate THF-$HClO_4$ has already been studied for low acid fractions in the work of Desmedt e*t al.* [DES 15]. In this paper, the SII hydrate structure is formed by mixing tetrahydrofuran (THF) and perchloric acid ($HClO_4$) guest molecules. The formation of the mixed hydrate requires the cooling of a $(1-\alpha)\mathrm{THF}\cdot\alpha\mathrm{HClO}_4\cdot 17H_2\mathrm{O}$ solution with α less than 0.125. Above this concentration, different phases were observed: a mixture of SI and SII. Focusing on the SII structure, they demonstrated that the substitution of a THF molecule per a perchlorate anion allows the modification of the melting of the SII hydrate by preserving the structure [DES 15]. It reveals the key role played by acidic defects existing in the host substructure on the physicochemical properties of clathrate hydrate.

In the mixed hydrate samples, various crystalline structures are expected. The SII and SI hydrate structure depending on the acid fraction in the samples but also hexagonal ice.

Tetrahydrofuran (THF) hydrate forms the SII structure at atmospheric pressure with a melting temperature of 277.4 K with cubic cell parameter a = 17.2 Å [CON 09, MAK 05, PRAS 07]. The pure hydrate reference pattern is taken from hydrate molecular formula THF-$17H_2O$.

The perchloric acid ($HClO_4$) hydrate, which chemical formula is $HClO_4$-5,5 H_2O, form SI structure at atmospheric pressure with a melting temperature of 228 K with cubic cell parameter a= 12.1 Å [MOO 87]. The hydrate structure for other hydration numbers for samples $HClO_4$-*n*H_2O has yet to be determined regarding hydrate/Ice ratio or cage filling. The stability of the solid phase of $HClO_4$-*n*H_2O is given in Figure IV. 1[BRI 49].

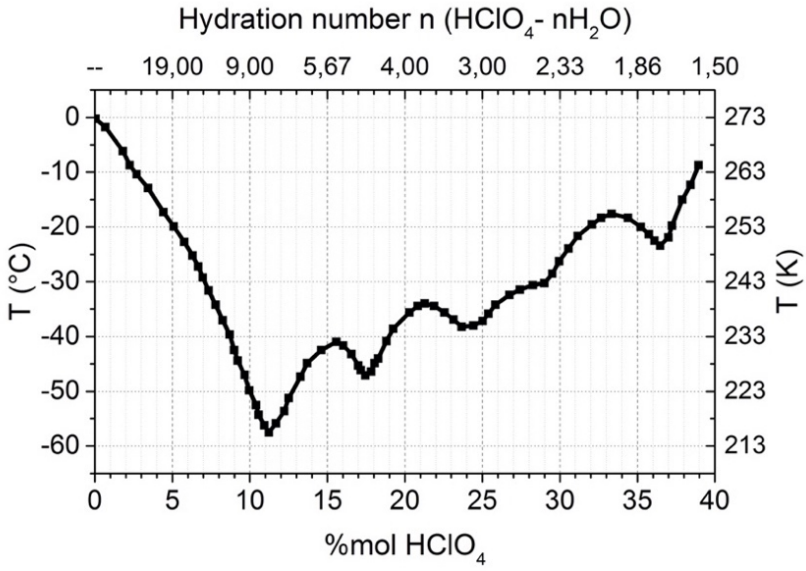

Figure IV. 1. Temperature stability of $HClO_4$-nH_2O depending on the molar concentration of $HClO_4$ (%mol) and the hydration number n [BRI 49].

From the simulated pattern, we can identify the symmetry corresponding to each peak. Their identifications and comparison are essential to select the peaks in the X-Ray diffraction pattern that will be relevant for the study of the mixed hydrate. Also, the temperature stability of the pure hydrate samples is tested to confirm the correct setting of the cooling method.

i. Preliminary identification of hydrate cubic structure.

X-Ray Diffraction patterns are identified from the known symmetry of the hydrate cubic structure and the simulated X-Ray Diffraction patterns of the SII and SI hydrate structure and the hexagonal Ice by VESTA software. In the X-Ray Diffraction pattern, the peaks are due to X-ray diffraction from crystallographic planes, noted by Miller indices as (h k l) X with X depending on the crystalline structure it belongs to (in this case: SI or SII for the hydrate structure and Ih for hexagonal Ice). The simulation of the X-Ray Diffraction pattern of the hydrate structure type SI and SII and hexagonal ice are indexed. The Figure IV. 2 shows the full indexation of the calculated pattern of the studied structure.

Some of the observed peaks of various structures are at a close position in the pattern. For

example, the peak of the SII structure noted (4 2 2) SII, the one of SI structure noted (2 2 2) SI and the peaks of the ice structure noted (1 0 1) Ih overlaps at the position around $2\theta = 26\ deg$. The same observation is made for the peaks (3 3 3) SII and (3 2 0) SI at $2\theta = 27\ deg$. (see Figure IV. 2). To better identify the formed structure of the mixed hydrate samples, we selected peaks isolated from one another. For the SII hydrate structure, the peaks noted (1 1 1) SII at $2\theta = 8.91$ deg. and (4 0 0) SII at $2\theta = 20.68$ deg. are chosen. The peaks noted (1 1 0) SI, (2 1 0) SI and (3 2 1) SI, respectively, at $2\theta = 10.5$, 16.74 and 27.1 deg. are specific for the SI hydrate structure. In the hexagonal Ice structure, the focus is on the peaks at $2\theta = 22.82$, 24.29 and 33.55 deg. respectively identified as (1 0 0) Ih, (0 0 2) Ih and (1 0 2) Ih (see Figure IV. 2).

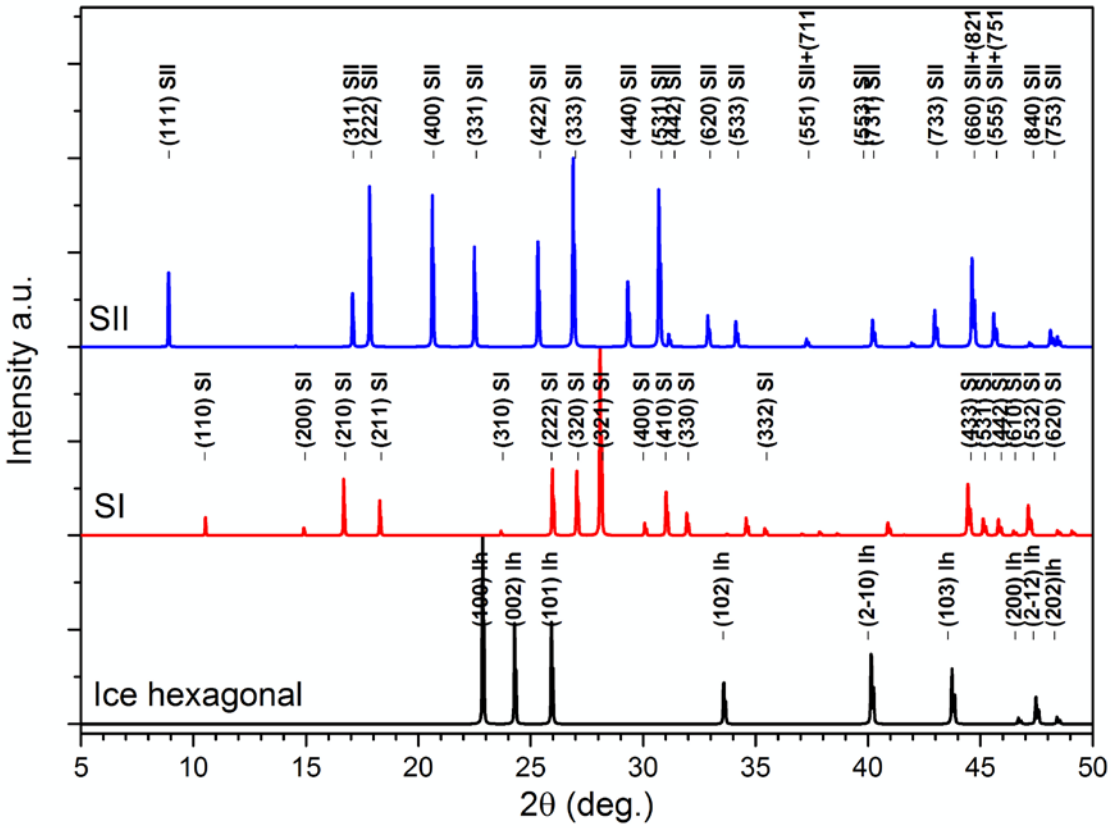

Figure IV. 2. X-Ray Diffraction patterns of the hydrate structure type SII (blue) and SI (red) and of the Hexagonal Ice (black), noted (h k l) X with respect to the structure (VESTA software).

ii. Experimental diffractograms of the reference systems.

In this section, the studied samples are the reference hydrates formed with a single species. The THF-17H_2O hydrate is known to form the SII hydrate structure and has a melting point at T_m= 277.4 K [MAK 05]. The $HClO_4$-5.5H_2O hydrate form the SI hydrate structure with a melting point T_m= 228 K.

The X-Ray Diffraction pattern of the THF-17H_2O sample (see Figure IV. 3) exhibits the peaks associated with the space group *Fd3m* corresponding to the SII hydrate structure. From 150 K to 270 K, we observed the pattern of SII hydrate structure. At 290 K, no crystalline pattern is observed. The melting point of the THF-17H_2O hydrate sample is determined between the 270 K and 290 K which agrees with the know melting point of the tetrahydrofuran hydrate (277.4 K) [MAK 05].

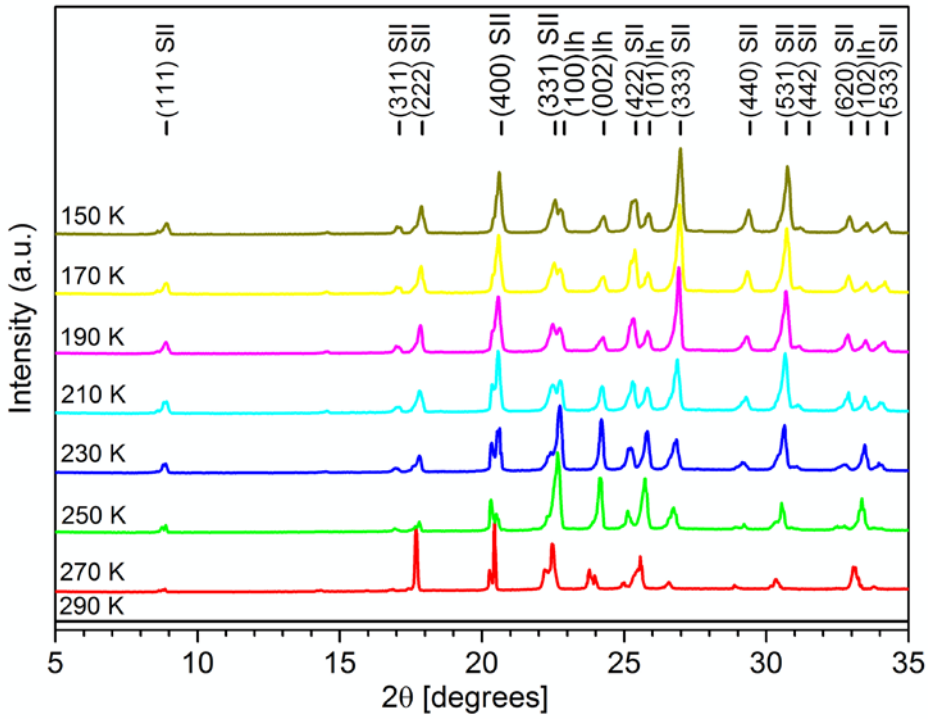

Figure IV. 3. X-ray Diffraction pattern of THF-17H_2O hydrate at different temperature.

The second reference sample is the perchloric acid hydrate of chemical formula $HClO_4$-5.5H_2O. The SI hydrate structure is expected for this water/acid ratio with a melting point known as T_m = 228 K [BRI 49].

The X-Ray Diffraction pattern of the $HClO_4$-5.5H_2O hydrate sample is shown in Figure IV. 4. Some of the peaks of the pattern associated with the space group $Pm\bar{3}n$ corresponding to the SI hydrate structure are overlapping with those of the hexagonal ice.

Between 210 K and 230 K, a decrease of the peak's intensity is observed. This is evidence of the sample melting. The complete melting of the sample is observed at 250 K.

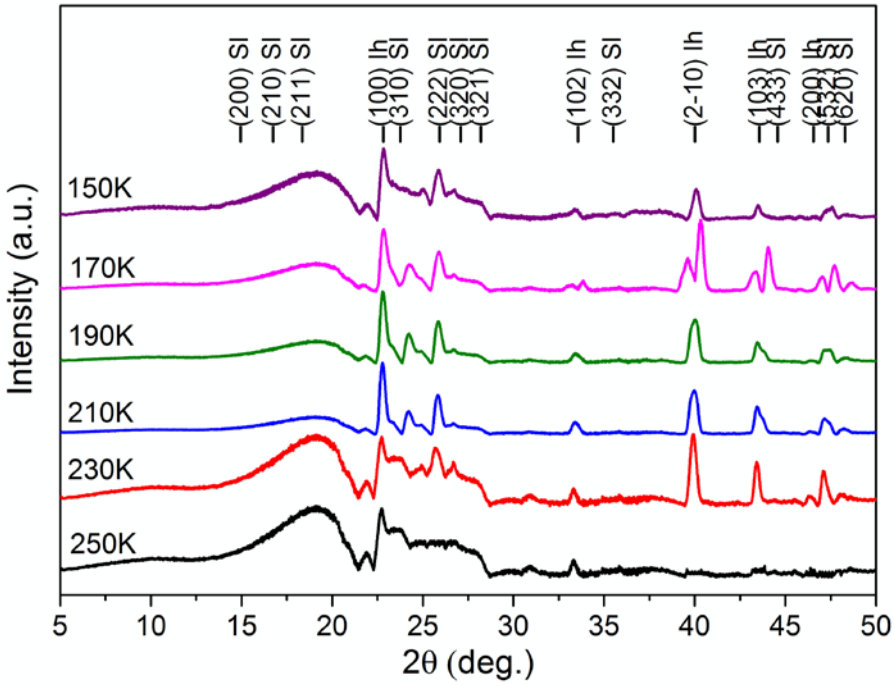

Figure IV. 4. X-Ray diffraction pattern of $HClO_4$-5.5$H_2$0. Melting of the sample is noticeable between 210 K and 250 K.

Because of the difficulties to identify the SI hydrate structure in the $HClO_4$-5.5H_2O sample, the X-Ray Diffraction pattern of the sample $HClO_4$-17H_2O is also studied. The patterns are shown in Figure IV. 5. The pattern of the SI structure is observed from 150 K to 200 K as well as the one for the hexagonal ice. The melting temperature for the SI hydrate structure is determined to be between 200 K and 210 K. The ice pattern is observed up to 240 K and then disappeared at 250 K. The complete melting point of the sample $HClO_4$-17H_2O is between 240 K and 250 K. The literature value for $HClO_4$-17H_2O melting is 250 K. The experimental result is in agreement with the literature value [BRI 49].

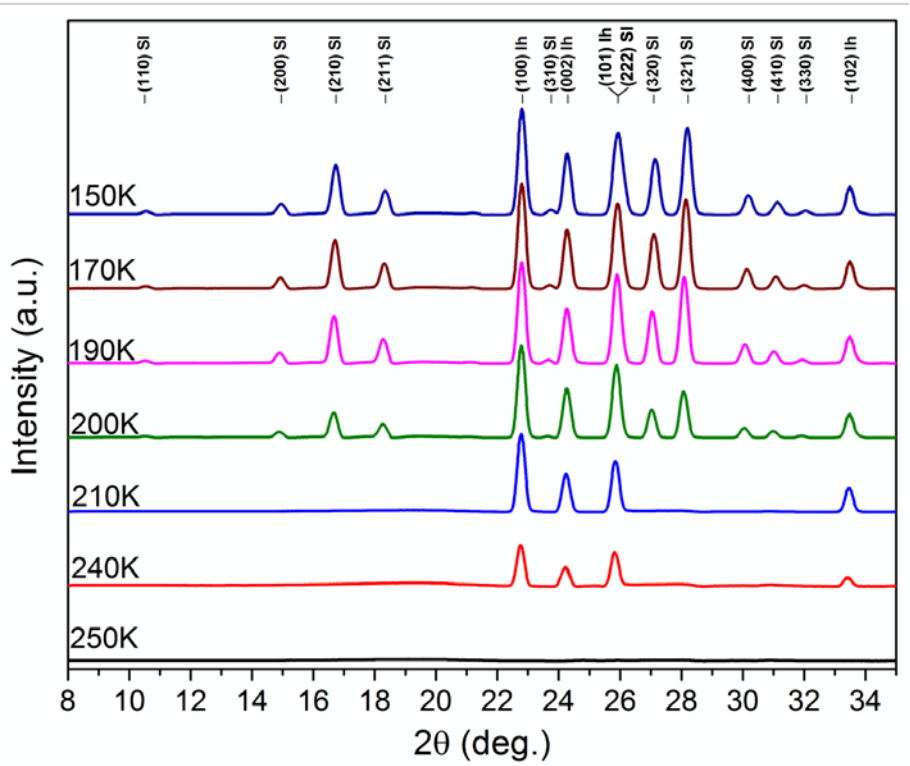

Figure IV. 5. X-Ray Diffraction patterns of HClO4-17H2O hydrate sample with peak identification noted as (h k l) X with X the associated structure from 150 K to 250 K

1. Mixed hydrates Structure analysis and indexation

The samples were made from the mixed of THF and $HClO_4$ with acid fraction from 0.35% molar to 4.6278 %mol (samples preparation Chapter II). In total, more than 10 samples were studied. We selected the more characteristic ones which are the 3 samples identifying domains where various structures were observed. They will be designated has low acid fraction, medium acid fraction and high acid fraction phases.

For the X-ray Diffraction experiment, liquid samples, trapped in a seal capillary, are placed under a nitrogen flux controlling the temperature. X-Ray diffraction pattern is recorded by heating the sample from 150 K to the melting point of the sample with a 10 K step, like the reference samples discussed previously (see also Chapter II).

For the first studied samples at low acid fraction, we expect to find only the SII hydrate structure from the previous study [DES 15]. Presented in Figure IV. 6 is the X-ray diffraction

pattern of the sample of $0.938\mathrm{THF}-0.063\mathrm{HClO_4}-17\mathrm{H_2O}$ formula corresponding to an acid fraction equal to 0.35 %mol. After the indexation, only the patterns for the SII hydrate structure and hexagonal ice are observed. Some characteristic peaks will be used for further study. For the SII hydrate structure, the (1 1 1) SII at $2\theta = 8.91$ deg., and for the ice, the peaks at $2\theta = 24.29$ deg., noted (0 0 2) Ih.

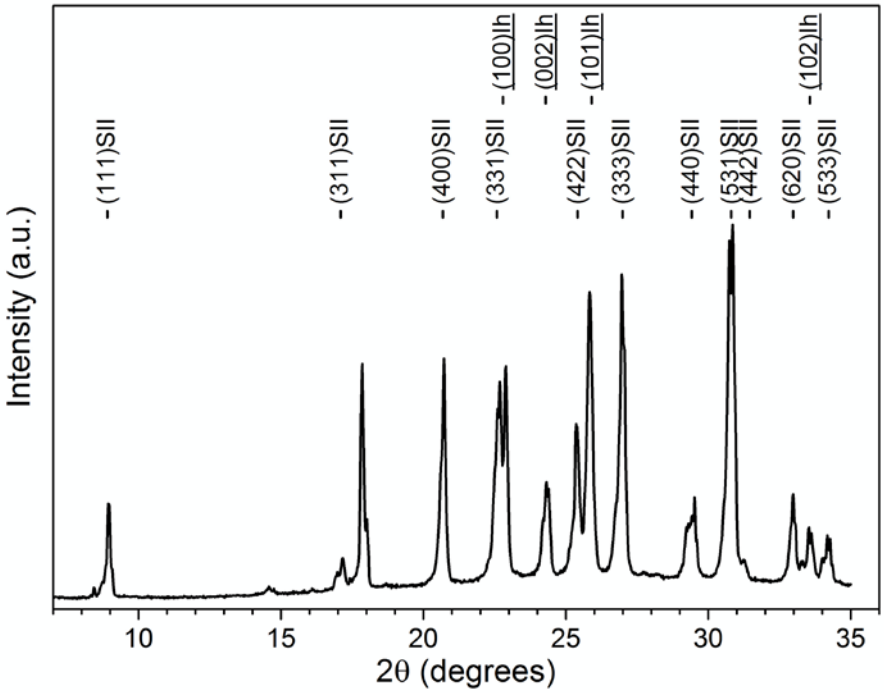

Figure IV. 6. X-Ray Diffraction pattern of mixed hydrate THF-HClO4 with acid fraction 0.35 %mol sample at 150K. Pattern identification is indexed as (h k l) X, with X for hydrate structure noted SIII and for hexagonal ice Ih.

Increasing the acid fraction in the mixed hydrate samples, a mixture of the various hydrate structure (SII and SI) and Ice is expected [DES 15].

X-Ray Diffraction pattern of mixed hydrate THF/$HClO_4$ with acid fraction = 0,694 %mol sample of chemical formula $(0{,}875\mathrm{THF}-0{,}125\mathrm{HClO_4}-17\mathrm{H_2O})$ show pattern belonging to two hydrate structure, SII and SI, and also the hexagonal ice structure, noted Ih. A full pattern indexation is shown in Figure IV. 7. The peaks which do not overlap with others are identified for each structure. On the X-Ray Diffraction pattern, 4 isolated peaks of SII structure are selected, corresponding to (1 1 1), (4 0 0), (6 2 0), and (5 3 3) at $2\theta = 8.91$, 20.68, 32.98 and

34.23 deg., respectively. Two peaks are identified for the SI structure at $2\theta = 14.96$ deg. and 28.21 deg., associated with (2 0 0) and (3 2 1). Ice structure pattern has two separated peaks corresponding to (0 0 2) at $2\theta = 24.29$ deg. and (1 0 2) at $2\theta = 33.55$ deg..

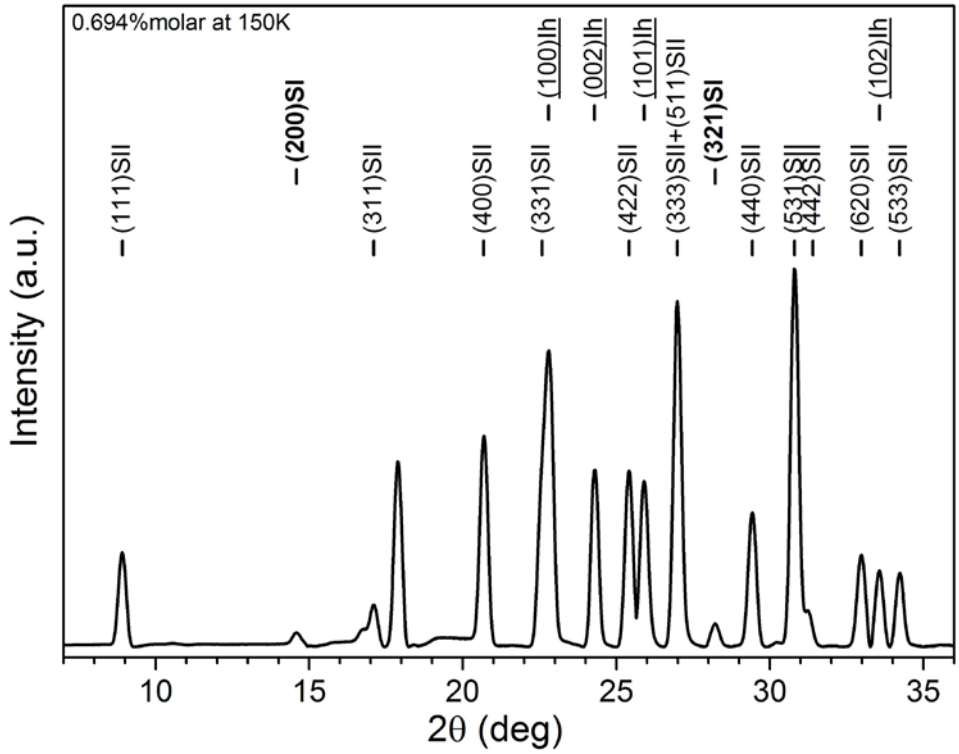

Figure IV. 7. X-Ray Diffraction pattern of mixed hydrate THF-HClO4 with acid fraction 0.694 %mol sample at 150K. Pattern identification is indexed as (h k l) X, respect to hydrate noted SII and SI and for hexagonal ice Ih.

Similar studies are conducted for the mixed hydrate sample with high acid fraction. When increasing the acid fraction, it is expected to observe the SII hydrate structure together with a large fraction of the SI structure and hexagonal ice. In Figure IV. 8, we present the indexation of the X-ray diffraction pattern of the mixed hydrate with acid fraction 4.628 %mol of chemical formula $(0{,}177\mathrm{THF} - 0{,}833\mathrm{HClO_4} - 17\mathrm{H_2O})$ at 150 K. The SI hydrate structure and hexagonal ice are found, whereas the SII hydrate structure is no longer observed.

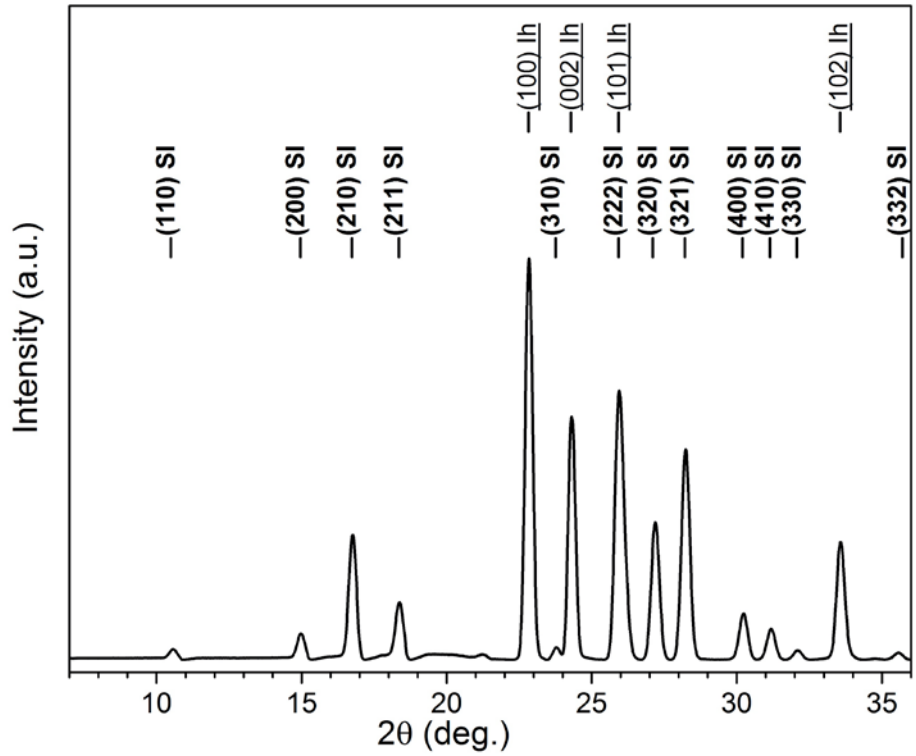

Figure IV. 8. X-Ray Diffraction pattern of mixed hydrate THF-$HClO_4$ with acid fraction 4.628 %mol sample at 150 K.

From the indexation, the localization of THF molecules is not addressed since the SII hydrate structure was not observed. This fact rises the possibility of THF molecules being guests in the SI hydrate structure with the $HClO_4$ molecules. Further studies are needed before concluding on the co-inclusion of THF and $HClO_4$ in SI structure. Analysing the SI structural stability as a function of the temperature might help in addressing the question of co-inclusion.

B. Analysing the structural stability

From the X-Ray Diffraction pattern, the peak intensity can be followed with respect to the temperature. The obtained curves give the structural stability of the sample. Boltzmann sigmoidal fit is done on the evolution of the peak's intensities for the SII and SI structure and ice to determine the temperature where any structural change occurs. The equation of the curve is given:

$$y = A_2 + \frac{A_1 - A_2}{1 + e^{\frac{(T-T_o)}{dT}}} \qquad (IV.44)$$

with A_1 is the initial value; A_2 is the final value; T_0 is the temperature corresponding to the mean value between these values; dT is the slope. A sketch of the function is given in Figure IV. 9.

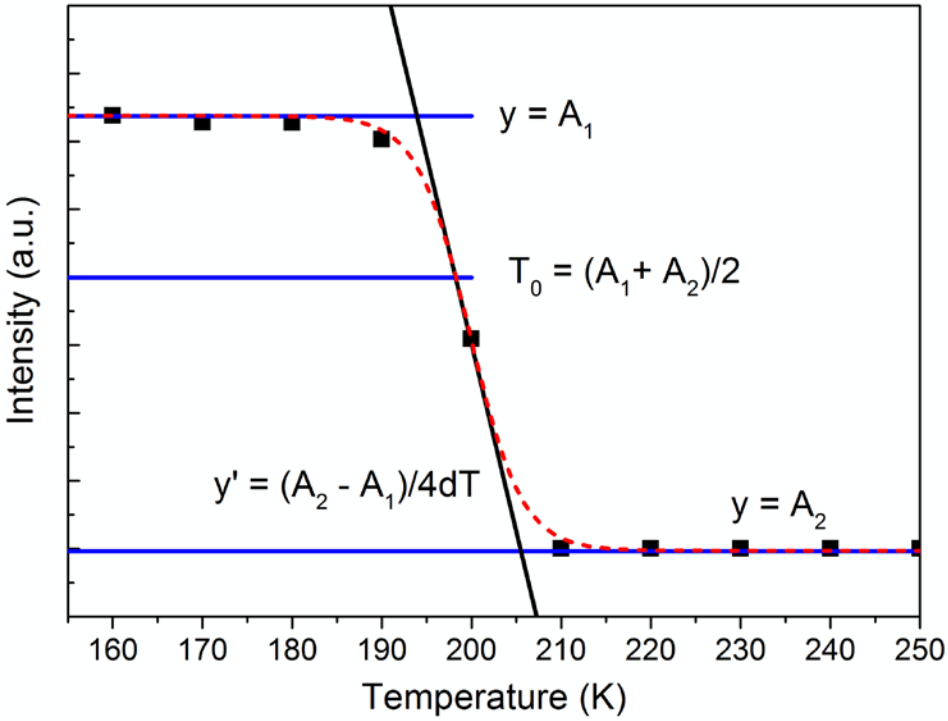

Figure IV. 9. Sketch of the method to determine the melting temperature with Boltzmann Fit.

The study is performed on the three samples presented before. They are representative of the three structural domains of mixed structure, identified by X-ray diffraction. The intensities of specific peaks of each structure with respect to the temperature are studied to determine the melting temperature of each structure for various acid concentrations.

1. Low acid fraction

The sample with low acid fraction (0.35 %mol) is studied from 150 K to 270 K with 20 K steps.

The evolution of the X-ray diffraction pattern with the temperature is shown in Figure IV. 10. The crystalline structures of the SII hydrate and of the hexagonal ice were indexed. The pattern of the SII structure is observed up to 230 K. At 250 K, the hexagonal ice pattern is the only one present. At 270 K, no pattern signature is identified. The sample is in a liquid state. If we look at the peak's evolution of the ice structure, an increase of the intensity is remarked at 210 K until 250 K before its disappearance. To complete the observation, Figure IV. 11 shows the evolution of the peaks intensity depending on the temperature for the peaks (101) Ih and (111) SII and (333) SII for the SII hydrate structure.

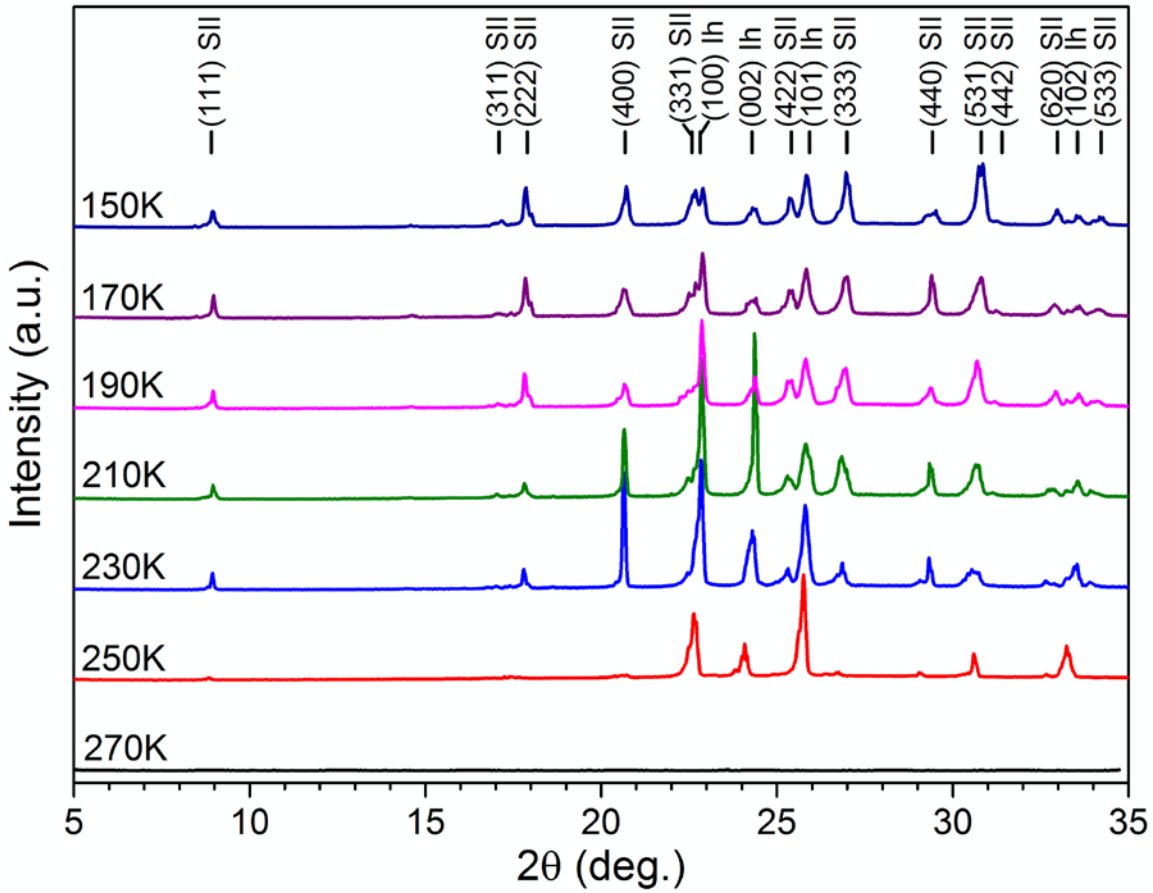

Figure IV. 10. X-Ray Diffraction pattern of mixed hydrate THF-$HClO_4$ with acid fraction 0.35 %mol at temperatures specified on the graph.

The increase of the ice peaks intensity (101) Ih between 210 K and 250 K corresponds to the decrease observed for the peaks of (333) SII and (111) SII at the same temperature. (see Figure IV. 11). With Boltzmann fit equation presented before, the melting temperature of the crystalline structure can be determined. The Boltzmann fits are represented by dash lines in

Figure IV. 11 . The Boltzmann fit is performed on the evolution of the peaks (111) SII, and the fitted parameters are given in Table IV. 1. The parameter T0 will be considered as the melting temperature of the structure. The SII structure has a melting point of $250.28 \pm 3.67\ K$. The Boltzmann fit is also performed on the evolution of the peaks (333) SII (see Table IV. 2). The melting point obtain is at $253.54 \pm 3.97\ K$. The two values obtained are in the error range. Sadly, the peak intensity of the ice structure varies too much to allow the identification of the melting point with a Boltzmann fit. However, following the disappearance of the ice peaks, the melting temperature can be identified between 250 K and 270 K.

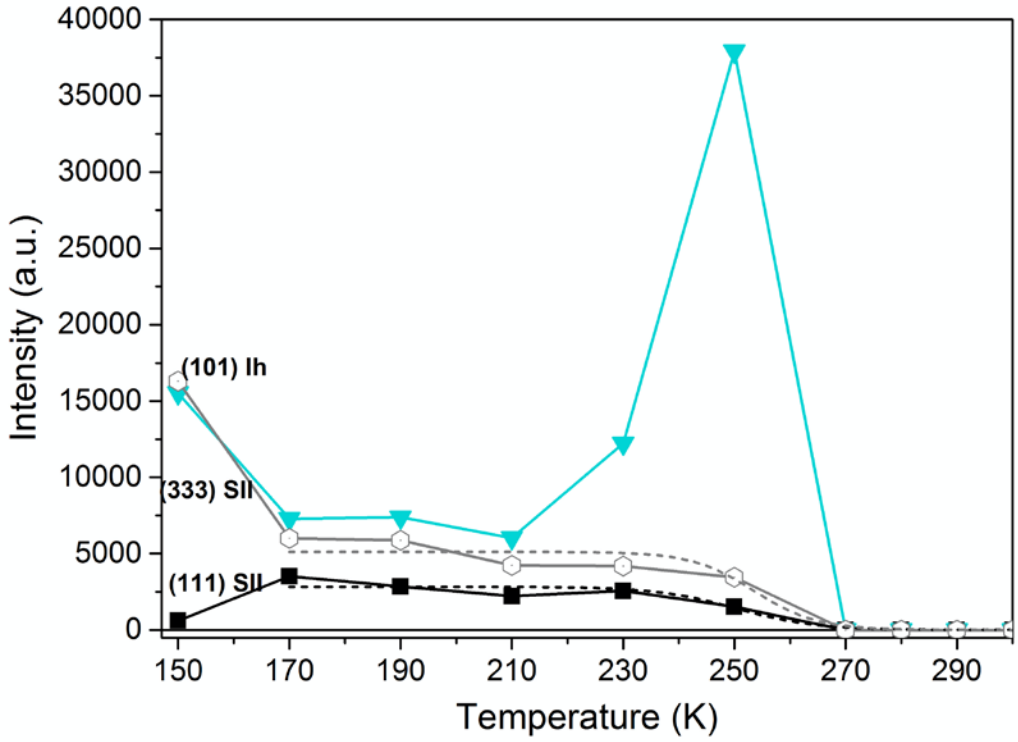

Figure IV. 11. Evolution of peaks intensity of THF-HClO4 mixed hydrate with acid fraction 0.035 %mol depending on the temperature, specifically peaks associated to the plane (002) Ih (triangle, light blue) and (111) SII (square, dark) and (333) SII (empty hexa, grey) fitted by Boltzmann sigmoidal (dash).

Table IV. 1. Boltzmann Fit data for the peaks (111) SII for the low acid sample at 0.035 %mol.

	Value	Standard error
A1	2833.316	198.723
A2	0	0

T0	250.280	3.666
dT	7.149	4.248

Table IV. 2. Boltzmann Fit data for the peaks (333) SII for the low acid sample at 0.035 %mol.

	Value	Standard error
A1	5118.507	363.184
A2	0	0
T0	253.546	3.976
dT	5.649	4.286

From the stability study of the SII hydrate structure in the mixed hydrate of THF/$HClO_4$ with low acid fraction, the melting point found is lower than for the pure THF hydrate in the SII structure. The acid molecules, as well as the presence of ice, destabilized the hydrate structure.

2. Medium acid fraction

The X-Ray Diffraction pattern of mixed hydrate THF-$HClO_4$ with acid fraction = 0,694 %mol change depending on the temperature (see Figure IV. 12). As identified before, at low temperature (150 K), we observe the pattern of three structures. The peaks associated with the SI hydrate structure are no longer observed at 190 K. Then at 260 K, the intensity of the peaks associated with the ice structure decrease and disappear at 270 K. The X-Ray Diffraction pattern is now the one specific to the SII hydrate structure without Ice. To determine the temperature where the transition occurs, the peak intensity for each structure is monitored. For this study, isolated peaks of the structure are selected: for the structure SII, the peaks (1 1 1) SII at $2\theta = 8.91$ deg., the peak (3 2 1) SI at $2\theta = 28$ deg. and Ice peaks at $2\theta = 24.29$ deg. and 33.56 deg. corresponding to (0 0 2) Ih and (1 0 2) Ih, respectively.

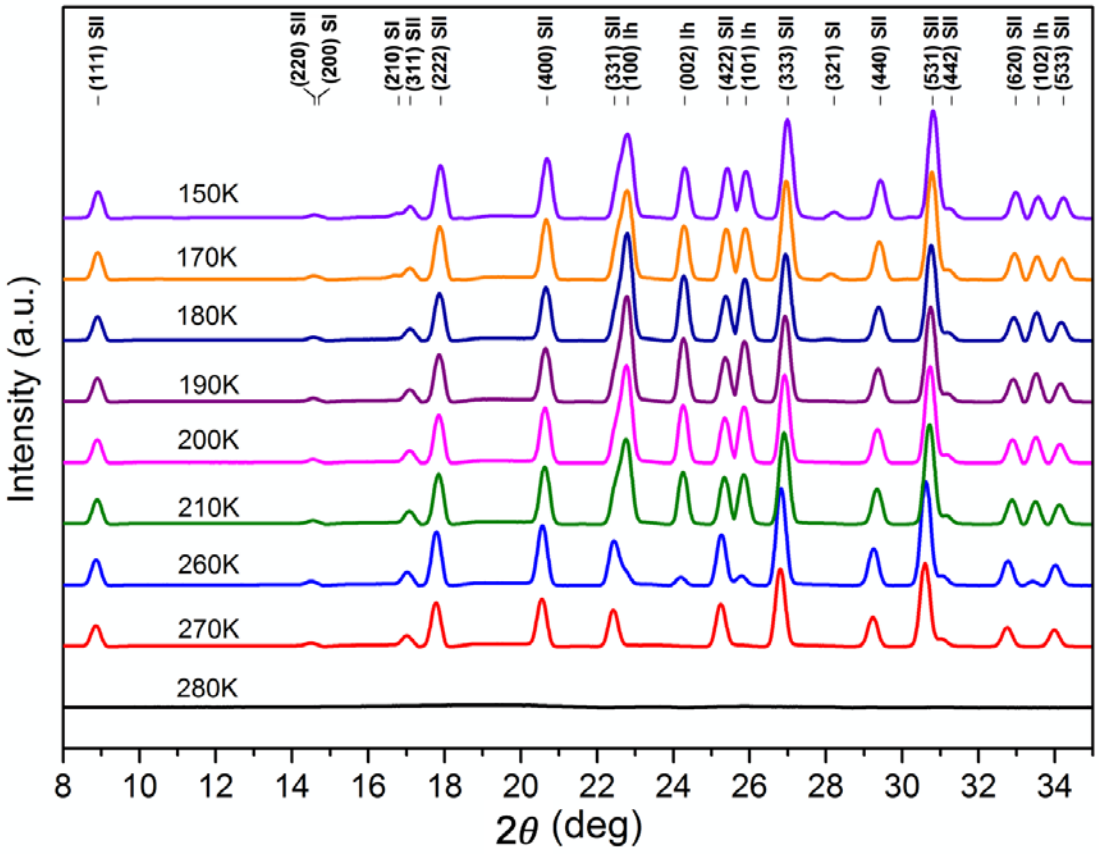

Figure IV. 12. X-Ray Diffraction pattern of mixed hydrate THF-HClO4 with acid fraction 0.694 %mol at the temperature specified on the graph, peaks noted (h k l) X with X corresponding to the structure.

The thermal dependences of the (3 2 1) SI, (1 1 1) SII, (1 0 2) Ih and (0 0 2) Ih peaks are shown in Figure IV. 13. The ice peaks have similar thermal evolution. There are constant from 150 K to 170 K, then a sudden increase is observed at 180 K. From 180 K to 260 K, the peak intensities decrease and reach zero at 270 K. The peak intensity for (3 2 1) SI decreases from 160 K to 190 K. The peaks (1 1 1) SII for the SII hydrate structure have an intensity mostly constant (except for a light decrease between 180 K and 200 K) and disappear at 280 K where the sample is in the liquid state.

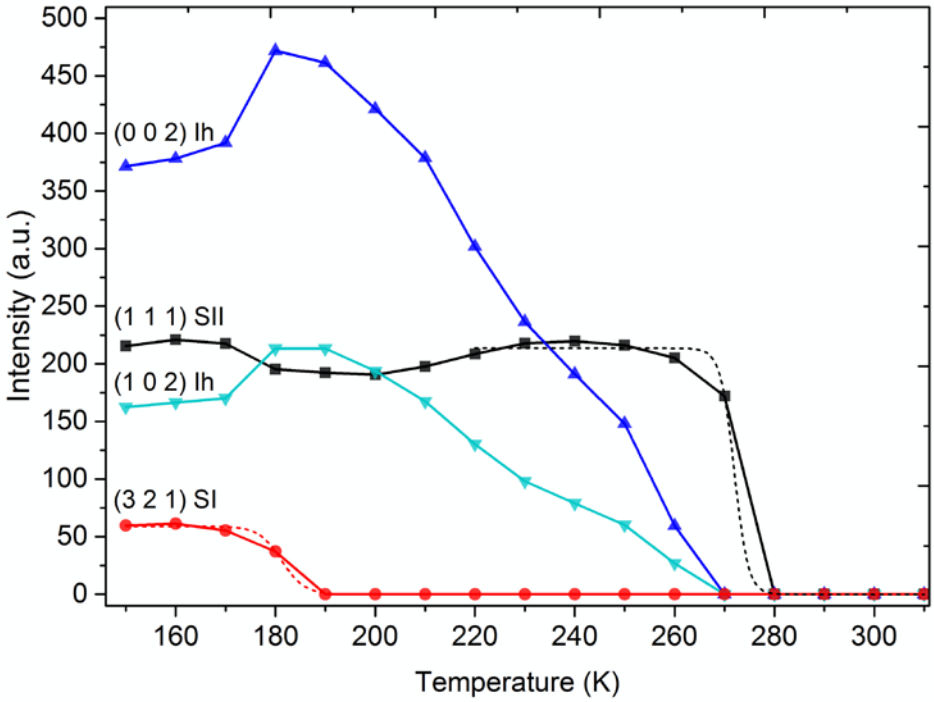

Figure IV. 13. Evolution of the peaks intensity of THF-HClO4 mixed hydrate with acid fraction 0.694 %mol depending on the temperature of the X-Ray Diffraction, specifically peaks associated to the plane (321) SI (circle, red), (102) Ih (down triangle, blue), (002) Ih (up triangle, light blue) and (111) SII (square, dark) and fitted by Boltzmann sigmoidal (dash).

Focusing on the SI hydrate structure stability, the melting temperature observed here at 190 K is 20 K below the expected melting temperature for any concentration of $HClO_4$ with water. The temperature where the SI hydrate structure with $HClO_4$ guest start melting also corresponds to the temperature where the SII hydrate structure peak intensity lightly decreases, and ice peak intensities increase. This increase indicates an important Ice formation as well as the SII hydrate structure formation.

At 190 K, the SI hydrate structure is not observed, meaning at least part of the water from the SI hydrate structure is transformed into hexagonal Ice. The ice formation is followed by its melting between 190 K and 200 K. The destabilisation of the ice proves the presence of acid molecules mixed up with it. Since they are no more in hydrate structure, we can talk about hydrated acid molecules. The presence of acid molecules within the ice destabilizes the hexagonal structure and lowers its melting temperature, normally at 273 K for pure hexagonal ice; here, the acidic ice start melting between 190 K and 200 K.

Boltzmann sigmoidal fit is done on the evolution of the peak intensities for the SII and SI structure to determine the temperature where structural change occurred. The melting temperature for SII structure found with Boltzmann sigmoidal fit is $271.9 \pm 2.54\ K$ with the data range selected from 230 K to 310 K. The fitting data to determine the melting point of the SII structure are presented in Table IV. 3. For the SI structure, the melting temperature is determined at $181.19 \pm 0.31\ K$ (see Table IV. 4).

Table IV. 3. Boltzmann Fit data for the (111) SII in the medium acid sample at 0.694 %mol.

	Value	Standard error
A1	213.453	2.312
A2	-0.160	2.982
T0	271.972	2.543
dT	1.384	1.774

Table IV. 4. Boltzmann Fit data for the (321) SI in the medium acid sample at 0.694 %mol.

	Value	Standard Error
A1	58.953	0.687
A2	-0.089	0.3318
T0	181.193	0.315
dT	2.277	0.504

The sample at medium acid fraction studied above shows the stability challenge of the SI and SII structures in the mixed hydrate. In this sample, the SII hydrate structure has a melting point of 271.9 K, close to the one of the pure THF hydrate (277 K). The presence of the SI structure does not destabilize the SII structure. However, the melting temperature for SI is determined at 181 K. The pure $HClO_4$ hydrate has a melting temperature of 228 K [MOO 87]. The 40 K difference between the pure hydrate and our sample highlights a destabilization effect happening in the mixed hydrate. Different hypothesis are proposed. The presence of the mixing of SI and SII structure destabilized the hydrate in SI structure. Another hypothesis is

that the composition of the SI hydrate is different from the one of pure HClO4 hydrate. By their nature, the hydrate structure and stability is link to the guest molecules. The inclusion of THF with HClO4 molecules in SI hydrate can explain the destabilisation of the structure. The THF molecules are larger than the CO_4^- anion constituting the hydrate in the pure form. Complementary study needs to be performed to confirmed the hypothesis of the co-inclusion of THF and HCLO4 in SI hydrate.

3. High acid fraction

A similar study was performed on a high acid fraction sample, where only the structure SI and hexagonal Ice were observed, as shown previously.

The X-Ray Diffraction patterns of mixed hydrate THF-$HClO_4$ with acid fraction at 3.671 %mol depending on the temperature, are shown in Figure IV. 14. At low temperatures, the pattern of two structures is formally observed. Some peaks of the different structures overlap with one another. In particular, some peaks that could be identified as the SII hydrate structure might be completely overlapping with peaks of the SI hydrate structure and ice Ih. Because of the low concentration of SII structure, expected for the samples at 3.671 %mol, no isolated peaks for SII are observed. It is not possible to confirm the presence of the SII structure. The peaks for SI hydrate structure and ice structure Ih are easily identifiable. The peak of SI structure at 10.5 deg. corresponding to the plane (1 1 0) SI and at 28.21 deg. the plane (3 2 1) SI. Ice peaks around 22.82 deg., 24.29 deg. and 33.55 deg. corresponding respectively to (1 0 0) Ih, (0 0 2) Ih and (1 0 2) Ih. The stability of the structures is studied by following the evolution of peak intensities with the temperature from 150 K to 260 K with 10 K steps. The peak associated with (3 2 1) SI of the SI hydrate structure is no longer observed at 200 K. The only X-Ray Diffraction pattern at temperatures higher than 200 K is the diffraction pattern specific to the hexagonal ice structure.

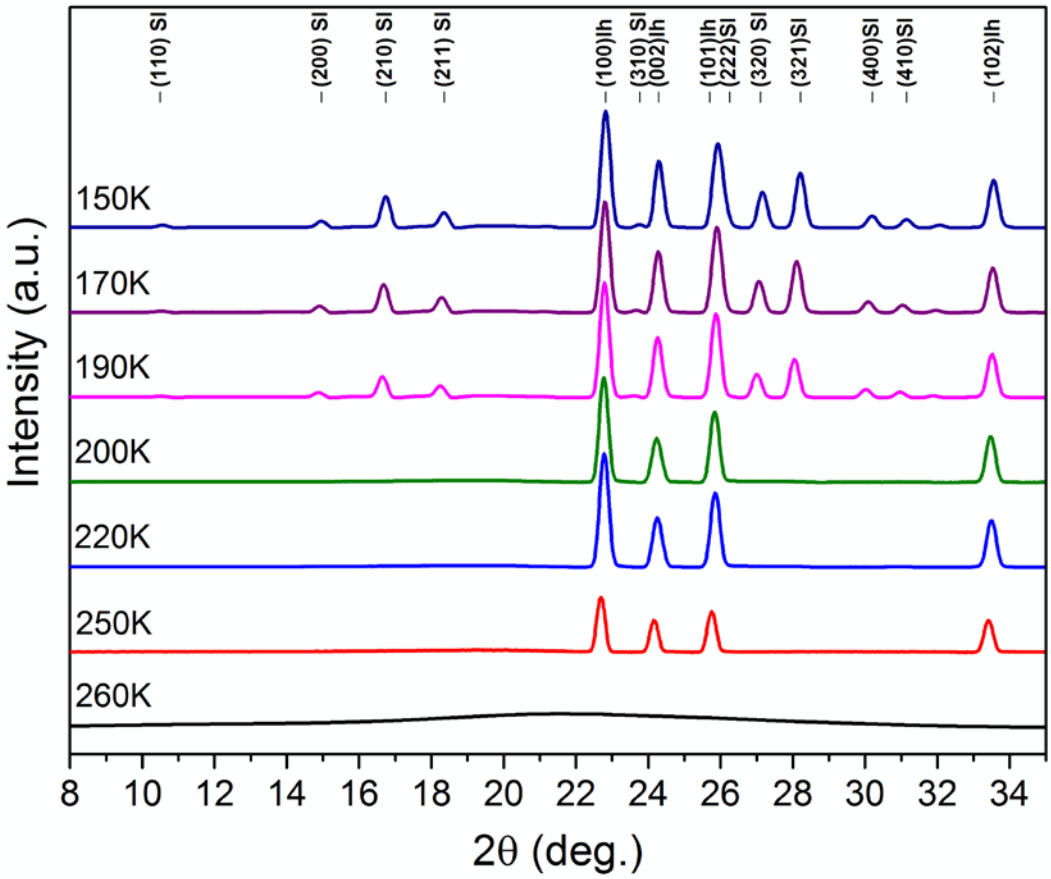

Figure IV. 14. X-Ray Diffraction pattern of mixed hydrate THF-HClO4 with acid fraction 3.671 %mol sample at various temperatures from 8 to 35 deg.

To determine the structural stability, the evolution of the peak intensities with respect to the temperature is studied (see Figure IV. 15). We focus on the evolution of two peaks for each structure: the peaks (1 0 0) Ih and (0 0 2) Ih, and (3 2 1) SI and (2 1 0) SI. The study of the sample with acid fraction at 3.671 %mol is presented in Figure IV. 15. The decreased of the SI peaks intensity start at 180 K and disappear at 200 K. The intensity of the ice peaks show a little increase at 180 K to then start to decrease slowly to 260 K where all the sample turn to liquid. Boltzmann Fit are done on the intensity evolution to determine the melting point of each structure. The parameter from the fit are given in Table IV. 5 and Table IV. 6. The melting point is found at $245.84 \pm 1.37\ K$ for the hexagonal ice. The melting point of the structure SI is determined $191.52 \pm 0.77\ K$. The melting temperature for SI and Ice are found lower than their reference values. The new stability property indicates a change in the hydrate structure which influence the melting temperature. For this sample, the THF molecules can not be

localised. The possible co-inclusion of THF and HClO4 in Si hydrate structure might be causing the destabilisation of the SI structure observed.

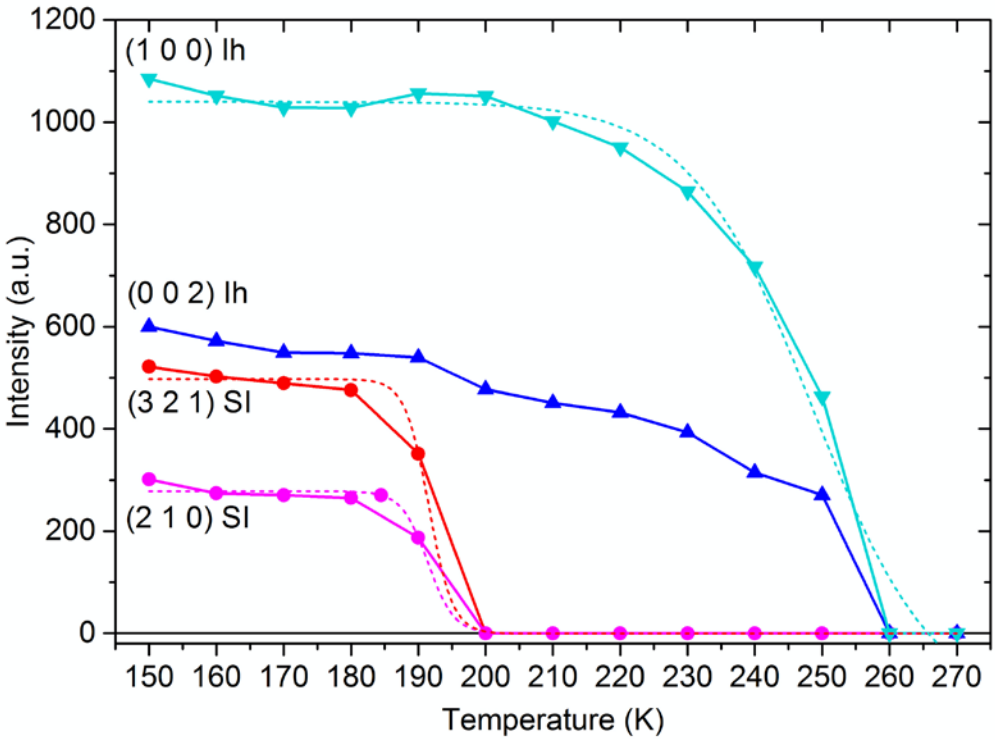

Figure IV. 15. Evolution of the peak intensities of THF-$HClO_4$ mixed hydrate with acid fraction 3.671 %mol depending on the temperature of the X-Ray Diffraction, specifically peaks associated to the plane (321) SI (circle, red), (210) SI (circle, pink), (100) Ih (down triangle, light blue), (002) Ih (up triangle, blue) and fitted by Boltzmann sigmoidal (dash).

Table IV. 5. Boltzmann Fit data for the (100) Ih in the high acid sample at 3.671 %mol.

	Value	Standard Error
A1	1031.208	22.421
A2	0	0
T0	245.846	1.317
dT	7.160	1.147

Table IV. 6. Boltzmann Fit data for the (321) SI in the high acid sample at 3.671 %mol.

	Value	Standard Error
A1	497.513	5.359
A2	0	0
T0	191.518	0.769

dT	1.732	0.865

Thanks to the XRD study, the diagram of the structural stability of the mixed hydrate according to the acid fractions and the temperature is determined in Figure IV. 16, as a summary of the melting temperature obtained by studying the evolution of the XRD peaks of the various structures for each sample. In Figure IV. 16, the three domains for low, medium and high acid fraction samples are represented in blue, purple, and red, respectively, for the temperature where all the hydrate structures are stable (T < 200 K). At medium acid fraction, called domain 2, the structures change with the temperature. First, SI, SII and Ice structures are observed (purple), then for T > 200K, only the SII and Ice structure remain (blue). For the samples in high acid fraction, domain 3, the structures change from a mix of SI and Ice structures (red) to only ice (grey) at T = 200 K.

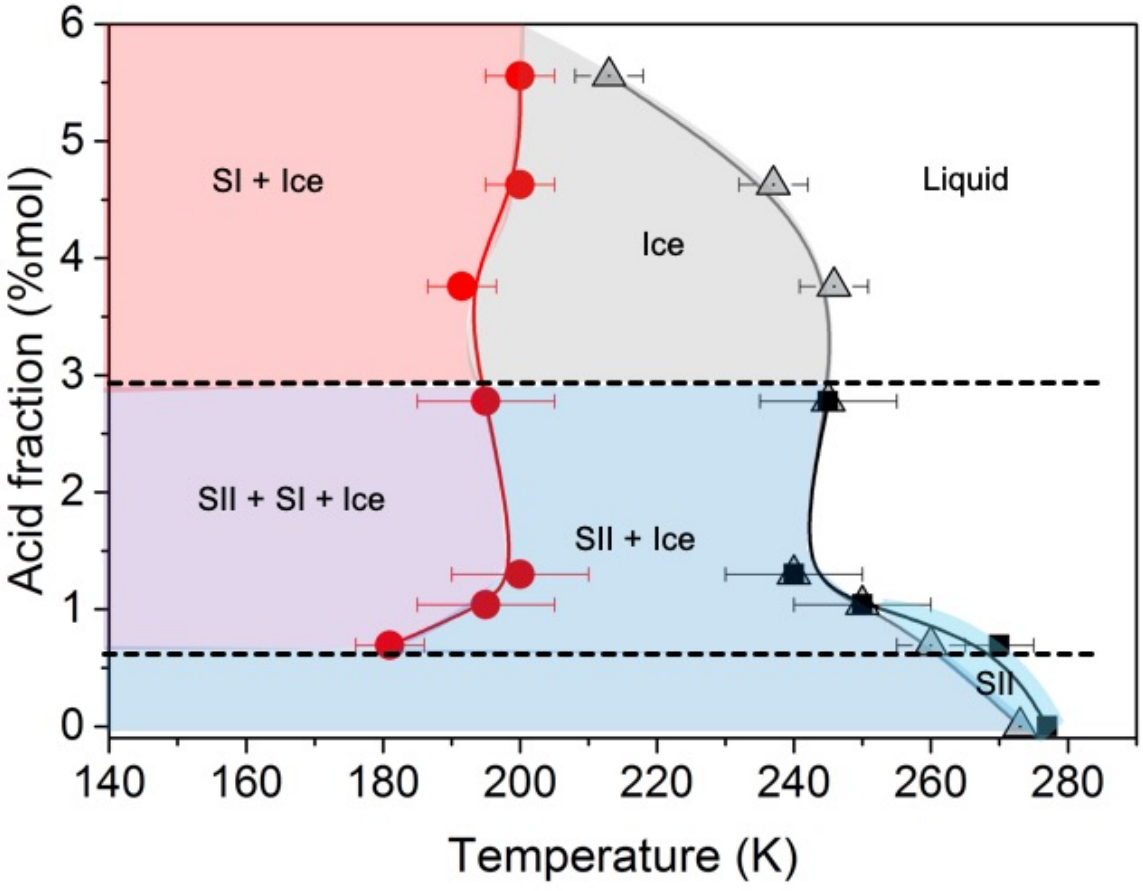

Figure IV. 16.Diagram of the structural stability of mixed hydrate with various acid fractions and temperatures. The melting temperature of SI (red dot), SII (black, square) and Ice (grey, triangle).

X-ray diffraction experiments showed, for low acid fraction samples, that the ice structure melted before the pure hexagonal ice structure (T_m= 273 K), proving that the stability of the ice in the sample is disrupted. One hypothesis is that the acid molecule or THF molecule destabilised the ice. Their mixing with the ice structure creates ice with impurities. This implies that not all the acid molecules are forming a hydrate structure; some are "lost" in the ice.

The structural stability of the mixed hydrate is one of the parameters that will influence the protonic conductivity. Therefore, quantifying the formed structures in the mixed hydrates needs to be considered to evaluate the impact of the changes happening in the samples.

C. SII and SI hydrate structure: a quantitative study

X-ray diffraction experiments highlighted the presence of various hydrate structures and ice in the sample depending on their acid fraction. From the XRD pattern, the peaks give an intensity corresponding to the concentration of a specific structure. This relation between peak intensities and concentration allowed us to follow the evolution of the different structures with the temperature (see in the previous section).

The intensity allows us to deduce also a relative fraction of the various structures for each sample at a given temperature. For example, the relative fraction of SII is given by:

$$Relative\ fraction_{SII} = \frac{I_{SII}}{I_{SII} + I_{SI} + I_{Ih}} \qquad (IV.45)$$

The relative fraction of each structure is found for various acid fraction at fixed temperature. The sum of the three relative fractions of SII, SI and Ice is equal to 1. The relative quantitative study is performed at the temperature where the structures are the most stable, 170 K.

The relative fraction of the three structures gives indications of the structural arrangement of

the various samples. In Figure IV. 17, the relative fraction of the structures in the mixed hydrate samples for various acid fractions is shown for temperature fixed at 170 K. The structural stability domains are indexed by colour: domain 1 in blue, domain 2 in purple and domain 3 in red, in Figure IV. 17, with the results found in the previous section. In domain 1, the sample at zero acid fraction shows a relative fraction for ice a little bit higher than for the SII structure. For the sample with an acid fraction of 0.035 %mol, the relative fraction of SI is zero, as expected (see the previous section and [DES 15]). The relative fraction of the SII structure is at 0.9, and the ice structure one is lower than 0.1. From this observation, the presence of acid seems favourable to the formation of the SII hydrate structure. This observation is confirming again the co-inclusion of the acid molecules by replacing some of the THF guest in SII structure. In domain 2, when increasing the acid fraction, the relative fraction of the SII structure decreases while the ice structure shows an increase of 0.1. The SI structure can also be observed and has a relative fraction increase from 0.1 to 0.3. In domain 3, SII structure is no longer present. The relative fraction of SI increase up until 0.8 as the relative fraction of Ice decrease.

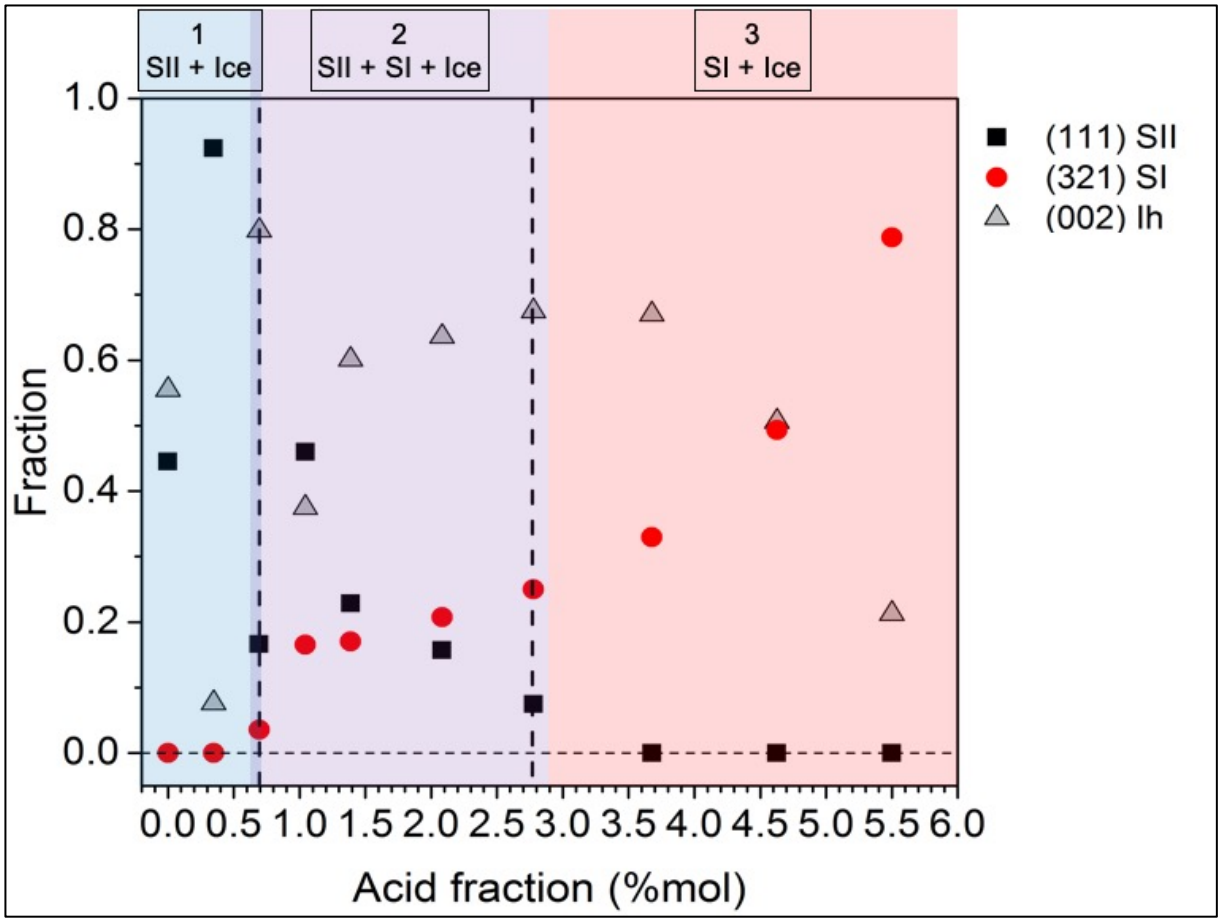

Figure IV. 17.The relative fraction of the SI, SI and Ice structures in mixed hydrate samples for various acid fractions at 170 K. (111) SI Peak (black, square), (321) SI (red, circle) and (002) Ih (grey, triangle). The structural domains are also noted.

At the limit between domain 1 (SII + Ice) and domain 2 (SII + SI + Ice) (respectively in blue and purple in Figure IV. 17), the sample 0.694 %mol show an ice relative fraction much higher than the other samples. The relative fraction of the hydrate structure is small compare to it. This phenomenon is explained by the number of water molecules used to formed the various hydrate structure. When 136 H_2O is needed to formed the unit-cell of the SII structure, only 46 H_2O is used to form the SI structure (see details in Chapter I). The formation of SI structure explains the "excess" of water that is forming ice at 170 K. It also explains the decrease of the SII hydrate structure since when you increase the acid fraction in the sample, the THF fraction decrease. Less THF molecules are then available to form the SII hydrate.

For the samples with acid fraction between 0.69 %mol and 2.77 %mol, various observation

can be made. The fraction of SII decrease as the fraction of SI increase which indicates that the acid molecules at this concentration are forming the SI hydrate structure. The ice relative fraction increases lightly due to the difference in the hydrate structure formed. As explained before, the SI needs fewer water molecules than the SII.

The information collected on the relative fractions of the various structures is used, in the Chapter V, to interpret the impedance measurements and to implement models to explain the protonic conductivity in the mixed hydrate.

D. Localization of the guest inside hydrates cages

1. Cell parameter and Thermal Expansion

From the X-Ray Diffraction pattern of the mixed hydrates samples, the cell parameter of each structure can be calculated. Due to crystalline structure of the hydrate, the peak corresponds to crystallography symmetry plane that can be identify. The localisation of the peaks is in relation to the inter-reticular distances in the crystal. The cell parameter determination is different for a cubic symmetry or hexagonal one. The followed relations are used to calculate the cubic cell parameter of hydrate and also the hexagonal parameter for the ice structure. From the XRD studied in temperature, the influence of temperature on the cell parameter is determined. The structure cell parameter evolution depending on the temperature is called the thermal expansion.

For cubic crystalline structure, the formula to calculate the cell parameter a is given by:

$$a = \sqrt{h^2 + k^2 + l^2} \times d \qquad (IV.46)$$

With $(h\ k\ l)$ are the Miller indices used for the peak identification on the XRD pattern, and d the peak position at 2θ. For hexagonal crystal, the structure parameters are given by:

$$\frac{1}{d^2} = \frac{3}{4}\left(\frac{h^2 + hk + k^2}{a^2}\right) + \frac{l^2}{c^2} \qquad (IV.47)$$

In Figure IV. 18, the evolution of the cell parameter for the structure SI from the X-ray diffraction pattern is shown for the different samples: the $HClO_4$ -17 H_20 hydrate sample and the mixed hydrate with acid fraction 0.69 %mol and 4.63 %mol. The reference curves are calculated from the theoretical formula of the thermal expansion for hydrate structures [HES 07] [SHI 11]. The reference value of the structures cell parameter is displayed in Figure IV. 18 (black point and line).

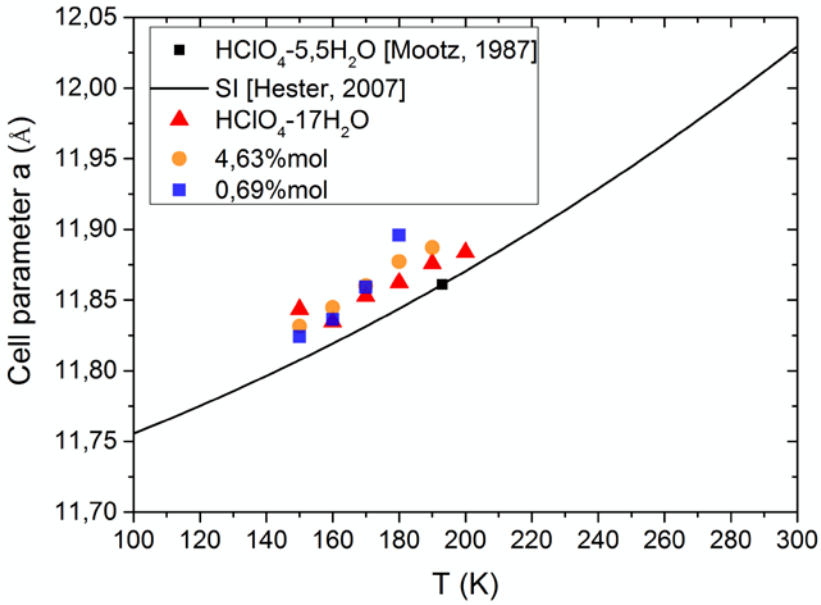

Figure IV. 18. Thermal expansion of SI structure cell parameter. Reference (black), $HClO_4$ -17 H_20 sample (triangle, red) and mixed hydrate samples at 4.628 %mol (circle, orange) and at 0.694 %mol (square, blue) [HES 07] [SHI 11].

In Figure IV. 18, the SI cell parameter found for the mixed hydrate samples is in good agreement with the reference data from Mootz *et al.* [MOO 87] but slightly higher. The flexibility of the hydrate cage, when associated with acid molecules, has been observed in the work of Desmedt *et al.* [DES 15]. The mixture of hydrate structure might influence the cell parameter of the SI hydrate and facilitate the inclusion of another species. These results obtain by considering only one peak of the SI structure are a good first step to the proof of the inclusion of THF molecules in SI hydrate with $HClO_4$. A study taking into account the full pattern of SI is needed to confirm this preliminary result. The structure resolution by Rietveld refinement would be ideal.

2. Discussion on DFT simulation to resolve the mixed hydrate guest configuration.

As shown in Chapter III, DFT simulations allowed testing the stability of the hydrate structure for various guest.

From our XRD study, the mixed hydrate forms only the SII hydrate structure for the samples with an acid fraction lower than 0.69%mol. The sample at 0.69 %mol have the chemical formula: 7 THF- 1 $HClO_4$ - 136 H_2O, which corresponds to the SII structure unit cell with all the 8 larges cages filled. In the paper of Desmedt *et al.* [DES 15] with the mixed hydrate of THF and $HClO_4$.in SII structure, they resolved the co-inclusion of $HClO_4$ molecules in the SII structure with the THF molecules. However, due to the presence of oxygen molecules in the acid species, a reaction with the water molecules of the hydrate sub-structure is possible. The possible participation of the acid's oxygen to form the hydrate cage is raised.

From the XRD experiments presented, the encapsulation of THF molecules in the SI hydrate structure in the samples of mixed hydrate with high acid fractions is a possibility. The localization of the THF molecules in samples forming only the SI structure could be addressed by quantum calculations. The project was to test the possibility of the THF molecules encapsulating with the acid in SI hydrate structure. The ideal acid hydrate formed the SI structure with all cages (2 small and 6 large cages) occupied by $HClO_4$ molecules giving the chemical formula $HClO_4$-5.5H_2O (see Chapter I) [MOO 87]. In this case, the anionic species (ClO_4^-) is the principal guest in the hydrate structure. To test the stability of the THF inside the SI structure, one of the ClO4- in the large cages and the H+ from the host substructure are removed. The THF molecules is placed at the centre of the large cage.

Due to the presence and mobility of the extra proton inside the sub-structure of the hydrate, the reactivity of the various charged species complicated the calculs of the stable structure (looking for the minimum total energy).

DFT calculation on the position of the guest in the mixed hydrate of THF-HClO4, especially the position of the acid molecules, didn't lead to conclusive results. The disorder of the SI hydrate structure might be one of the factors that make this simulation challenging. The high mobility of the proton in the case of $HClO_4$ hydrate is to be considered.

Further study by Ab-initio simulation could be performed to resolved the issues with the proton mobility.

E. Conclusions

The mixed hydrate of THF/$HClO_4$ with various acid fractions has been studied in order to have a better understanding of the influence of acid molecules on the hydrate stability and structure.

A partial summary of the structural findings by XRD are presented in Figure IV. 19 and the three structural domains are identified. One domain (in blue) is for the samples with a low acid fraction from 0 to 0.69 %mol excluded where the SII hydrate structure is observed with ice. The second (purple) represent when the three structures cohabiting, the SII and SI hydrate structures and the hexagonal ice for the samples of acid fraction up to 2.77 %mol. For samples with higher acid fractions, only the SI hydrate structure is found, it's the domain 3 (red).

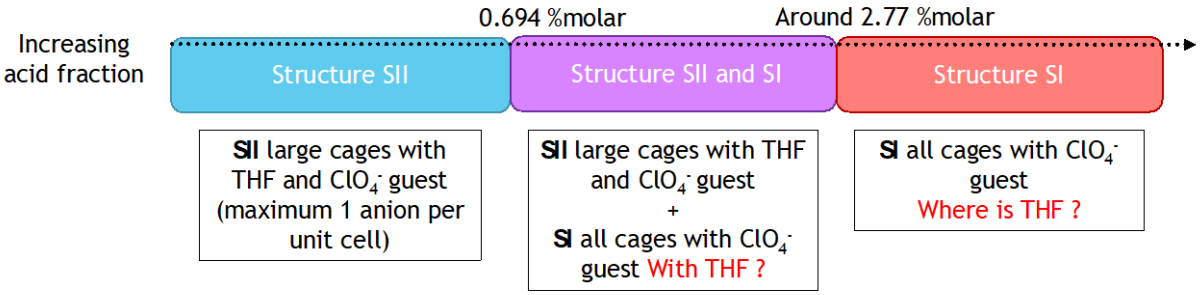

Figure IV. 19. Sketch of the structure identification by XRD depending on the acid fraction in mixed hydrate sample of THF-$HClO_4$ at 170 K.

The study of the evolution of the XRD peaks intensities highlighted the influence of the acid molecules on the structural stability of hydrate.

For the SI hydrate structure, the melting temperature found is different from the pure $HClO_4$ hydrate. The encapsulation of THF with $HClO_4$ in the SI structure might cause it destabilisation and caused it to melt at a lower temperature. With this study, the possible co-inclusion of THF and $HClO_4$ in the SI hydrate structure is brought up. The localisation of THF molecules in the mixed hydrate when the SII structure is not formed needs to be investigated further. In Figure IV. 19, the guest composition of the hydrate structures is presented with the unknown regarding the localisation of the THF.

The melting temperature of the Ice in the samples is lower than 273 K (melting T for pure ice) and indicates the disruptive effect of the acid molecules on the structure. The effect is particularly observed for samples in domain 2 and 3, where the SI hydrate melt around 200 K and the acid molecules from the SI hydrate is mixed with the ice.

The structural findings of the mixed hydrate by XRD experiments are applied to the impedance measurements to interpret the conductivity values. We will look at how the acid concentration and also structure domains influence the protonic conductivity of the mixed hydrate. In order to localise the structures and their distribution within the sample, Raman imaging spectroscopy is performed on the samples' surfaces. The distribution of the structure in the sample give insight on their influence on the protonic conductivity. Combining the techniques highlight the parameters in the hydrate samples influencing the conductivity.

Chapter V. Protonic conductivity in the mixed hydrate THF-$HClO_4$

Table of contents

A. Introduction

To determine the influence of acid concentration on the protonic conductivity of ionic hydrates at various temperatures, impedance measurements were performed on mixed hydrate with THF and $HClO_4$.

In Chapter IV, the hydrate of THF and $HClO_4$ has been studied by X-Ray Diffraction. The thermal stabilities of the SII and SI hydrate structures, depending on the acid concentration, are combined in Figure IV.18. Depending on the acid concentration in the mixed hydrate samples, three domains with hydrate structure were identified: one with only the SII structure, a second with a mixed of the SII and SI structure and a third with only the SI structure.

Now that we have a complete picture of the sample studied, we want to know their protonic conductivity and linked it to the acid fraction and hydrate structure to understand their influence.

We start by questioning ourselves on the different models possible for protonic conductivity. Then we looked at the Raman spectroscopy study to answer question on the sample overall structure. Then we apply various model depending on the samples structure to associate the model to the conductivity data.

B. Conductivity models

Before showing the impedance measurements, done on the mixed hydrate samples, models of the protonic conductivity are presented. The model considers a porous system with a 3D diffusion process which correspond to hydrate systems.

1. Nernst-Einstein: Model A

The Nernst-Einstein law is a law that is involved in the migration of species in crystalline solids when the species are subjected to a force; by "species", we mean "crystal defects".

The conductivity σ depends on the concentration c and the mobility of the charge carriers expressed by the diffusion coefficient D, as well as on the temperature T according to the following Nernst-Einstein equation:

$$\sigma(c,T) = \frac{D.c.e^2}{k.T} \qquad [48.V]$$

One type of porous material is considered for this equation.

From the Nernst-Einstein equation, the conductivity depends on the concentration c and the temperature T. The influence of these two parameters is the focus of this study. They will be treated separately. First, we look at the temperature effect on the conductivity and, then, the concentration influence. Presented next is the expected relation evolution between the parameters and the conductivity.

- Conductivity as a function of the temperature at fixed concentration: $\sigma = f(T)$

The diffusion coefficient can be described by the Arrhenius law as depending on the temperature:

$$D = D_0.e^{-\frac{E_A}{kT}} \qquad [49.V]$$

Combining the Arrhenius law with the Nernst-Einstein equation, we obtain

$$\sigma = D_0.c.e^2.\frac{e^{-\frac{E_A}{kT}}}{kT} \qquad [50.V]$$

From the chosen model with the Nerst-Einstein equation, the conductivity is expected to increase with the temperature. The increase is linear when the graphic representation shows the conductivity times the temperature in the log scale with respect to the inverse of the temperature in K^{-1} (see Figure V. 1. Left). The slope of the linear fit is the activation energy E_A of the material conductivity.

- Conductivity σ as a function of the concentration c at a fixed temperature.

The Nernst-Einstein law gives the conductivity relation with the concentration for a constant temperature *T* and the diffusion coefficient *D (fixed by the porous material consider)*:

$$\sigma(c) = \frac{De^2}{kT}.c \qquad [51.V]$$

The conductivity will increase linearly proportionally to the concentration with $\sigma(c) = 0 \; for \; c = 0$ (see Figure V. 1. Right).

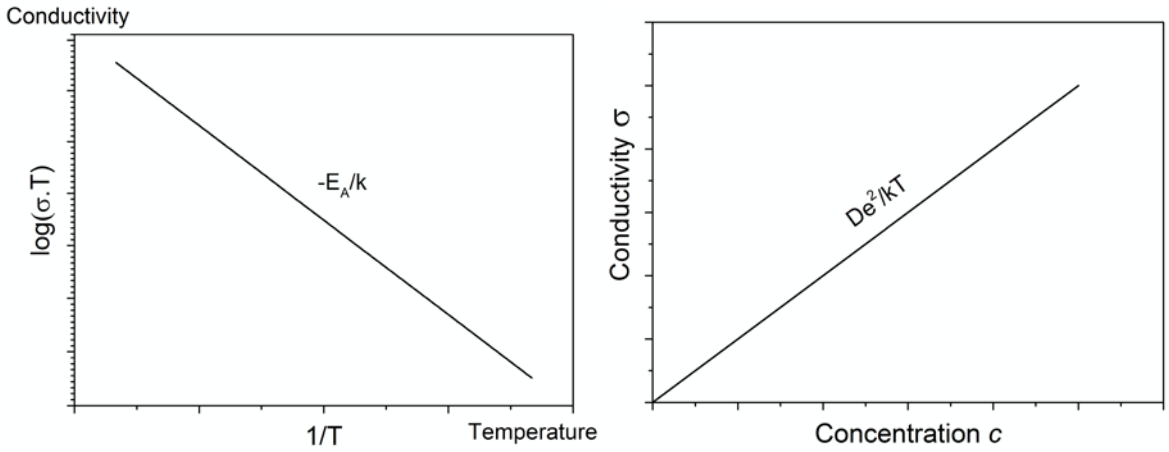

Figure V. 1. Left. Evolution of the conductivity with respect to the temperature at fixed concentration. Right Evolution of the conductivity with respect to the concentration at fixed temperature according to the Nernst-Einstein law.

2. Solution solid model

The Nernst-Einstein model which considers only one type of structure, is too simple to describe all the mixed hydrate samples.

For the DRX study, the mixed hydrate samples can have up to three types of solid: SII and SI hydrate structure as well as hexagonal ice, noted I_h (see Chapter IV) Figure V. 2.

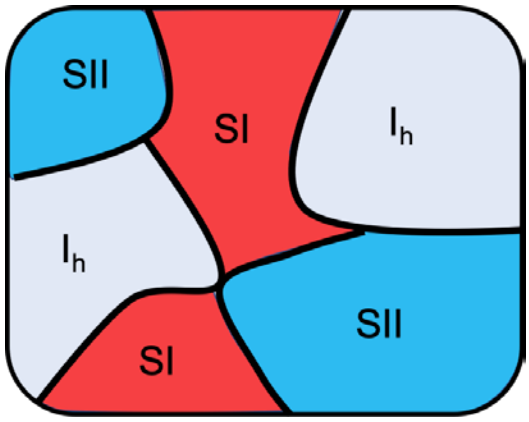

Figure V. 2. illustration solution solid: mixed hydrate structure and Ice.

The next conductivity model is the Perfect Solution Solid Model [REF!]. For this model, the conductivity total of the sample is the sum of the conductivity of each solid present in the sample with their respective quantity.

Model solution solid with three solids:

$$\sigma(c,T) = \Delta_{SII}(c).\sigma_{SII}(\mathrm{T}) + \Delta_{SI}(c).\sigma_{SI}(\mathrm{T}) + \Delta_{Ih}(c).\sigma_{Ih}(T) \qquad [52.V]$$

The ice conductivity is negligible compared to the hydrate conductivity. In this model, the interface contribution is neglected to simplify the model.

The SII hydrate conductivity $\boldsymbol{\sigma_{SII}}$ **and** SI hydrate conductivity $\boldsymbol{\sigma_{SI}}$ and their respective quantity in fraction Δ in the hydrate sample **are** considered. The fraction is calculated with the ratio of Guest-H_2O needed to form each ideal structure and the sample concentration. SII Ideal structure is formed with their 8 big cages filled with THF except for one big cage filled with $HClO_4$ (sample Acid fraction = 0,694 %mol).

The ideal SI structure is considered with all cages (6 big + 2 small) filled with $HClO_4$ corresponding to the $HClO_4$-5,5H_2O hydrate [MOO 87]. The ice is formed from the H_2O molecules not participating in the ideal hydrate structure. The sum of fraction of each system (SII hydrate Δ_{SII}, SI hydrate Δ_{SI} and ice Δ_{Ih}) is equal to 1 ($\Delta_{SII} + \Delta_{SI} + \Delta_{Ih} = \mathbf{1}$**).**

- Conductivity with respect to the temperature at fixed concentration: $\sigma = f(T)$

$$\sigma(T) = \Delta_{SII}.\sigma_{SII}(\mathrm{T}) + \Delta_{SI}.\sigma_{SI}(\mathrm{T}) \qquad [53.V]$$

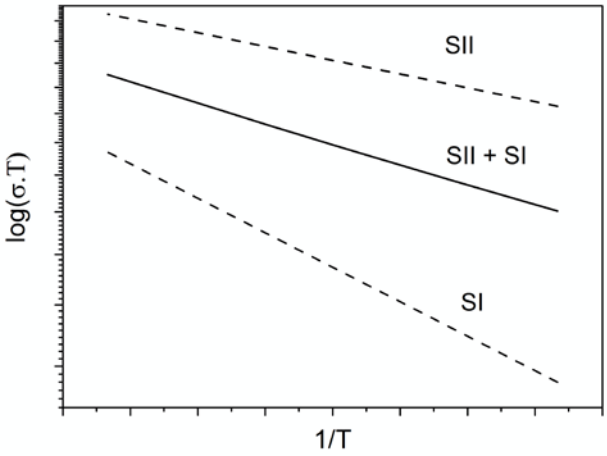

Figure V. 3. Expected figure for the study of the conductivity with respect to the temperature in the solution solid model.

- Conductivity σ as a function of the concentration c at a fixed temperature

$$\sigma(c) = \Delta_{SII}(c).\sigma_{SII} + \Delta_{SI}(c).\sigma_{SI}\ [+\Delta_{Ih}(c).\sigma_{Ih}] \qquad [54.V]$$

From the XRD study we have identify three different structure presence in the sample depending on the acid fraction, called domain, in this work. In Figure V. 4, we show the expected conductivity evolution with respect to the concentration and with the three structural domains.

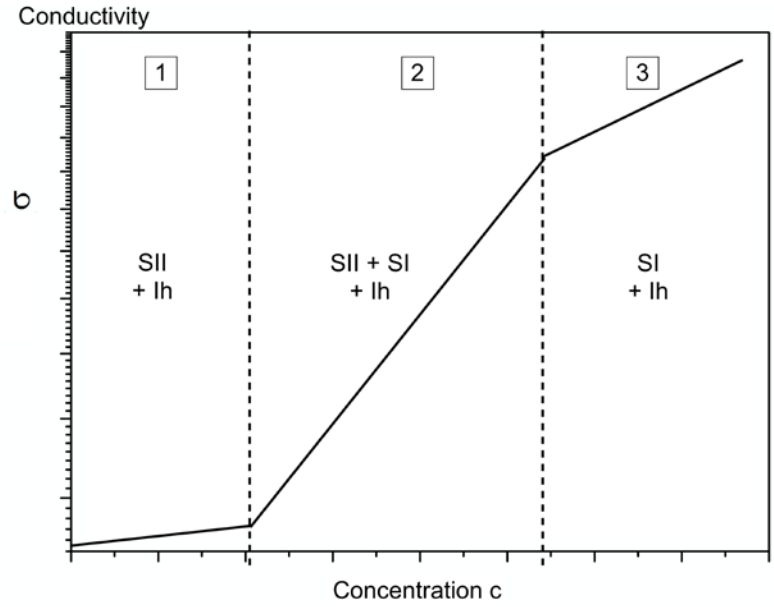

Figure V. 4. Expected figure for the study of the conductivity evolution with respect to the concentration in the solution solid model

In domain 1, SI hydrate structure is not formed. The fraction of SI hydrate structure is zero, noted $\Delta_{SI} = 0$. The sample in domain 1 are composed of SII hydrate structure and ice. The ice conductivity is negligible compare to the conductivity of the mixed hydrate. This case corresponds to the Nernst-Einstein model introduce earlier with one type of material.

Therefore, the conductivity of the samples from domain 1 are expected to follow a linear evolution with the concentration

$$\sigma_{SII} = b_{SII}C + a_{SII} \; ; \; a_{SII} = 0$$

Similar reasoning for samples from the domains 3. In domain 3, SII hydrate structure is not formed (XRD data, see Chapter IV). The fraction of SII structure is zero, noted $\Delta_{SII} = 0$. The conductivity of the SI hydrate structure is expected to be acid concentration dependent. $\sigma_{SI} = f(c)$.

Domain 2, where the SI and SII structure were identified by XRD in Chapter IV) presents the most challenging aspect of the mixed hydrate. The fraction of each structure needs to be

considered as well as their evolution with the acid concentration. Two cases are possible:

Model 2.1: the fraction of each structure is constant ${}^{\Delta_{SI}}/_{\Delta_{SII}} = constante$, i.e. not linked to the concentration

Model 2.2: The fraction of SI and SII hydrate structure formed in the sample is not constant and change with the acid fractions: ${}^{\Delta_{SI}}/_{\Delta_{SII}} = f(c)$, i.e. change with the concentration

From the XRD, we know the faction of each structure depend on the acid concentration, we are then in the case Model 2.2. But to have a complete study and confirmed the observation of the XRD, the two model will be considered when we apply them to the conductivity data, later on.

3. Solution solid model and interface.

The problematic of the interface in protonics conductors is source of many studies. For the case of solid protonic conductor, the effect of the solid-solid interfaces plays a crutial part in the systems performance [CHI 20]. In the case of the hydrate structure the influence of interfaces has been noted for the super-diffusion of the methane in hydrate structure [RAN 21]. The nature of the interfaces is of particular interest for water system [BAC 21]. They destabilized or stabilized a system. In the case of ionic hydrate the layer nature and structuration is influencing the protonic conductivity [DES 18].

To implement the previous model, the interface between the various structure is considered (see Figure V. 5). The interface contribution is noted as $\Delta_{\boldsymbol{int}}$. The conductivity of the interface $\boldsymbol{\sigma_{int}}$ has to be considered.

$$\sigma(c,T) = \Delta_{SII}(c).\sigma_{SII}(\mathrm{T}) + \Delta_{SI}(c).\sigma_{SI}(\mathrm{T}) + \Delta_{Ih}(c).\sigma_{Ih}(T) + \Delta_{int}(c).\sigma_{int}(T) \qquad [55.V]$$

The conductivity of the ice σ_{Ih} is considered negligable compare to the hydrate conductivity

and the interface contribution.

The used of the previous model apply to the conductivity data will allowed to determine the conductivity of the SII hydrate structure (for the sample where only SII hydrate is formed) and the conductivity of the SI hydrate structure.

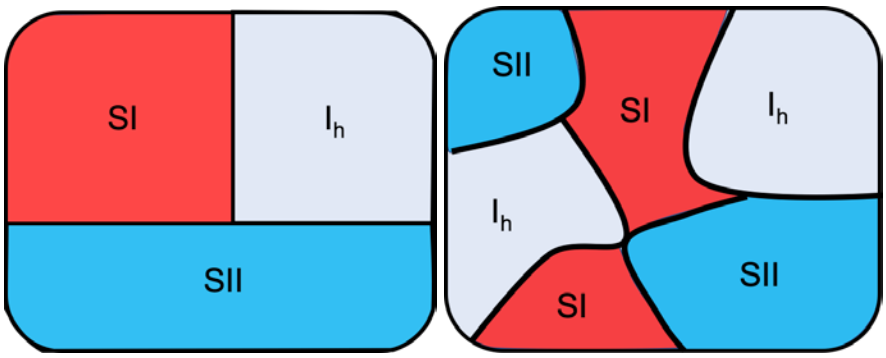

Figure V. 5. Sketch of possible arrangement of the hydrate structure and Ice in mixed hydrate sample.

The interface Δ_{int} can be described by the surface area of hydrate structure. Depending on the arrangement of the different structure in the samples, the interface will not be the same.

If we consider the different structure as grain, the surface area can be described as:

$$A_S = 4\pi R^2 \qquad [56.V]$$

where A is the surface area of the hydrate if round grains are considered and R is the radius of the hydrate grain.

If the surface interface is considered as a monolayer of H_2O molecules, we obtain:

$$N_{H2O}^{S} = \frac{A_S}{A_{H20}} = \frac{4\pi R^2}{A_{H20}} \qquad [57.V]$$

where A_S surface area of hydrate and A_{H20} water molecule area.

The size of hydrate aggregates defines the hydrate surface, creating the interface influencing

the conductivity. The hydrate structural arrangement inside the samples is needed. The rayon of hydrate aggregate R = $R_{SI} = R_{SII}$ is not known.

$$\Delta_S = \frac{4\pi R^2}{A_{H20}} \times \frac{1}{N_{H20}} \qquad [58.V]$$

The surface coverage may add a limit value to the extra water quantity to have an effect on the conductivity. Surface coverage: $\sigma_{int} = \mathrm{f(c)}$. If the surface coverage is inferior to 100% of the hydrate structure, then they have no effect on the conductivity $\sigma_S \sim 0$ but if the surface coverage equal ~100 %, the conductivity is $\sigma_{int} \neq 0$.

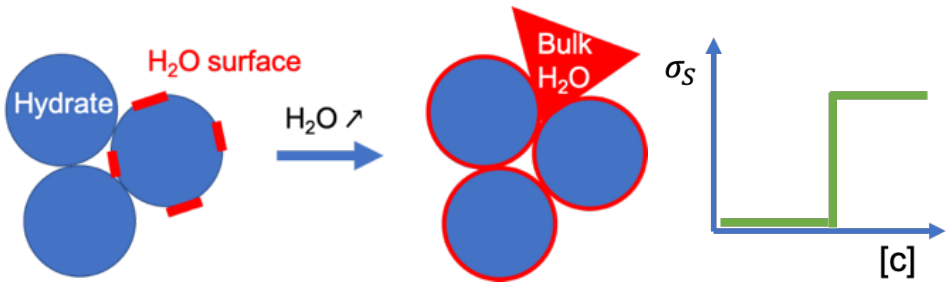

Figure V. 6. Left. Scheme of hydrate aggregate and water surface considering the water coverage. Right. Hypothesis of the effect on the conductivity of the surface water concentration.

Raman imaging at the micro scale is performed on the samples to bring some answers on the samples homogeneity. The spatial resolution of the Raman imaging (Chapter II) allows to scan the samples' surface and determined the size of the hydrate aggregates in the order of micro-scale ($R > \mu m$).

C. Distribution of the different structures in THF-$HClO_4$ mixed hydrate– Raman

After the X-Ray diffraction analysis of the mixed hydrates as a function of the acid fractions, we are interested in the spatial distribution of the various structure in the sample. As

expressed in the different models, the homogeneity, or the lack of it, of the samples determined.

1. Species Identification

Raman spectra have been performed on the clathrate hydrate of THF and on the perchloric acid hydrate. Band identification and stability temperature are done on the hydrate samples of THF-17H_2O forming the SII structure and hydrate of $HClO_4$-5.5H_2O forming the SI structure. These studies allow the establishment of relevant information for the investigation of the mixed clathrate hydrate where THF and $HClO_4$ are both guest molecules.

i. Raman signature of the THF hydrate and THF liquid

THF hydrate formed the structure type SII with unit-cell composed of 16 cages 5^{12} and 8 cages 5^{12} 6^4. Only the 8 big cages are full of THF guests. Raman spectroscopy is done on pure liquid THF and on THF-17H_2O hydrate samples at 170 K (solid form) and at 290 K (liquid form). Comparing the different spectra allowed the identification of relevant THF peaks and hydrate peaks. THF spectra are shown in Figure V. 7. The most prominent modes in pure THF are at 914 cm^{-1}, 1030 cm^{-1} and 2870 to 2960 cm^{-1}. The stronger modes at 914 cm^{-1} and 2870-2960 cm^{-1} are assigned to a ring breathing mode and an anti-symmetrical stretching mode of the CH_2 groups, respectively. The band centred at 914 cm^{-1} for the pure substance degenerated and split into two bands centred at 892 cm^{-1} and 918 cm^{-1} for the liquid THF, which can be attributed to the interactions between THF and water molecules. [PRA 07]. For THF hydrate, the 914 cm^{-1} band shifted to 920 cm^{-1} without splitting, because the highly-ordered cage of water molecules prevents the interactions that occur in the liquid phase. At 920 cm^{-1} the ring-breathing mode observed is characteristic of the encapsulated THF molecule. Split of the 920 cm^{-1} peak of the hydrate form in 890 cm^{-1} and 922 cm^{-1} for an aqueous mixture of THF.

The Raman bands centred at ~3200 and ~3400 cm^{-1} represent hydrogen-bonded water molecules. Both of the protons of these water molecules are involved in hydrogen bonding, and both of the lone electron pairs are also involved in hydrogen bonding. The spectrum at

~3200 cm^{-1} represents the vibrations of strongly hydrogen-bonded OH-groups, which indicates an ordered arrangement of water molecules; specifically, the band centred at ~3200 cm^{-1} is attributed to the OH mode of tetrahedrally-coordinated hydrogen-bonded water, which is normally the most intense band in the spectrum of ice. The spectrum at ~3400 cm^{-1} represents more weakly hydrogen-bonded OH-groups for water molecules in incomplete tetrahedral coordination (i.e. slightly disordered) hydrogen-bonded structure. This band at 3200 cm^{-1} is often referred to as the "ice-like" mode, whereas the band at 3400 cm^{-1} is referred to as the "liquid-like" mode.

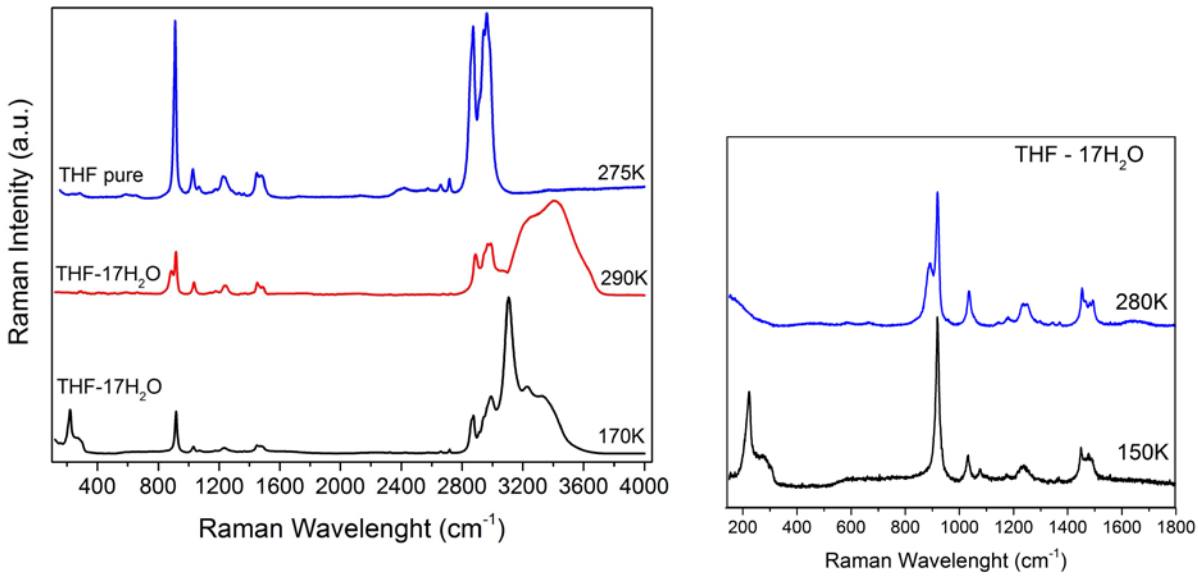

Figure V. 7:Raman spectrum of pure liquid THF at 275 K (blue) and hydrate THF-17H_2O at 290 K (red) and at 170 K (black), Zoom on the 200-1600 cm^{-1} region of hydrate THF-17H_2O spectrum.

ii. $HClO_4$ hydrate and liquid form

The perchloric acid hydrates formed a hydrate structure type SI, with unit cell composed of 2 cages 5^{12} and 6 cages 5^{12} 6^2. All the water cages are occupied by the perchlorate anion. The guest molecules of $HClO_4^-$ interact with the water molecules forming the cages. The interaction in the crystal structure lead to a modification of the intra and inter molecular bonds. Studies have also determined the melting temperature of hydrate $HClO_4$-5.5 H_2O at T_m = 228K [MOO 87].

In order to differentiate the crystalline phase and the liquid phase of the hydrate, a comparison of the Raman spectra on the well know hydrate $HClO_4$-5.5 H_2O at 170 K and 300 K is shown Figure V. 8. The identification of the characteristic vibration modes of $HClO_4$ in liquid state and hydrate state is made. First, easily identifiable are the three peaks attributed to the guest $HClO_4$. The totally symmetric stretching mode of the perchlorate anion is observed at 934 cm^{-1}.The relevant signature of the perchlorate anions is associated with the mode υ_2 at 460.6 cm^{-1} and the mode $\upsilon_4$at 627 cm^{-1}. The peak at 1100 cm^{-1} of $HClO_4$ at 300 K is separated into two peaks at 170 K. The split of the peak at 1100 cm^{-1} is proof of encapsulated $HClO_4$ species and, thus, of hydrate formation. Know melting temperature is 228 K. The water molecule lattice mode around 200 cm^{-1} and the shape of the Raman bands of O-H stretching from 3000 cm^{-1} to 3500 cm^{-1} are also evidence of the hydrate's shape of hydrogen-bonded water molecules. Due to the low signal of the water and lattice hydrate structure, the identification of $HClO_4$ hydrate formation is made by following the split of the peak at 1110 cm^{-1}.

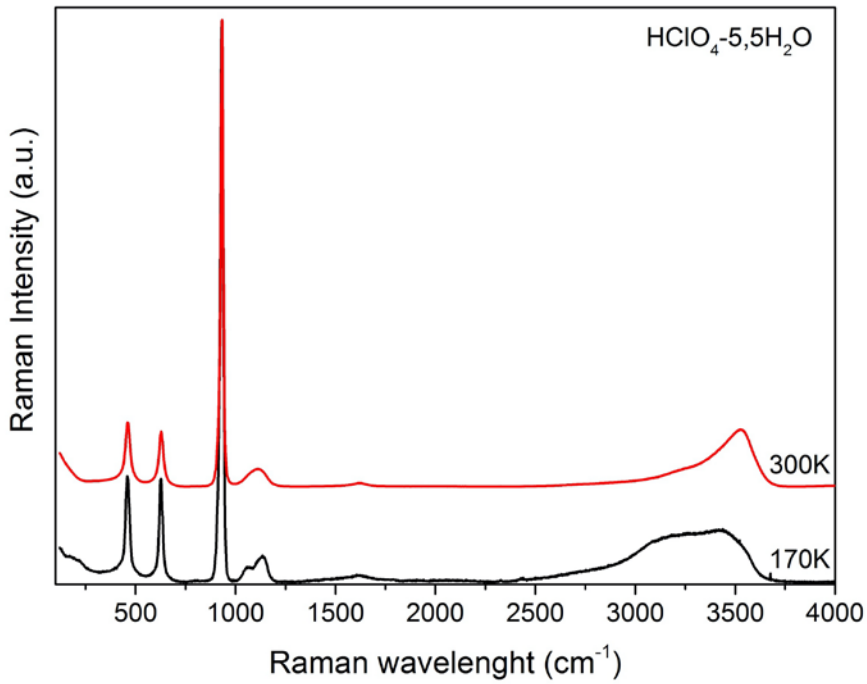

Figure V. 8. Raman spectra (λ = 532 nm) of $HClO_4$ -5,5H_2O at 170 K(black) and 300 K(red). Peaks Identification noted for $HClO_4$ species by full circle, for $HClO_4$ encapsulated by full start and for H_2O in hydrate structure by empty start.

The study of the compound in pur liquid and hydrate form is essential for further study.

Knowing the Raman signals of each species as the melting temperature of the hydrate, depending on the structure formed, will guide the study of the mixed samples.

2. Mixed hydrate - Imaging Raman spectroscopy

i. Mixed THF-HClO4 hydrates

After the study of the THF and $HClO_4$ Raman signatures in their respective pure hydrate structure, we noticed the possible overlapping of the Raman signatures that will make the identification of the mixed hydrate challenging. The characteristic for $HClO_4$ hydrate at 1100 cm^{-1} is overlapping with the signals from THF molecules. The water stretching between 3100 and 3600 cm^{-1} characteristics of $HClO_4$ hydrate is also overlapping with the one from the THF hydrate (see Figure V. 9). The XRD study revealed the presence of ice in the mixed hydrate samples (see Chapter IV) and the ice peaks in Raman spectroscopy is as well overlapping with the hydrate signals from the hydrate structures.

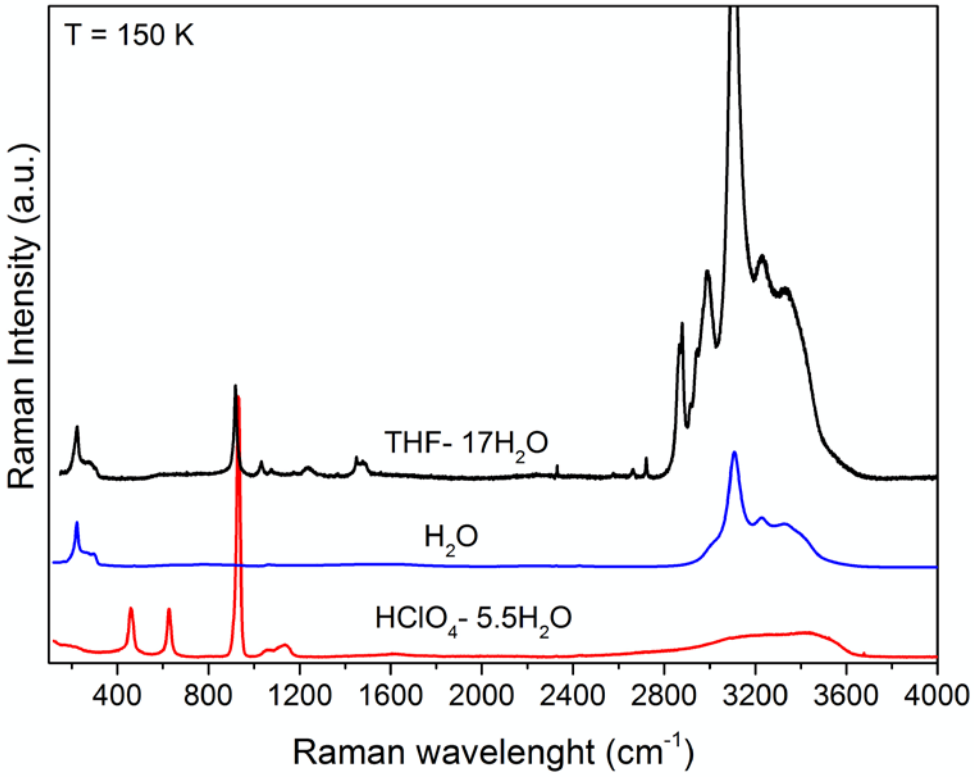

Figure V. 9. Comparison of the Raman spectra of THF hydrate (Black), Ice (blue) and $HClO_4$ hydrate (red).

A comparative study is done on the samples where Raman spectra are recorded at two positions on the sample surface and then compare with each other. The sample of the mixed THF-$HClO_4$ hydrate with acid fraction at 2.778 %mol, corresponding to the chemical formula 0.5 THF – 0.5 $HClO_4$ – 17 H_2O is studied (see Figure V. 10).

From the Raman spectrum of this mixed hydrate sample at 150 K, some peaks are clearly identifiable. The THF modes at 920 cm^{-1} and around 2870-2960 cm^{-1} are assigned to the ring breathing mode, and the anti-symmetric stretching mode of the CH_2 groups, respectively. The totally symmetric stretching mode of the perchlorate anion is observed at 934 cm^{-1}. The relevant signatures of the perchlorate anions are associated with the mode v_2 at 460.6 cm^{-1} and the mode v_4 at 627 cm^{-1}. Complicating the hydrate structure identification are the O-H lattice modes around 200 cm^{-1} and the O-H stretching mode in the region 3200-3600 cm^{-1}, where the hydrate and ice signal can't be differentiated from one another.

From the sample with high acid fraction at 2.77 %mol, we compare two spectra taken at the surface of the mixed hydrate at a distance of 30 μm from each other. The acid peaks intensity at 460.6 cm^{-1} and at 627 cm^{-1} show different intensities as well as the peaks at 2870-2960 cm^{-1} from the THF species. The intensity change is linked to a quantity difference on the sample surface, confirming the heterogeneous mixed of the hydrate sample.

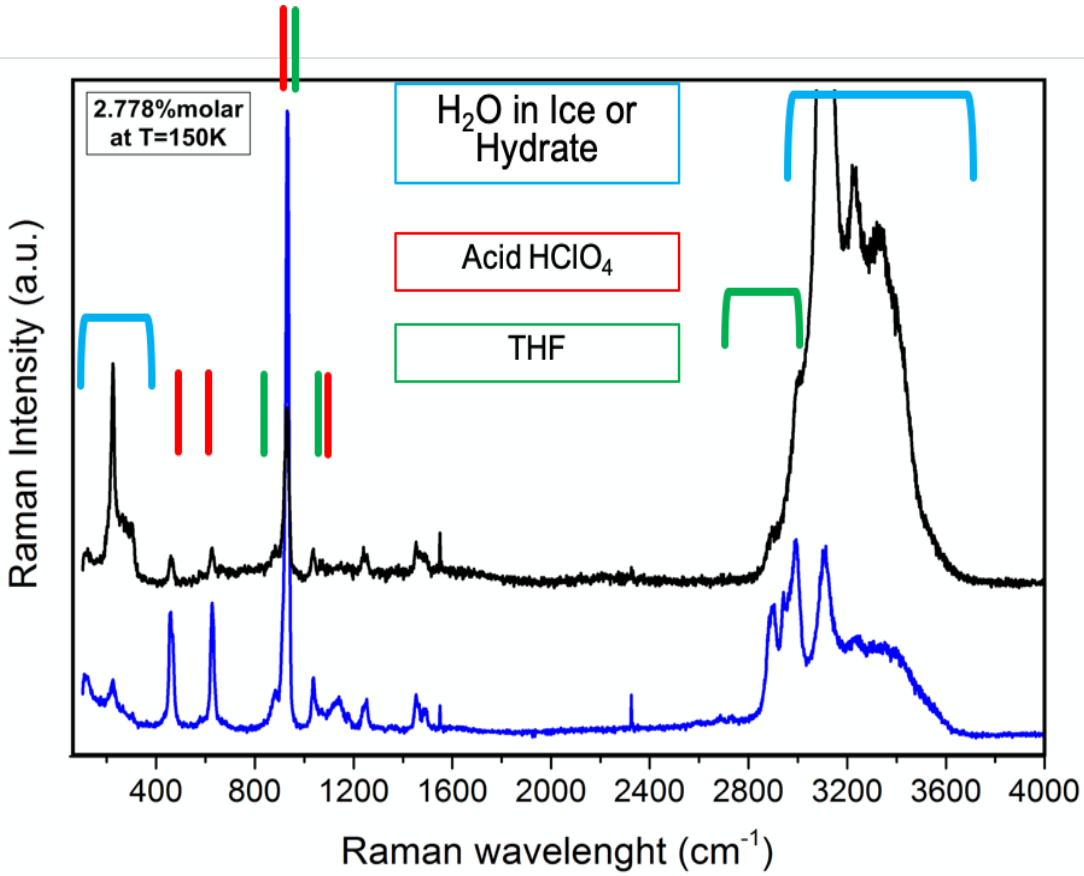

Figure V. 10. Raman spectra of mixed hydrate with acid fraction at 2.77 %mol at 150 K done at two different coordinates on the surface sample.

The overlapping area at 1060 cm^{-1} of the $HClO_4$ and THF peaks doesn't allow the identification of the encapsulation of $HClO_4$ in the SI hydrate structure characterised by the splitting of the peaks at 1110 cm^{-1}.

The peak identifications are not conclusive in mixed samples to localise and differentiate the SI hydrate structure from the SII structure. The peaks proving the formation of the SII or SI structure are overlapping with other peaks making the determination of the formed structure complicated. Different options are available to resolve this issue. Knowing that the SI hydrate structure formed with acid guest $HClO_4$ and the SII hydrate structure with THF molecules, the signature peaks of the guest species will give indications of their localization at the micro-scale.

Hydrate samples with various acid fraction were scanned in the surface along the x y plane

over areas of around 50 x 40 μm^2 with 5 μm step (size of the scan depend on the visual shape of the hydrate surface). The scans are made to obtain a “picture” of the sample and to study the peak variation on the surface. Cartography made on the surface shows heterogeneous samples. From the X-Ray Diffraction pattern, we know the different structures expected to be formed in the samples.

ii. Principle Component Analysis technic

The Principle Component Analysis (PCA) is a chemometric study [BEA 21]. The PCA used reference Raman spectra to identify, by comparison, compounds in a given sample.

The PCA techniques compare reference spectra, given previously, to the sample and estimate the weight of the reference spectra in the sample spectrum. While the follow of peak intensity will show a precise localisation of the species in the sample, the PCA study gives us a chance to localized and quantify the hydrate structure on the sample surface. The accuracy of the technics is also greater by considering the full reference spectra and not only some isolated peaks.

Reference Raman spectra are taken for each pure compound expected in the studied sample. Identified by X-ray diffraction, the THF hydrate, the $HClO_4$ hydrate, and ice are expected in this case. Their respective Raman spectra, studied in the previous part, are selected as references for the PCA study. All the experiments were done in the same experimental set-ups (see Chapter II).

The resulting image obtains shows the coefficient of each reference spectra (three in total) that compose the sample spectrum from the Raman cartography. Identifying areas of the different compounds on the surface of our mixed hydrate samples is now possible.

iii. PCA apply to Raman imaging of mixed hydrate

The Raman imaging has performed to complete the observation made from the XRD experiments (see Chapter III) and to study the distribution of the various structure in the sample in similar experimental conditions as for the conductivity measurement (as explained in Chapter II).

PCA is applied for each sample, but only one sample from each structural domain will be presented here. In Figure V. 11, Figure V. 12 and Figure V. 13, graph (a) will show the optical microscopic image of the sample surface made by the microscope coupled with the Raman spectroscopy (presented in Chapter II). Graphs (b), (c), and (d) show the presence in weight percentage of the reference Raman spectra in the mixed sample. The reference spectra of ice (H_20 at 150 K), $HClO_4$ hydrate and THF hydrate samples are shown in Figure V. 9. The percentage scale is the same for the three graphs in the PCA study.

The mixed hydrate at 0.521 %mol acid, which is a sample from domain 1 where the SII hydrate structure and ice are formed, is studied first. In Figure V. 11. (a), the optical microscopic image shows the sample surface studied. The three other images noted in Figure V. 11. (b), (c) and (d) represent the three reference spectra weight percent, respectively, for the ice, THF hydrate and $HClO_4$ hydrate, in the spectra done at the corresponding x y position.

From the reference %weight map, various areas in the sample can be identify. At the y position from -10 to -25 μm and x position from -30 to -10 μm, the ice weight% is over 90 weight% (dark red) and the $HClO_4$ and THF map show a weight percent lower than 12 weight% (purple and black) at that same position. These observations indicate the presence of ice. By opposition, areas with lower to none ice is identify at the top right corner across the sample (black to purple areas). At the same position, the %weight of the $HClO_4$ hydrate reference is the highest, from 30 %weight to 60 %weight, and the THF hydrate is at 60 to 80 %weight. This weight percentage corresponds to the formation of SII hydrate structure with THF guests and fews $HClO_4$ guests.

In other areas where the ice weight% is lower, the THF and $HClO_4$ hydrate weight% is higher. This data evidence a mix of the SII hydrate structure with THF and $HClO_4$ guests and ice structure, with a grain size lower than a micrometre (which is the resolution of the Raman

spectrometer, as seen in Chapter II).

At the area where H_2O is between 60 to 80 %weight, $HClO_4$ hydrate %weight is under 6 % weight, and THF hydrate is at 20 and 30 %weight. From the percentage, the hypothesis can be that SII THF hydrate is formed without $HClO_4$ guest and mixed with ice in these areas.

All the results support the observation of the heterogeneity of the samples, even at low acid concentrations, at the microscopic scale.

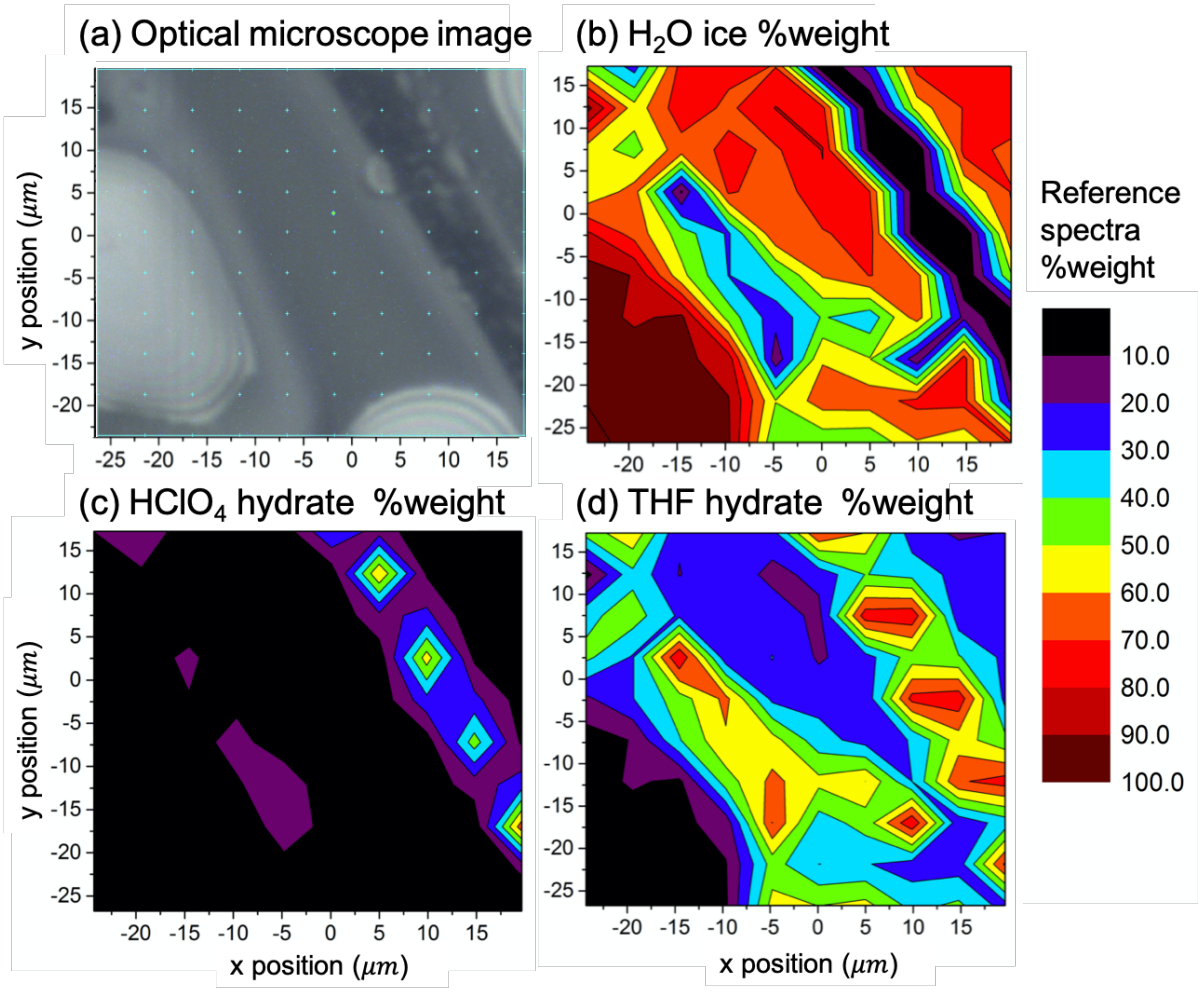

Figure V. 11. PCA map of mixed hydrate at 0.521 %mol acid fraction.

The PCA method is applied on the mixed hydrate sample with medium acid fraction at 1.85 %mol; The resulting three maps are shown in Figure V. 12. In this sample, the SII and SI

hydrate, as well as the ice, are expected to be present from the XRD experiments presented in Chapter IV.

Graph (b) in Figure V. 12 shows the weight of the ice reference spectra in the cartography of the mixed hydrate surface. The black and purple areas correspond to a percentage inferior to 20 %weight. The blue, green and orange areas are for a percentage between 25 %weight to 65 %weight. Figure V. 12 (c) show the percentage weight of the spectra of pur $HClO_4$ hydrate in SI structure in the sample spectra in the cartography. Figure V. 12 (d) show the percentage weight of the spectra of THF hydrate in SII structure.

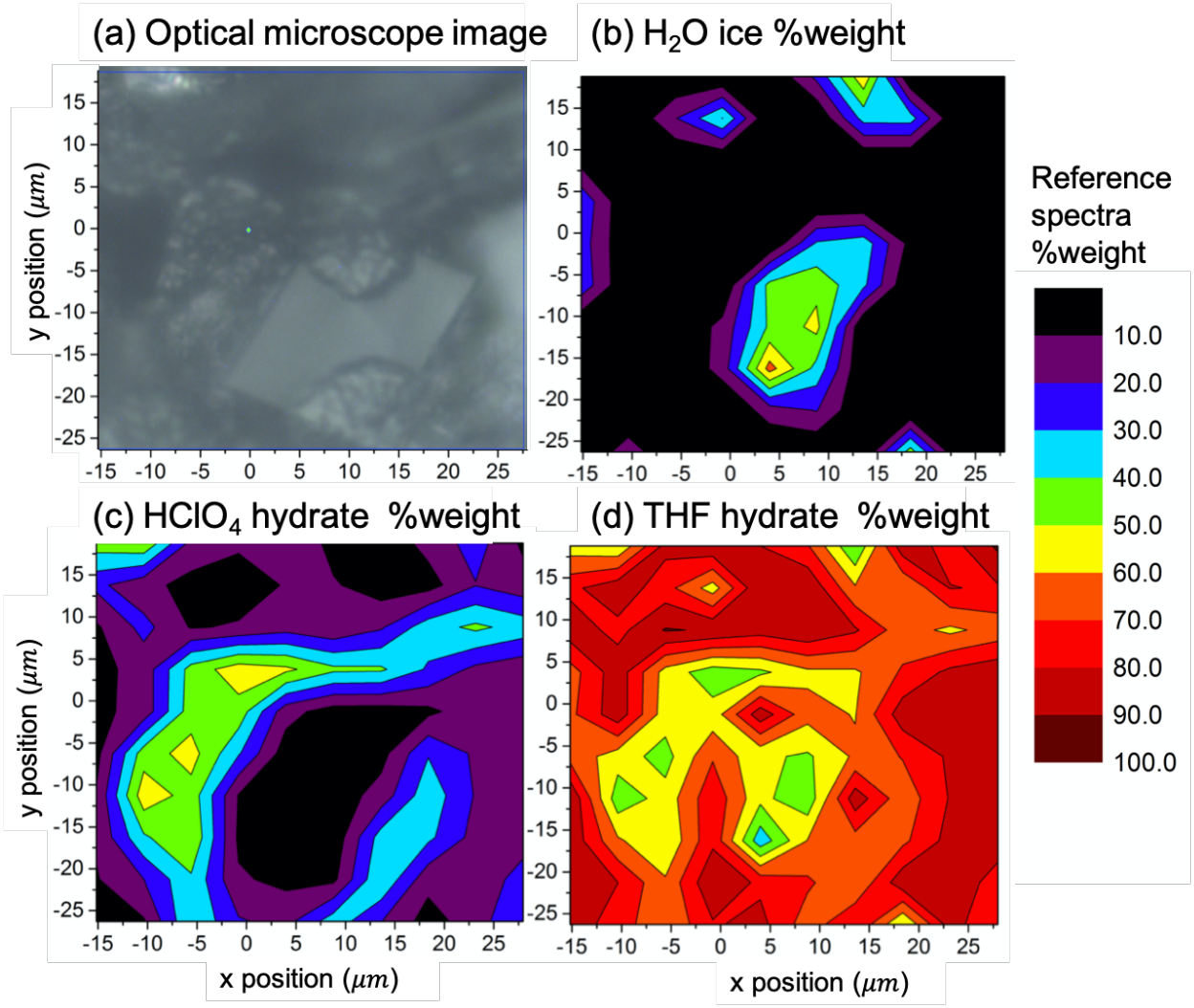

Figure V. 12. PCA study of mixed hydrate at 1.85 %mol acid fraction.

Finally, the sample at 4.629 %mol is studied. This sample belongs to the third domain, where SI hydrate structure is formed with ice. Figure V. 13

The overall percentage of THF is lower than 30 %weight. Graph (a) of H_2O weight% and (b) of HClO4 hydrate weight% are the opposite image of each other. For example, at the position x = 15 and y = 5 μm, H_2O weight% is over 80 weight%, and the $HClO_4$ is lower than 20 weight%. It confirmed the presence of ice and SI hydrate structure formed with $HClO_4$ guest. More importantly, it indicates that the sample forms grain of ice and hydrates at the micro-scale.

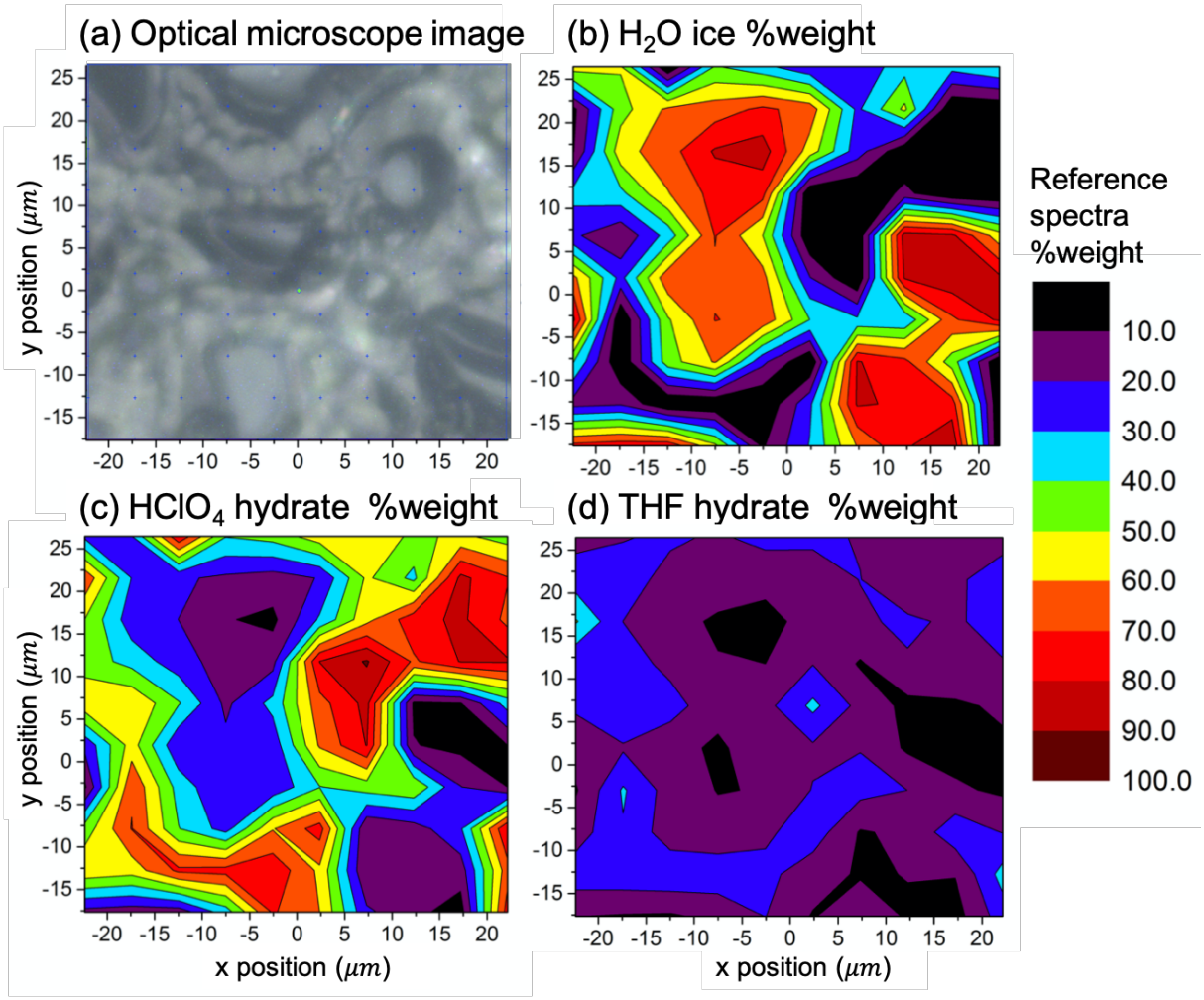

Figure V. 13. PCA study of mixed hydrate at 4.629 %mol acid fraction.

3. Conclusion Raman

Peak identification = overlapping of the characteristic peaks of hydrate.

Visual Observation made by the optical microscope on the various samples' surfaces shows heterogeneous samples. It was confirmed by taking Raman spectra at various locations on the surface. The global picture of the heterogeneous sample is constructed from multiple spectra done at the surface for a given x y plane with μm step, resulting in a map of the sample's surface.

Principle Component Analysis (PCA) study shows from the domain previously identified by the peaks intensity where only identify the presence of THF and HClO4 are actually more complex. When we consider the THF and $HClO_4$ hydrate full spectra and compare them with the percentage ratio, new areas appear. The different hydrate structures inside the mixed samples create a new interface structure.

D. Model Application to the conductivity measurements

The impedance measurements are obtained for different temperatures for the hydrate samples of THF-$17H_2O$, $HClO_4$-$5{,}5H_2O$ and the mixed hydrate samples of THF and $HClO_4$ with various acid fractions from 0.069 %mol. to 4.628 %mol.

Impedance measurements are recorded for temperatures from 150 K to the melting temperature of the sample using 10 K steps or 20 K steps (details in Chapter II).

The conductivity results are presented with the model application presented in part B of this Chapter V.

1. Conductivity of the pure hydrate systems

i. THF hydrate conductivity study

Impedance measurements are done on the hydrate sample of THF - $17H_2O$ at various temperatures. The conductivity times the temperature in the log scale with respect to the

inverse of the temperature is shown in Figure V. 14 . The data doesn't allow us to apply the Arrhenius law (detailed in Part B on the conductivity model). There is no linear relation between protonic conductivity and temperature for THF hydrate. The protonic conductivity values obtained are between 1.10^{-4} S.cm^{-1} and 3.10^{-4} S.cm^{-1}. These values are quite low and at the detection limit of the impedance set-up.

Impedance measurements are also performed on H_2O samples as a reference. The results obtained are in the same order as for THF hydrate. Protonic conductivity data for the ice sample is shown in Figure V. 14 (grey, triangle). Again, no linear relation is found between protonic conductivity and temperature.

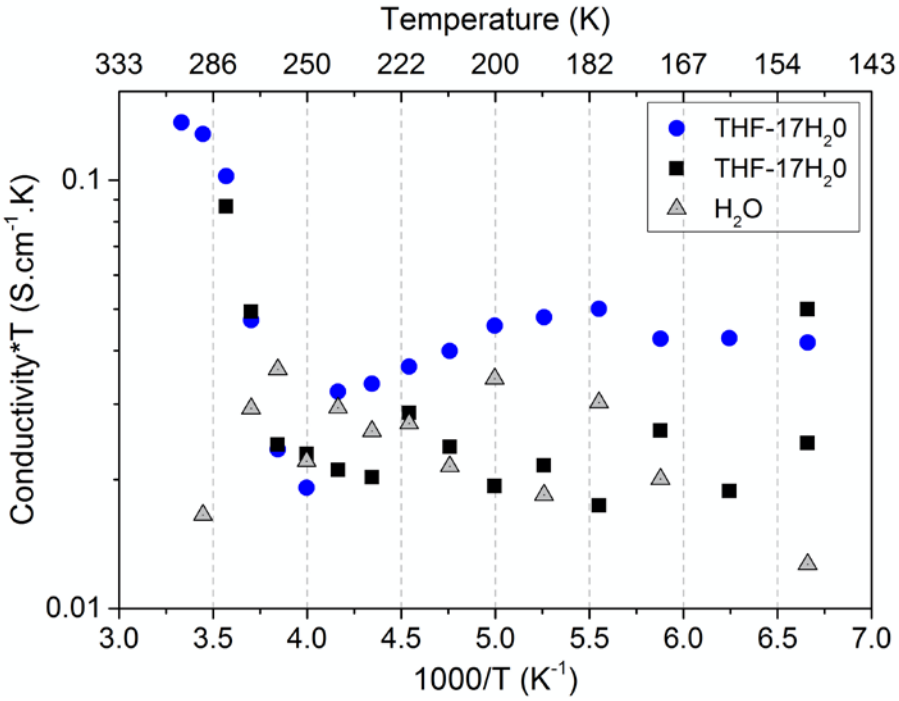

Figure V. 14. The conductivity of THF-17H_2O hydrate in log-scale with respect to the temperature, two sets of measurements done in the same conditions (Black, square) and (Blue, circle) and H_2O (grey, triangle).

ii. $HClO_4$ hydrate conductivity study

Impedance measurements are performed on the $HClO_4$ – 5.5H_2O sample forming the SI hydrate structure [MOO 87]. The conductivity times the temperature in the log scale with respect to the inverse of the temperature is shown in Figure V. 15. The protonic conductivity

increase with the temperature from 0.00217 S.cm^{-1} at 150 K to 0.36884 S.cm^{-1} at 260 K. We noticed a change in the linear increase of the conductivity in the Figure V. 15 between the temperature 210 K and 220 K. This jump is evidence of a change in the sample phase, going from solid state to liquid state. The diffusion coefficient is different if we consider the solid phase or the liquid phase. We focus on the solid phase of the sample, which is the hydrate phase.

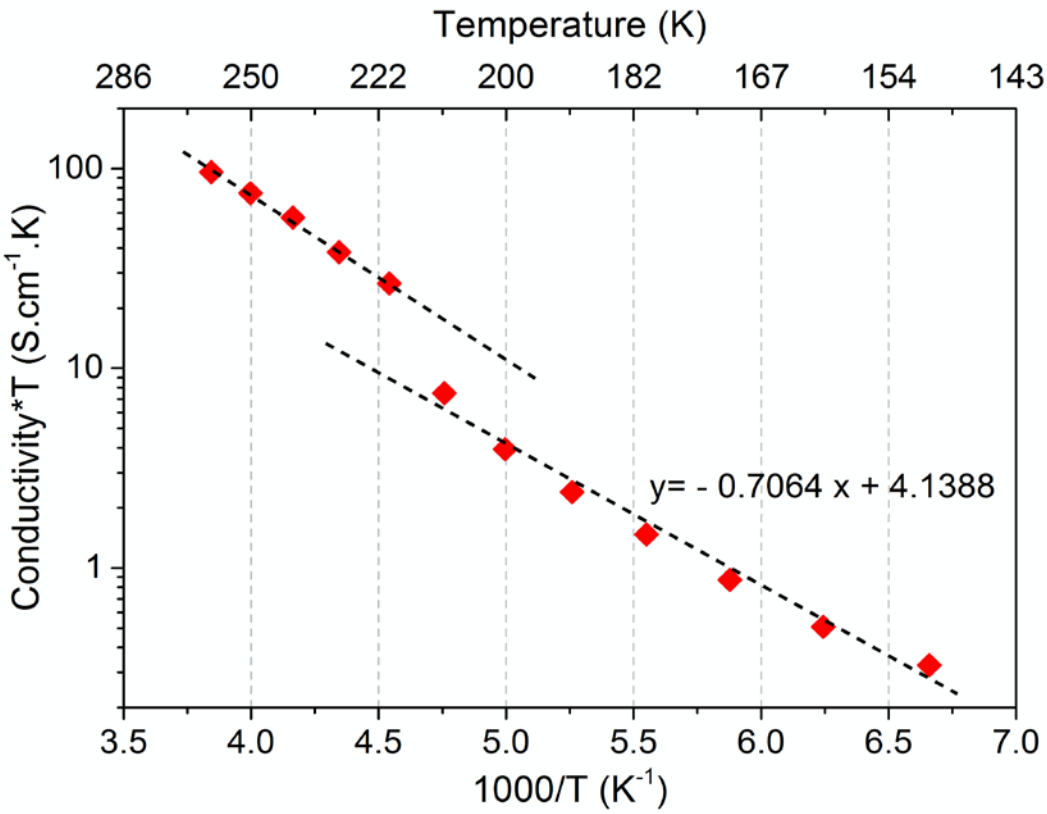

Figure V. 15. The conductivity of $HClO_4 – 5.5H_2O$ in log scale with respect to the temperature. Linear fit in black.

From Nernst-Einstein equation and the Arrhenius law (see part B), we know that the linear fit on Figure V. 15 give as a slope the activation energy E_A over Boltzmann constant ($k = 8{,}6173303.10^{-5}\ \mathrm{eV.K^{-1}}$).

$$\frac{E_A}{k} = 0.7064 \qquad [59.V]$$

The study of the acid concentration influence on the conductivity of $HClO_4$ hydrate is shown

in Figure V. 16. From the Nernst-Einstein equation and the Arrhenius law, the slope of the linear fit gives the diffusion coefficient

$$slope = \frac{De^2}{kT} = 4.59682.10^{-4} \pm 5.14083.10^{-5} \quad [60.V]$$

$$D = 4.59682.10^{-4} \text{ x } \frac{\text{kT}}{e^2} \quad [61.V]$$

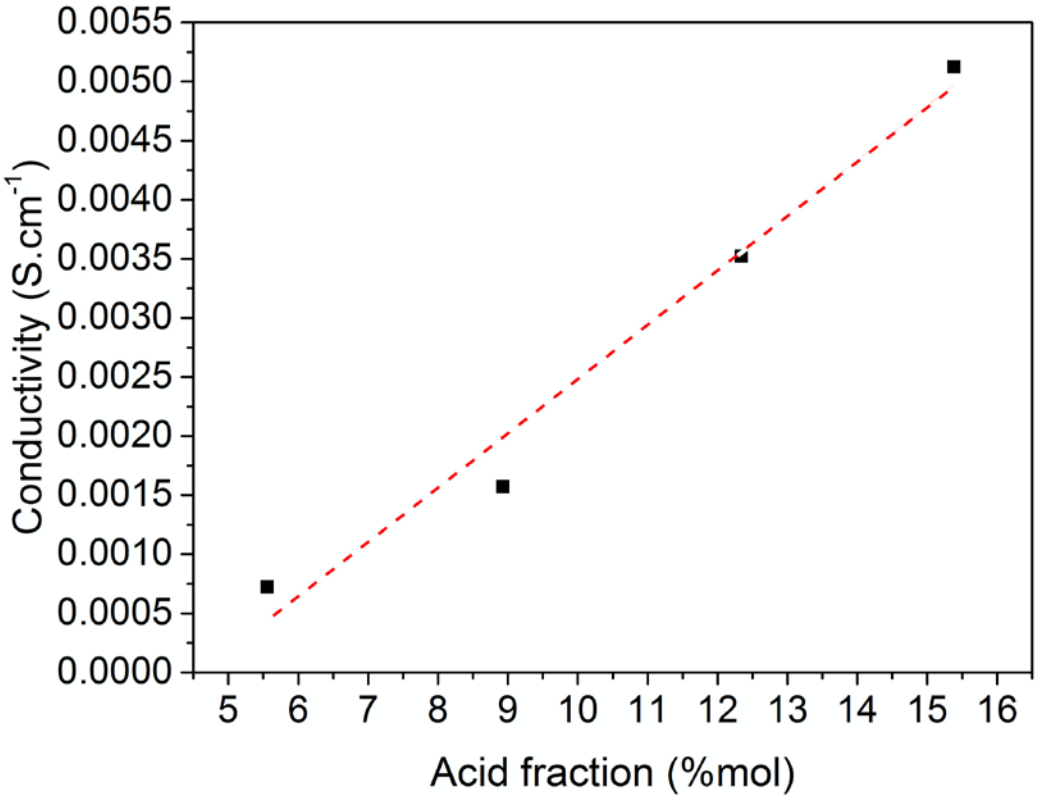

Figure V. 16. Conductivity of $HClO_4$ hydrate with respect to the acid fraction at 170 K.

The diffusion coefficient obtained for the pure SI hydrate structure is used later on when applying the solution solid model. The mixing of hydrate structure for samples with SII and SI effect on the conductivity is investigate through this model.

2. Conductivity study for a fixed acid fraction.

i. Domain 1 samples

The sample at the acid fraction 0.347 %mol which formed the SII hydrate structure is studied first. The conductivity results are presented in Figure V. 17 as the conductivity times the temperature in the log scale ($S.K.cm^{-1}$) with respect to the temperature ($1000/T\ K^{-1}$).

The first observation is the linear increase of the conductivity from 150 K to 260 K. Between 260 K and 270 K, the conductivity value jumps suddenly. From 270 K, the conductivity increases again linearly. The break in the linear evolution of the conductivity corresponds to a structural change in the samples. The sample goes from a solid state at 260 K to a liquid form at 270 K. The conductivity is higher in a liquid state than in a solid state due to the combined effect of the Vehicular and the Grotthuss mechanism responsible for the protonic conductivity presented in Chapter I. The phase transition around 270 K is in agreement with the melting temperature known for the SII hydrate structure with THF. Focusing on the samples in hydrate structure, the conductivity measurements are fitted by a linear function as expected by the Nernst-Einstein model presented in part B. The slope obtain gives

$$\frac{E_A}{k} = 1.26356$$

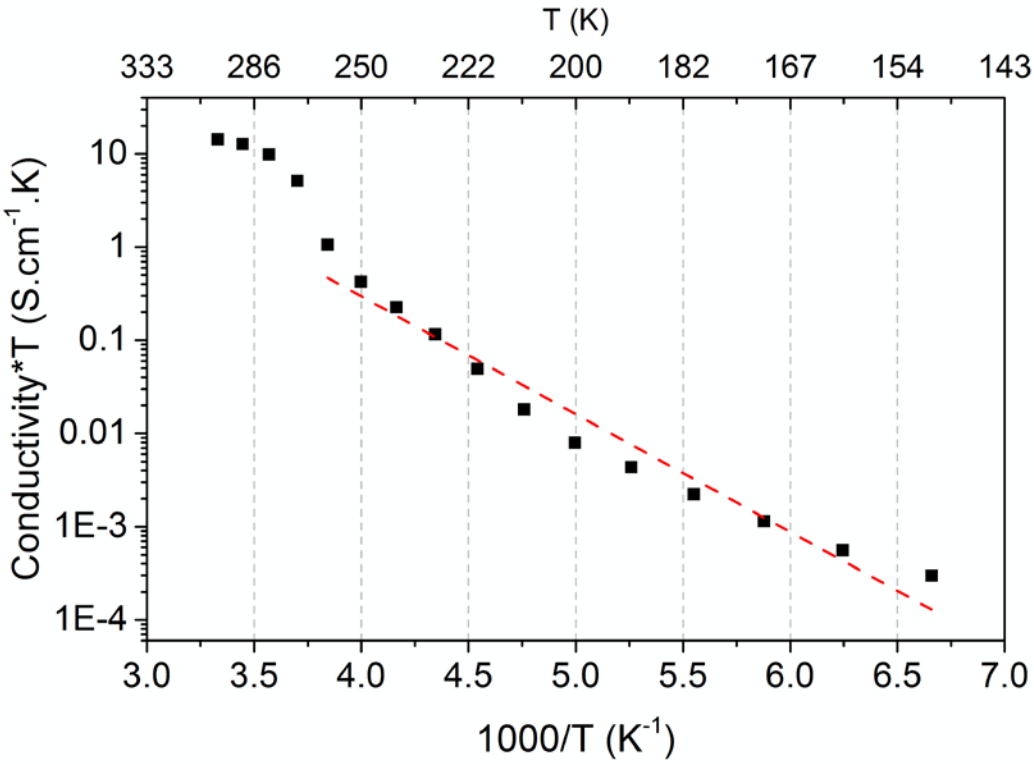

Figure V. 17. Conductivity with respect to the temperature of mixed hydrate at 0.347 %mol acid fraction.

ii. Domain 3 samples

The conductivity data for the sample at 4.627 %mol are presented in Figure V. 18. We noticed three different regimes in the conductivity corresponding to structural change happening in the sample according to the temperature. At low temperature (150 K to 180 K) the sample has SI hydrate structure and ice according to the XRD study in Chapter IV. When increasing the temperature, the SI hydrate structure melt and only the ice structure remain in the sample. At 250 K and over, the sample is fully liquid. The structural evolution of the sample implies for each change, a different activation energy.

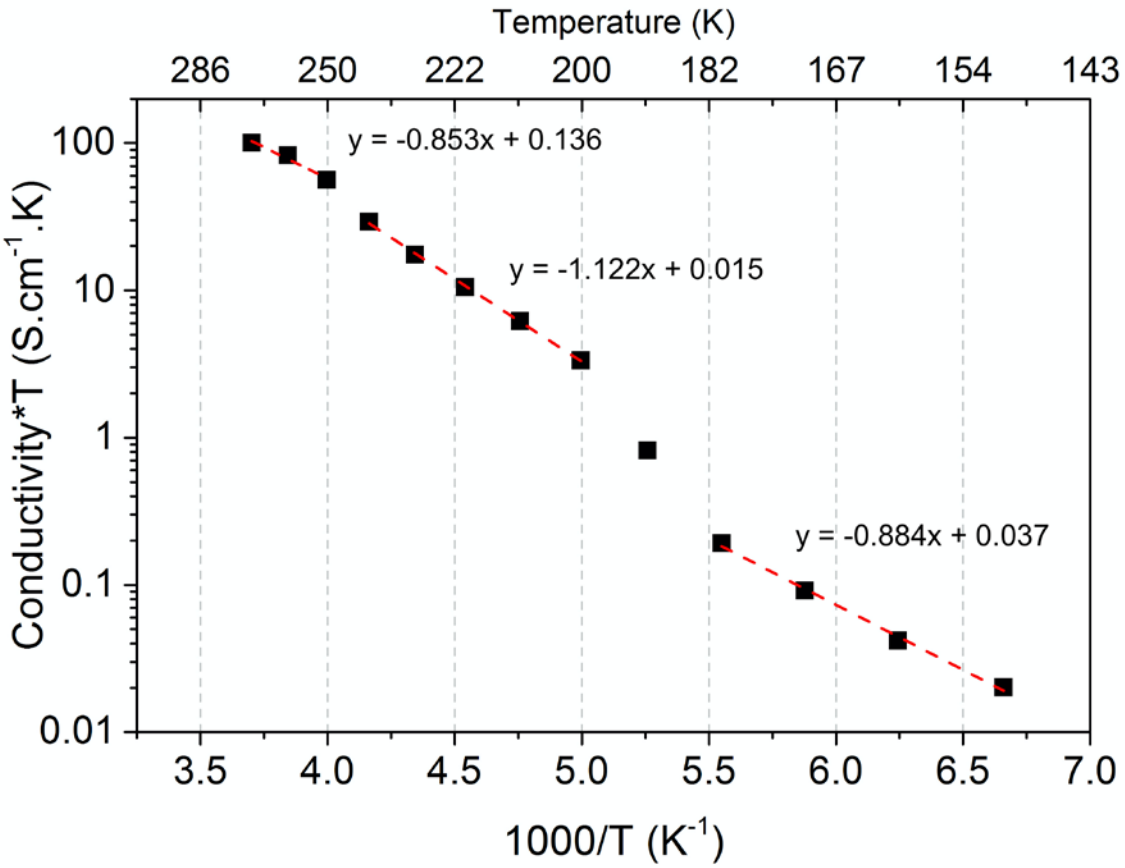

Figure V. 18. Conductivity with respect to the temperature of mixed hydrate at 4.627 %mol acid fraction.

The structural evolution of the samples with the temperature is translated, by a change in the linear behaviours of the conductivity measurements in Figure V. 18. The linear fit for each sample structure are given in Figure V. 18.

The simple but powerful model of Nernst-Einstein gives the linear evolution of the conductivity of the SI and SII hydrate structures depending on the temperature.

3. Conductivity study at fixed temperature.

To recall, samples with acid fractions lower than 0.694 %mol form SII hydrate structure and samples with acid fractions higher than 2.77 %mol form SI hydrate structure.

The case of the samples with acid fraction between 0.694 %mol and 2.778 %mol will be treated later in another section.

i. At T = 170 K.

The conductivity of the mixed hydrate at various acid fractions is presented in Figure V. 19 for the temperature at 170 K.

By the Arrhenius law, the conductivity σ increase linearly proportionally to the concentration c with $\sigma(c) = 0 \; for \; c = 0$ which is a condition imposed on the linear fit in Figure V. 19.

The Nernst-Einstein law gives the conductivity relation with the concentration for a constant temperature *T* and the diffusion coefficient *D* (fixed by the porous material considered). The slope of the linear fit gives

$$\frac{De^2}{kT} = 4.58237.10^{-5} \qquad [62.V]$$

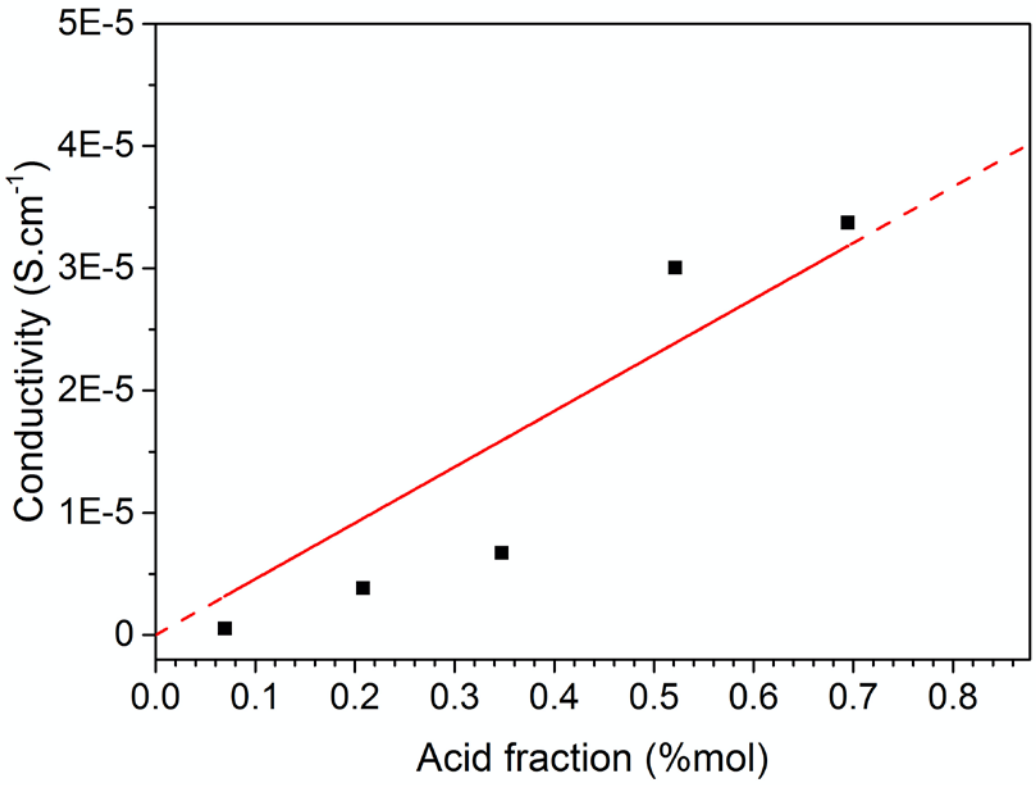

Figure V. 19. Conductivity with respect to the acid fraction at 170 K.

A similar study is performed on the data with the acid fraction over 2.77 %mol. The

conductivity results obtain at 170 K for the various mixed hydrates are presented in Figure V. 20. The conductivity value for the domain 1 and 3 where only one type of hydrate structure is formed are fitted linearly. The linear evolution of the conductivity with respect to the acid fraction is coherent with the model of Nernst-Einstein. The slopes of the linear fit in Figure V. 20 are different ($\text{slope}\,1 = 4.58237.10^{-5}$ and $\text{slope}\,3 = 1.0505.10^{-4}$). In these mixed hydrates, the domain 3 have a better diffusion coefficient than the domain 1. One of the explanation is the difference in the actual quantity of hydrate formed in these systems. In the Chapter IV, relative fractions of the structures were determined for the various samples. For the domain 3, the relative fractions of SI were increasing with the acid fraction, while the relative fractions of ice decrease.

Another factor to explain the differences is that the SI hydrate structure has a better diffusion coefficient of the proton due to its crystalline symmetry than the SII hydrate structure.

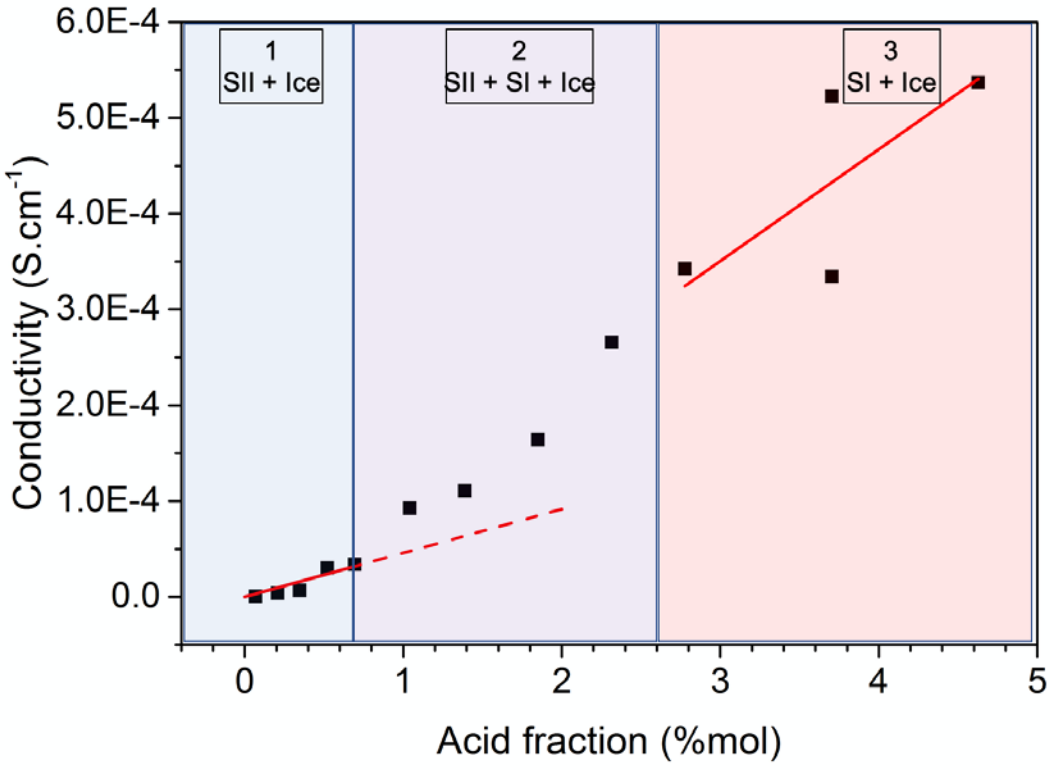

Figure V. 20. Conductivity data of the mixed hydrate samples with respect to the acid fraction at 170 K.

ii. At T = 230 K

At 230 K, the samples formed SII hydrate structure with Ice at acid fraction lower than 2.778 %mol. Above this acid fraction, only the ice structure were observed (see Chapter IV). The conductivity performed at 230 K on the various mixed hydrates are presented in Figure V. 21. The XRD structural determination is shown according to the acid fractions, SII and Ice structure in Blue and Ice structure in grey.

A linear fit of the conductivity values is not possible over the data from the same structural domain. Only considering the effect of the crystalline structure detected by XRD experiment (Chapter IV) is not sufficient to model the conductivity. Indeed, the samples at acid fractions over 0.694 %mol, not only have the SII hydrate structure and Ice but also acid molecules that used to be in SI structure. At 230 K, the SI hydrate structure melt and at least part of the water molecules formed the ice structure, as shown in the study of the XRD peaks evolution with respect to the temperature in Chapter IV. The presence of the acidic ice with SII structure and pure ice has modified the diffusion behavior found for the SII and Ice in the previous study at 170 K. A new diffusion coefficient is determined here for samples up to 1 %mol. For samples with higher acid fraction, the conductivity value shows an exponential increase. The increase of the acid fraction increase the number of acid molecules in the samples. In small quantities, the acid molecules could be considered as impurity in the ice structure, conserving the solid integrity of the samples. But for higher acid concentration, the ice formation is compromised. Part of the water and acid molecules are present in a liquid state. This phenomenon was noted visually by microscope during Raman imaging experiments. The layer formed by the water and acid molecules influence positively the conductivity of the mixed hydrate. This result join the study of the HPF_6 hydrate by Desplanche *et al.* [DES 18], where a micro structured layer was also identified with the HPF_6 hydrate structure for a given temperature (see Chapter I).

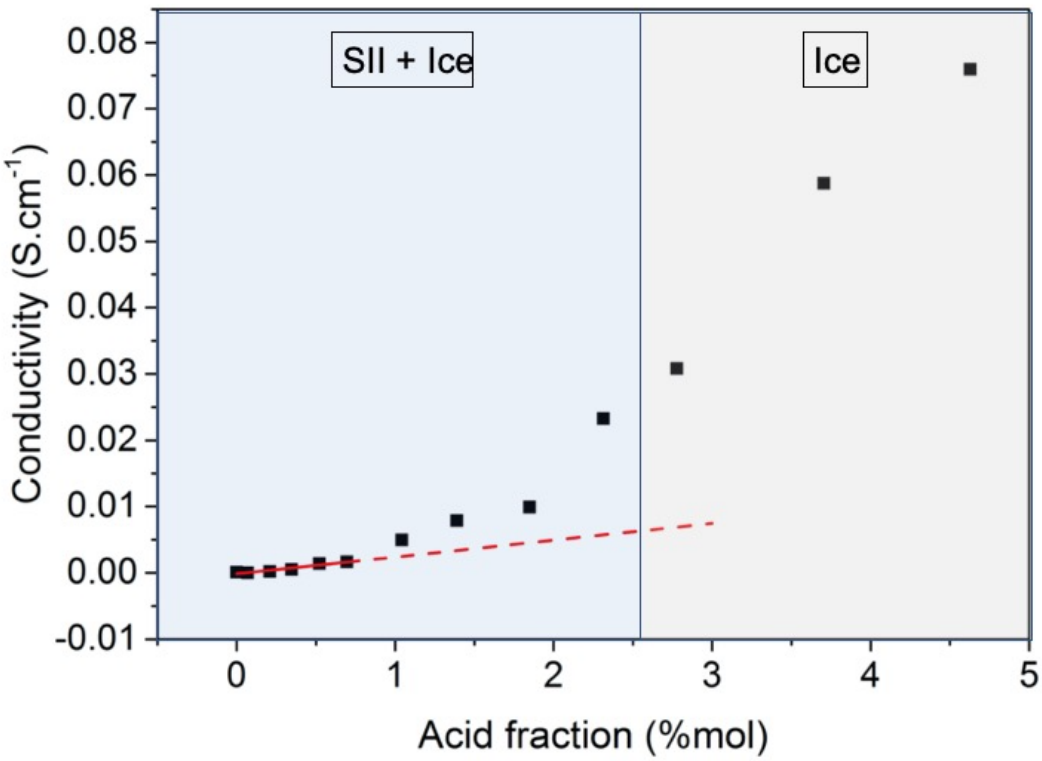

Figure V. 21. The conductivity of mixed hydrate $THF - HClO_4$ sample with various acid fraction at 230K.

No quantification of this phenomena was possible with the XRD experiments presented before. Indeed, the quantitative XRD study only indicates the relative fractions of the crystalline structure in a sample at a given temperature. We formed the enlighten hypothesis that the increase of acid fraction which increase the number of acid molecules leads to the increase of liquid layer in the samples. The formation of layer enhanced the conductivity in the mixed hydrate at 230 K. To quantify the effect of the layer for these samples, conductivity models are applied in the next part when we focus on the samples from the domain 2.

4. Mixing of SII and SI structures in mixed hydrate

In this part, the study is focused on the samples with acid fraction between 0.694 and 2.77 %mol. For these samples in the domain 2, identified by the XRD study (see Chapter IV), the SI and SII hydrate structure coexist for temperature below 200 K. When increasing the temperature, the melting of the SI structure was observed and the crystalline structure

remaining were the SII hydrate structure and the ice structure.

i. Conductivity study at fixed acid fraction: domain 2 samples

The conductivity results for the samples at acid fraction 2.315 %mol, presented in Figure V. 22, show a light jump in the conductivity at 190 K. This effect is due to the melting of the SI hydrate structure in the samples. The second jump at 260 K, correspond to the melting of the SII structure and the ice. The conductivity observations are in agreements with the structural changes determine by the XRD experimental study for this sample belonging to the domain 2. Linear fit were made visualised the linear change in the conductivity evolution.

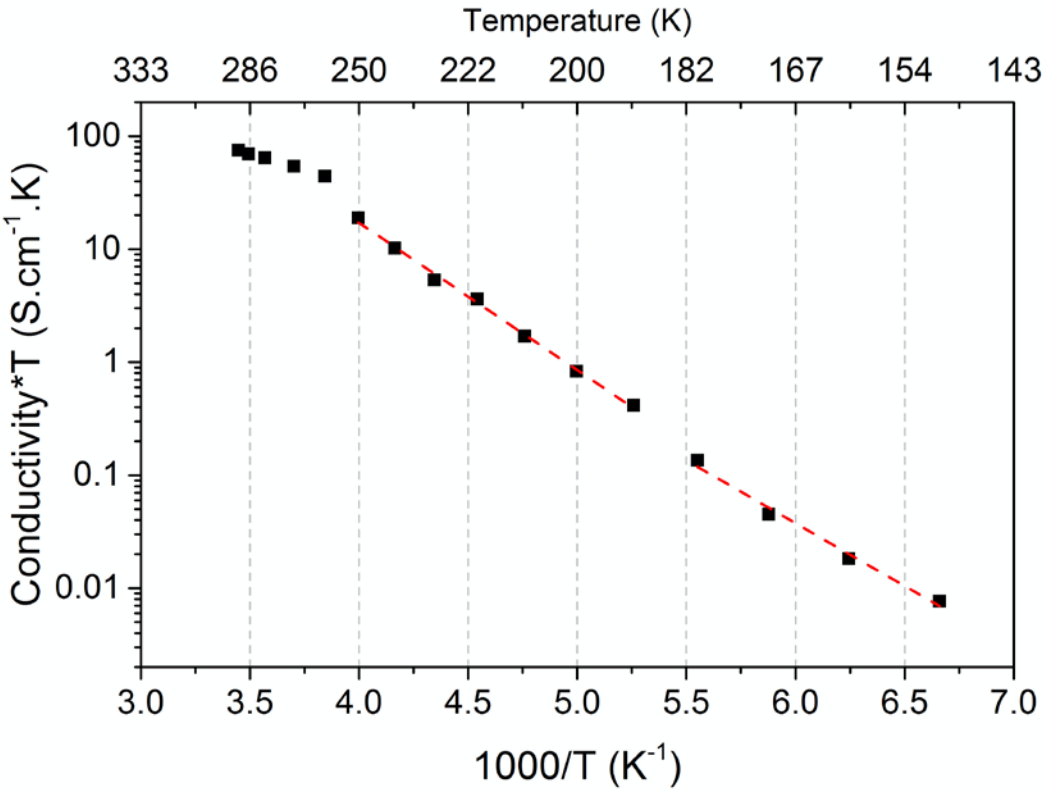

Figure V. 22. Conductivity of mixed hydrate with an acid fraction of 2.315 %mol with respect to the temperature.

ii. The conductivity evolution at fixed temperature

The mixed hydrate samples categorized in the domain 2 are mixture of SI and SII hydrate structure and Ice.

To take into account their structural particularity we used the Solution solide model. Described in the previous sections, this model considers the total conductivity of the sample as the sum of the conductivity of each structure that composed it. Different hypothesis are tested with the solution solid model.

For the model, we selected the conductivity of the SII hydrate structure. The conductivity of the SII structure with THF and $HClO_4$ was determined previously for the domain 1 sample with acid fraction of 0.694 %mol. This sample at the limit of the domain 1 represent the SII hydrate with THF guests and $HClO_4$ guests which replaced the THF molecules in the structure to their maximum. (recall: the unit cell chemical formula for the SII structure is 7THF -1$HClO_4$-136 H_2O). Then, for the conductivity of the SI hydrate value, it dependence in the acid concentration needs to be consider. Indeed, SI structure conductivity $\sigma_{SI} = f(c)$ was determined in the previous sections. Combining the conductivity of the SII hydrate structure and the one for the SI, we apply the model to the impedance measurement performed on the various samples at 170 K.

The solution solid model is given by:

$$\sigma(c) = \Delta_{SII}(c).\sigma_{SII} + \Delta_{SI}(c).\sigma_{SI}(\mathrm{c}) \,[+ \Delta_{Ih}(c).\sigma_{Ih}] \qquad [63.V]$$

,with the conductivity of the ice negligible compare to the conductivity of the SI and SII hydrate structure.

The model is divided in cases:

- Model 1, the fraction of SI and SII is consider constant $\Delta_{SII}/\Delta_{SI} = cst$; ie independent from the acid concentration.

- Model 2 , the fraction of SII and SI change with the acid fraction: $\Delta_{SII}/\Delta_{SI} = f(c)$.

The fractions of the hydrate structures were investigated in the previous Chapter IV. The XRD study presented, highlighted the dependence of the relative fraction formed in the various samples with the acid fractions. The relative fractions are used with the solution solid model 2.

The model 2 data are shown in Figure V. 23 with the conductivity values obtained with respect to the acid fractions.

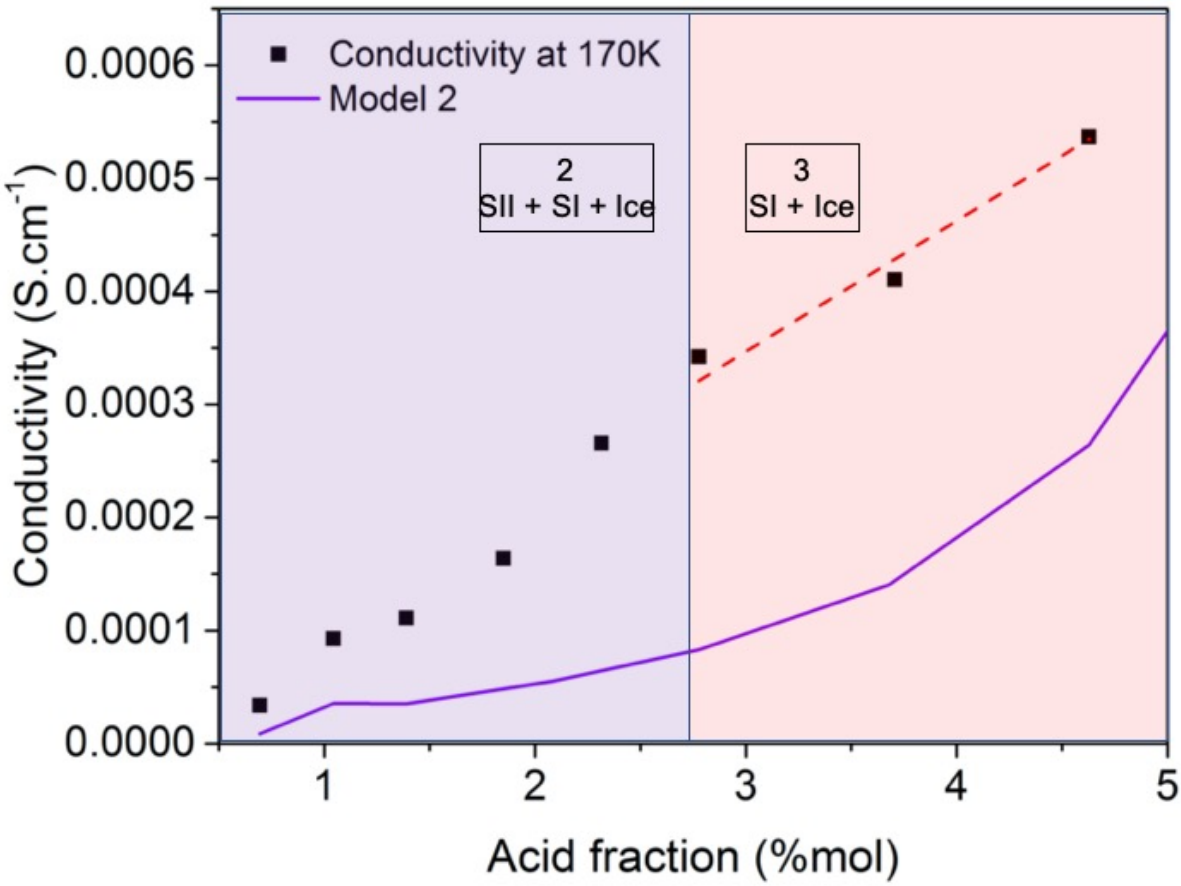

Figure V. 23. Conductivity values with respect to the acid fractions for mixed hydrates at 170 K. Model 2 (pruple line).

iii. Solution solid Model and interface

From the solution solid model, conductivity $\boldsymbol{\sigma}$ can be fitted by adding the contribution of each structure (fraction Δ_X) and their conductivity $\boldsymbol{\sigma_X}$. To go further in the solution solid model, interactions needs to be consider.

The nature of the interface between the structure at 170 K submit to hypothesis. In the model of perfect solution solid, mixed hydrate samples have H_2O molecules not participating in hydrate structure. They formed the ice structure present in all the samples. One assumption is to consider that part of the water molecules is as a monolayer (or an amorphous water structure) around the hydrate structures which increases the protonic conductivity.

From the Raman imaging investigations on the various mixed samples brings the hydrate structure were identified

What is the quantity and structure of the extra water? Is the assumption of a monolayer of H_2O correct?

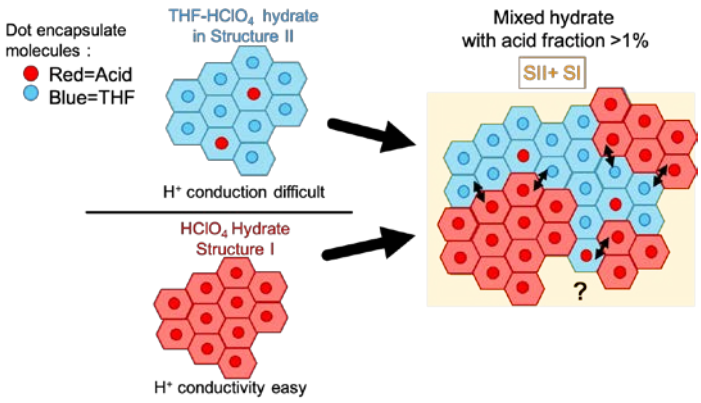

Figure V. 24.Illustration of the interface effect in the mixing of the SI and SII hydrate structure.

Another assumption that we made is that acid molecules are all integrated in the hydrate structure. However, for the samples at 230 K, we found indication of acidic ice. The presence of this ice with acid molecules, acting like impurities in the system, at other temperature needs to be investigated for further models.

E. Conclusions

The localization of THF molecules at high acid fraction might influence the interpretation of the samples, especially, where the two hydrate structures were observed. The first interpretation was that the SI hydrate structure is only formed with the acid guest $HClO_4$ present in all cages. With this study, the proof of co-inclusion of THF and $HClO_4$ is brought up. The new structural environment of the SI hydrate structure The THF molecules localization in the large cages of the structure SI is possible.

This work has highlighted the parameters of mixed hydrate structure that are influencing the conductivity.

The impact of the mixing of hydrate structures, especially the interfaces were discussed and from the collected data possible explanation on the conductivity behaviours are given. The complexity of this systems need further investigations.

General conclusion and perspectives

In this work, the combination of experimental and simulations studies allowed us to investigate various properties influencing the very interesting systems that are strong acid hydrates. Gaining interest for their unique properties that are of interest to solve energy issues. Among the many original physico-chemical properties of clathrate hydrates, the understanding of the high proton conductivity of acid hydrates up to relatively low temperatures has been at the heart of this PhD research. The use of Raman spectroscopy, coupled with X-ray diffraction and quantum chemical calculations (DFT), has provided new data and new answers to the study of the physicochemical properties of these systems.

Due to their specific properties, these hydrates have proven to be very good solid proton conductors with original physicochemical properties and promising applications. The focus was put on the HPF_6 and $HClO_4$ hydrate which are among the best conductors.

In this work, the localization of the ionic defect and their influence on the hydrate structural properties, as well as the cage occupancy, are important questions for the understanding of hydrates systems. Due to an ionic superconductivity of up to 10^{-1} $S.cm^{-1}$ and a melting temperature close to room temperature, hexafluorophosphoric acid hydrates appear to be excellent candidates for application as fuel cell electrolytes. In previous experimental work, the impurities were attributed to the reactivity of the HPF_6 with water, forming species like HPO4-. The effect of the impurities on the protonic conductivity where noted by impedance measurements. They investigated further the HPF_6 hydrate with impurities by Raman scattering and NMR. While some of the impurities were detected as being in a micro-structure environment, there were also indication of the encapsulation of this imputities with the HPF6 hydrate. Indeed, the DFT simulation performed in this work tended to similar conclusions.

The first step of this work was to select the correct parameters for the simulations of hydrate systems. The balance between the cost and accuracy of the calculations has been discussed in Chapter II. The functional and various parameters were tested on hydrate systems as shown

in Chapter II and finally on the acid hydrate in Chapter III. In chapter III, the stability study performed on the HPF_6 hydrate confirmed its stability when impurities guests were incorporated into the structure in small quantities. These results converge with the observation made in the experimental study. The simulations done here have shown the accuracy of this technique in answering the fundamental question of guest localization in hydrate structure. The study of HPF6 hydrate reinforces the importance of the localization of the species to understand the mechanism of the protonic conductivity in hydrate systems.

To better understand the role played by the acid concentration on the protonic conductivity, it is possible to prepare mixed hydrates (i.e., encapsulating two guest species) by co-including $HClO_4$ acid and tetrahydrofuran (THF) molecules (THF hydrate is a prototypical clathrate hydrate, widely investigated). By varying the THF to $HClO_4$ ratio, such mixed hydrates offer the opportunity to control the concentration of the acidic defects in the hydrate structure. The co-inclusion of THF and $HClO_4$ molecules in the SII hydrate, known from the literature study, allowed the strict study of the acid concentration in hydrate structure on the conductivity. the study of the structure influence is also possible by tuning the acid concentration on this mixed hydrate.

During this PhD, work was carried out on the fundamental understanding of the physical chemistry of these systems. It was necessary to deepen and complete our knowledge of the formation, stability and dynamics of these systems. Thus, the use of different characterisation techniques, such as Raman spectroscopy, X-ray diffraction and impedance spectroscopy, has made it possible to provide new information and new elements concerning their physicochemical properties.

The mixed hydrate of THF/$HClO_4$ with various acid fractions has been studied by X-Ray diffraction in Chapter IV to better understand the influence of the acid concentration on the hydrate structure and stability. The structural investigation by XRD experiments determined three structural domains for the mixed hydrates depending on the acid fraction and the temperature. The first domain is found for the samples with a low acid fraction from 0 to 0.69 %mol, where the SII hydrate structure is observed with ice. The second domain is described by the three structures cohabiting, the SII and SI hydrate structures and the hexagonal ice for

the samples of acid fraction up to 2.77 %mol. For samples with higher acid fractions, only the SI hydrate structure is found; it's the third domain. The thermal stability of the mixed hydrates structures was investigated. The study of the evolution of the XRD peaks intensities highlighted the influence of the acid molecules on the structural stability of hydrates. The melting temperature found for the SI hydrate structure is different from the pure $HClO_4$ hydrate. The modification of the hydrate melting temperature might be explained by the possible co-inclusion of $HClO_4$ and THF in the so-called type SI structure. To our knowledge, this would be the first observation of the encapsulation of THF in SI structure. The localisation of THF molecules in the mixed hydrate when the SII structure is not formed needs further investigation.

The ice melting temperature in the samples is lower than 273 K (melting temperature for pure ice) and indicates the disruptive effect of the acid molecules on the structure. This effect is mainly observed for samples in domain 2 and 3, where the SI hydrate melt around 200 K and the acid molecules from the SI hydrate is mixed with the ice. By X-Ray diffraction, the mixed hydrate structures were identified as a function of their acid fraction and temperature. Their temperature stability was studied and revealed an unexpected behaviour for the hydrate structures.

The XRD can be used to resolved the full crystalline structure of hydrates by Rietveld refinement. This method could bring information on the positions of the species in the hydrate's cages. The resolution of the Rietveld refinement is challenging for the hydrate structure. The mixing of the hydrate structure adds to the complexity of the resolution, but as we saw in our XRD study, by selecting the temperature, some of the mixed hydrate samples can be stabilised in one type of structure.

Before the structural findings of the mixed hydrate by XRD experiments are applied to the impedance measurements, technical models to interpret the conductivity in these hydrate structures are presented. This study highlighted the importance of the structural arrangement of the different structures in the mixed hydrate samples.

Raman imaging was used to study the distribution of the various phases at the micro-scale in

the mixed hydrate, highlighting the heterogeneity of the samples. The study by principal component analysis gave a picture of the different pathways for protonic conductivity according to the acid concentration.

In the next section of chapter V, we looked at how the acid concentration and structure domains influence the protonic conductivity of the mixed hydrate. The conductivity study was separated in different cases to consider one parameter of the hydrate at a time. First, to follow the influence of the temperature on the hydrate, we study the evolution of the conductivity with respect to the temperature at a given acid concentration. From this study, the structural changes happening in the sample were observed and confirmed the observation made by the XRD. The influence of the hydrate structure on the conductivity is affirmed here.

For the next case, we look at the conductivity with respect to the acid concentration at a fixed temperature. To study the strict influence of the acid concentration, and with the help of the structural identification by XRD made in chapter IV, the conductivity was studied for two ranges of acid fractions corresponding to the two domains (1 and 3) at 170 K. In these domains, the samples were found to form one hydrate structure, and their conductivity evolution match the linear evolution expected for the 3D protonic diffusion in a porous solid. An unexpected behaviour was found for the study at 230 K. according to the XRD experiments, the structures formed were at first the mixing of SII hydrate and ice, then at an acid fraction higher than 2.7 %mol only ice structure. With the assumption of the negligibility of the ice conductivity compared to the one of the SII structure, we expected two linear behaviour corresponding to the structural change of the samples. However, it wasn't the case. The conductivity changed behaviour at 1 %mol. This sample (mixing SII and Ice at 230 K) corresponds to the sample that formed, at a lower temperature, the SI structure. The melting of SI led to the partial formation of Ice that was identified as acidic ice by XRD. The conductivity of this acidic ice is then not negligible anymore.

The last case is the more complex one. Indeed, the mixing of the SI and SII hydrate structures needs the application of conductivity models to determine the parameters influencing the conductivity. The solution solid model where a sum of the SII and SI structure conductivity, deduced previously, does not fit the values for the mixing structures samples. These results

highlighted the non-negligible contribution of the interface between the structure. The effect and nature of this interface is discussed at the end of this work and revealed the necessity of further investigations.

The impedance measurements on the mixed THF/$HClO_4$ hydrates showed that the protonic conductivity is controlled not only by the ionic defect concentration but also by the formed hydrate structure and the mesoscopic organisation within the sample as revealed by X-ray diffraction analysis and Raman imaging. Combining the techniques highlight the parameters in the hydrate samples influencing the conductivity.

To go further, the use of Raman imaging and its spatial resolution could bring answers to the localization of the different species and micro structuration detected by the XRD experiment and Impedance study. The mapping of the sample surfaces performed at 150 K could be extended to a temperature-dependent study to observe and especially quantify the possible microstructure layer for the samples with the mixing of SII and SI hydrate structures.

Understanding the mechanism behind the conductivity in hydrate necessitates the investigation of more hydrates with different anionic guests. The conductivity study of the mixed hydrate of THF and $HClO_4$ underlines the effect of the structural interface in the improvement of the conductivity. One of the next investigations could be on controlling the hydrate grain size to tune the effect of the interface on the conductivity.

In addition, to complete our study, the thermodynamic stability of the mixed hydrates has to be investigated.

For the theoretical simulations, Ab-initio calculations are an interesting technique that could allow us to test different configurations in hydrate structure (guest position and occupation). Simulated the protonic conductivity depending on the cages filling in hydrate could be possible using a thermostat with the ab-initio simulations. This study combines with the observation of the experimental conductivity, will bring answers on the acid concentration and structure influence.

Understanding the influence of the hydrate structure on the proton conductivity and the mechanisms involved in forming acid hydrates will be crucial to open the possibility of using hydrates in decarbonised energy applications. The present Thesis project is a contribution towards this aim.

REFERENCES

[AGM 95] Agmon, N. The Grotthuss Mechanism. Chem. Phys. Lett. 1995, 244 (5-6), 456-462. https://doi.org/10.1016/0009-2614(95)00905-J.

[ALA 12] Alavi, S.; Ripmeester, J. A. Effect of Small Cage Guests on Hydrogen Bonding of Tetrahydrofuran in Binary Structure II Clathrate Hydrates. J. Chem. Phys. 2012, 137 (5), 054712. https://doi.org/10.1063/1.4739928.

[ART 99] Artacho, E.; Sanchez-Portal, D.; Ordejon, P.; Garcia, A.; Soler, J. M. Linear-Scaling Ab-Initio Calculations for Large and Complex Systems. phys. stat. sol. (b) 1999, 215 (1), 809-817. https://doi.org/10.1002/(SICI)1521-3951(199909)215:1<809::AID-PSSB809>3.0.CO;2-0.

[ASC 94] Aschrafimahabadi, S.; Cappadonia, M.; Stimming, U. Proton Transport in Solid Electrolytes with Clathrate Structure. Solid State Ion. 1994, 70-71, 311-315. https://doi.org/10.1016/0167-2738(94)90328-X.

[BAB 18] Babu, P.; Nambiar, A.; He, T.; Karimi, I. A.; Lee, J. D.; Englezos, P.; Linga, P. A Review of Clathrate Hydrate Based Desalination To Strengthen Energy-Water Nexus. ACS Sustainable Chem. Eng. 2018, 6 (7), 8093-8107. https://doi.org/10.1021/acssuschemeng.8b01616.

[BEA 21] Beattie, J. R.; Esmonde-White, F. W. L. Exploration of Principal Component Analysis: Deriving Principal Component Analysis Visually Using Spectra. Appl Spectrosc 2021, 75 (4), 361–375. https://doi.org/10.1177/0003702820987847.

[BEC 88] Becke, A. D. Density-Functional Exchange-Energy Approximation with Correct Asymptotic Behavior. Phys. Rev. A 1988, 38 (6), 3098-3100. https://doi.org/10.1103/PhysRevA.38.3098.

[BEC 93] Becke, A. D. A New Mixing of Hartree-Fock and Local Density?functional Theories. The Journal of Chemical Physics 1993, 98 (2), 1372-1377. https://doi.org/10.1063/1.464304.

[BED 13] Bedouret, L. Modélisation théorique et expérimentale du mécanisme de conduction

protonique dans un clathrate hydrate ionique, 2013, Thèse de l'Université de Bordeaux.

[BED 14] Bedouret, L.; Judeinstein, P.; Ollivier, J.; Combet, J.; Desmedt, A. Proton Diffusion in the Hexafluorophosphoric Acid Clathrate Hydrate. J. Phys. Chem. B 2014, 118 (47), 13357-13364. https://doi.org/10.1021/jp504128m.

[BER 13] Berrod, Q. Relation structure - transport dans des membranes et matériaux modèles pour pile à combustible, Thèse de l'université de Grenoble, 2013.

[BER 14] Berland, K.; Hyldgaard, P. Exchange Functional That Tests the Robustness of the Plasmon Description of the van Der Waals Density Functional. Phys. Rev. B 2014, 89 (3), 035412. https://doi.org/10.1103/PhysRevB.89.035412.

[BIR 47] Birch F., Finite Elastic Strain of Cubic Crystals, Phys. Rev. 1947, 71, 809-824.

[BJE 57] Bjerrum, N. Structure and Properties of Ice. 1952, 115, 7.

[BOD 55] Bode H.; Teufer G. Die Kristallstruktur der Hexafluorophosphorsäure. Acta Cryst. 1955; 8; 611-614.

[BOR 92] Borkowska, Z.; Cappadonia, M.; Stimming, U. Interfacial and Bulk Electrolyte Properties in Frozen Electrolyte Studies. Electrochimica Acta 1992, 37 (3), 565-568. https://doi.org/10.1016/0013-4686(92)87049-6.

[BOR 98] Borkowska, Z.; Opallo, M.; Tymosiak-Zielinska, A.; Zoltowski, P. Tetraalkylammonium Cation Clathrate Hydrates in Interfacial Electrochemistry. Colloids Surf. Physicochem. Eng. Asp. 1998, 134 (1-2), 67-73. https://doi.org/10.1016/S0927-7757(97)00328-2.

[BOS 11] Boswell R., Collett T. S., Current perspectives on gas hydrate resources, Energy Environ. Sci. 2011, 4, 1206-1215.

[BRA 02] Brandbyge, M.; Mozos, J.-L.; Ordejón, P.; Taylor, J.; Stokbro, K. Density-Functional Method for Nonequilibrium Electron Transport. Phys. Rev. B 2002, 65 (16), 165401. https://doi.org/10.1103/PhysRevB.65.165401.

[BRI 49] Brickwedde, L. H. Properties of Aqueous Solutions of Perchloric Acid. J. Res. Natl. Bur. Stand. 1949, 42 (3), 309. https://doi.org/10.6028/jres.042.026.

[BUR 12] Burke, K. Perspective on Density Functional Theory. J. Chem. Phys. 2012, 136 (15), 150901. https://doi.org/10.1063/1.4704546.

[CAP 94] Cappadonia M., Kornyshev A.A., Krause S., Kuznetsov A.M., Stimming U., Low-temperature proton transport in clathrates, J. Chem. Phys. 1994; 101; 7672-7682.

[CEP 80] Ceperley, D. M.; Alder, B. J. Ground State of the Electron Gas by a Stochastic Method. Phys. Rev. Lett. 1980, 45 (7), 566-569. https://doi.org/10.1103/PhysRevLett.45.566.

[CHA 08] Cha, J.-H.; Shin, K.; Choi, S.; Lee, S.; Lee, H. Maximized Proton Conductivity of the HPF 6 Clathrate Hydrate by Structural Transformation. J. Phys. Chem. C 2008, 112 (35), 13332-13335. https://doi.org/10.1021/jp805510g.

[CHA 15] Chaouachi M., Falenty A., Sell K., Enzmann F., Kersten M., Haberthür D., Kuhs W. F., Microstructural evolution of gas hydrates in sedimentary matrices observed with synchrotron X-ray computed tomographic microscopy. Geochem. Geophys. Geosyst. 2015, 16, 1711?1722.

[CHO 07] Choi, S.; Shin, K.; Lee, H. Structure Transition and Tuning Pattern in the Double (Tetramethylammonium Hydroxide + Gaseous Guests) Clathrate Hydrates. J. Phys. Chem. B 2007, 111 (34), 10224-10230. https://doi.org/10.1021/jp073910c.

[CHO 19] Choudhary, N.; Chakrabarty, S.; Roy, S.; Kumar, R. A Comparison of Different Water Models for Melting Point Calculation of Methane Hydrate Using Molecular Dynamics Simulations. Chem. Phys. 2019, 516, 6-14. https://doi.org/10.1016/j.chemphys.2018.08.036.

[CON 09] Conrad, H.; Lehmkühler, F.; Sternemann, C.; Sakko, A.; Paschek, D.; Simonelli, L.; Huotari, S.; Feroughi, O.; Tolan, M.; Hämäläinen, K. Tetrahydrofuran Clathrate Hydrate Formation. Phys. Rev. Lett. 2009, 103 (21), 218301. https://doi.org/10.1103/PhysRevLett.103.218301.

[COR 13] Corsetti, F.; Fernández-Serra, M.-V.; Soler, J. M.; Artacho, E. Optimal Finite-Range

Atomic Basis Sets for Liquid Water and Ice. Journal of Physics: Condensed Matter 2013, 25 (43), 435504. https://doi.org/10.1088/0953-8984/25/43/435504.

[COS 15] Costandy, J.; Michalis, V. K.; Stubos, A. K.; Tsimpanogiannis, I. N.; Economou, I. G. Atomistic Simulations of Clathrate Hydrates. In Proceedings of the 4th International Gas Processing Symposium; Elsevier, 2015; pp 351-359. https://doi.org/10.1016/B978-0-444-63461-0.50036-5.

[COX 14] Cox, S. J.; Towler, M. D.; Alfè, D.; Michaelides, A. Benchmarking the Performance of Density Functional Theory and Point Charge Force Fields in Their Description of SI Methane Hydrate against Diffusion Monte Carlo. The Journal of Chemical Physics 2014, 140 (17), 174703.

[DAV 11] Davy, H.; The Bakerian Lecture. On some of the combination of oxymuriatic gas and oxygen, and on the chemical relations of these principles, to inflammable bodies, Philos.Trans. R. Soc. London, 1811; 101; 1-35.

[DAV 72] Davidson, D. W.; Garg, S. K. The Hydrate of Hexafluorophosphoric Acid. Canadian Journal of Chemistry 1972, 50 (21), 3515-3520. https://doi.org/10.1139/v72-565.

[DAV 81] Davidson, D. W.; Calvert, L. D.; Lee, F.; Ripmeester, J. A. Hydrogen Fluoride Containing Isostructural Hydrates of Hexafluorophosphoric, Hexafluoroarsenic and Hexafluoroantimonic Acids. Inorg. Chem. 1981, 20 (7), 2013-2016. https://doi.org/10.1021/ic50221a016.

[DES 04] Desmedt, A.; Stallmach, F.; Lechner, R. E.; Cavagnat, D.; Lassègues, J.-C.; Guillaume, F.; Grondin, J.; Gonzalez, M. A. Proton Dynamics in the Perchloric Acid Clathrate Hydrate HClO4?5.5H2O. J. Chem. Phys. 2004, 121 (23), 11916-11926. https://doi.org/10.1063/1.1819863.

[DES 10] Desmedt A., Diffusion inélastique des neutrons. EDP Sciences 2010; 10; 545- 562.

[DES 13] Desmedt, A.; Lechner, R. E.; Lassegues, J.-C.; Guillaume, F.; Cavagnat, D.; Grondin, J. Hydronium Dynamics in the Perchloric Acid Clathrate Hydrate. Solid State Ion. 2013, 252, 19-

25. https://doi.org/10.1016/j.ssi.2013.06.004.

[DES 15] Desmedt, A.; Martin-Gondre, L.; Nguyen, T. T.; Pétuya, C.; Barandiaran, L.; Babot, O.; Toupance, T.; Grim, R. G.; Sum, A. K. Modifying the Flexibility of Water Cages by Co-Including Acidic Species within Clathrate Hydrate. J. Phys. Chem. C 2015, 119 (16) 8904–8911. https://doi.org/10.1021/jp511826b.

[DES 18] Desplanche S., De l'étude fondamentale d'hydrates d'acide fort par spectroscopie de vibration et de relaxation à l'application de leur super-conductivité protonique pour le développement d'une micropile à combustible, 2018, Thèse de l'Université de Bordeaux.

[DIC 95] Dickens, G. R.; O'Neil, J. R.; Rea, D. K.; Owen, R.M., Dissociation of oceanic methane hydrates as a cause of the carbon isotope excursion at the end of the Paleocene. Paleoceanography, 1995, 10 (6), 965-971.

[DIO 04] Dion, M.; Rydberg, H.; Schröder, E.; Langreth, D. C.; Lundqvist, B. I. Van Der Waals Density Functional for General Geometries. Phys. Rev. Lett. 2004, 92 (24), 246401. https://doi.org/10.1103/PhysRevLett.92.246401.

[DIP 91] Dippel Th., Kreuer K.D., Proton transport mechanism in concentrated aqueous solutions and solid hydrates of acids. Solid State Ionic 1991; 46; 3-9.

[DYA 99] Dyadin Y.A., Larionov E.G., Aladko E.Y., Manakov A.Y., Zhurko F.V., Mikina T.V., Komarov V.Y., Grachev E.V. Clathrate formation in water-noble gas (Hydrogen) systems at high pressures, Journal of Structural Chemistry 1999; 40; 790-795.

[FOW 40] Fowler, D. L.; Loebenstein, W. V.; Pall, D. B.; Kraus, Charles A., Some Unusual Hydrates of Quaternary Ammonium Salts, Journal of the American Chemical Society 1940 62 (5), 1140-1142. DOI: 10.1021/ja01862a039

[GIL 16] Gillan, M. J.; Alfè, D.; Michaelides, A. Perspective: How Good Is DFT for Water? The Journal of Chemical Physics 2016, 144 (13), 130901. https://doi.org/10.1063/1.4944633.

[GRI 10] Grimme, S.; Antony, J.; Ehrlich, S.; Krieg, H. A Consistent and Accurate Ab Initio

Parametrization of Density Functional Dispersion Correction (DFT-D) for the 94 Elements H-Pu. The Journal of Chemical Physics 2010, 132 (15), 154104. https://doi.org/10.1063/1.3382344.

[GRO 08] de Grotthuss, C. J. T. Memoir on the Decomposition of Water and of the Bodies That It Holds in Solution by Means of Galvanic Electricity. Biochimica et Biophysica Acta (BBA) - Bioenergetics 2006, 1757 (8), 871-875. https://doi.org/10.1016/j.bbabio.2006.07.004.

[HES 07] Hester, K. C.; Huo, Z.; Ballard, A. L.; Koh, C. A.; Miller, K. T.; Sloan, E. D. Thermal Expansivity for SI and SII Clathrate Hydrates. J. Phys. Chem. B 2007, 111 (30), 8830–8835. https://doi.org/10.1021/jp0715880.

[HIR 15] Hiratsuka, M.; Ohmura, R.; Sum, A. K.; Alavi, S.; Yasuoka, K. A Molecular Dynamics Study of Guest-Host Hydrogen Bonding in Alcohol Clathrate Hydrates. Phys. Chem. Chem. Phys. 2015, 17 (19), 12639-12647. https://doi.org/10.1039/C4CP05732E.

[HOH 64] Hohenberg, P.; Kohn, W. Inhomogeneous Electron Gas. Phys. Rev. 1964, 136 (3B), B864-B871. https://doi.org/10.1103/PhysRev.136.B864.

[HUAN 88] Huang T.H., Davis E., Frese U., Stimming U., Proton Mobility in Liquid and Frozen Perchloric Acid Hydrate (1:5.5): NMR and Conductivity Measurements, J. Phys. Chem. 1988; 92; 6874-6876.

[IRE 04] Ireta, J.; Neugebauer, J.; Scheffler, M. On the Accuracy of DFT for Describing Hydrogen Bonds: Dependence on the Bond Directionality. J. Phys. Chem. A 2004, 108 (26), 5692-5698. https://doi.org/10.1021/jp0377073.

[JEF 84] Jeffrey, G. A. Hydrate Inclusion Compounds. Journal of Inclusion Phenomena 1984, 1 (3), 211-222. https://doi.org/10.1007/BF00656757.

[KAR 74] Karelin, A. I.; Grigorovich, Z. I.; Rosolovskii, V. Ya. Vibrational Spectra of perchloric acid-I. Gaseous and liquid HClO4 and DClO4, Spectro Chimica Acta, 1974 vol.31A, pp.765 to 775.

[KHA 19] Khan, M. N.; Peters, C. J.; Koh, C. A. Desalination Using Gas Hydrates: The Role of Crystal Nucleation, Growth and Separation. Desalination 2019, 468, 114049. https://doi.org/10.1016/j.desal.2019.06.015.

[KLI 11] Klimeš, J.; Bowler, D. R.; Michaelides, A. Van Der Waals Density Functionals Applied to Solids. Phys. Rev. B 2011, 83 (19), 195131. https://doi.org/10.1103/PhysRevB.83.195131.

[KOH 07] Koh, C. A.; Sloan, E. D. Natural Gas Hydrates: Recent Advances and Challenges in Energy and Environmental Applications. AIChE J. 2007, 53 (7), 1636-1643. https://doi.org/10.1002/aic.11219.

[KOH 65] Kohn, W.; Sham, L. J. Self-Consistent Equations Including Exchange and Correlation Effects. Phys. Rev. 1965, 140 (4A), A1133-A1138. https://doi.org/10.1103/PhysRev.140.A1133.

[KOH 90] Koh, C. A.; Sloan, E. D. Natural Gas Hydrates: Recent Advances and Challenges in Energy and Environmental Applications. AIChE J. 2007, 53 (7), 1636-1643. https://doi.org/10.1002/aic.11219.

[KOP 64] Koppers Co., " Potable Water from Sea Water by the Hydrate Process ", Office of Saline Water, Research Develop. Progress Report No. 90, 1964.

[KRE 04] Kreuer, K.-D.; Paddison, S. J.; Spohr, E.; Schuster, M. Transport in Proton Conductors for Fuel-Cell Applications: Simulations, Elementary Reactions, and Phenomenology. Chem. Rev. 2004, 104 (10), 4637-4678. https://doi.org/10.1021/cr020715f.

[KRE 82] Kreuer, K.-D; Prof. Dr. Rabenau, A.; Dr. Weppner, W. Vehicle Mechanism, A New Model for the Interpretation of the Conductivity of Fast Proton Conductors. 1982, 21(3), 208-209. doi:10.1002/anie.198202082.

[KRE 96] Kresse, G.; Furthmüller, J. Efficient Iterative Schemes for Ab Initio Total-Energy Calculations Using a Plane-Wave Basis Set. Phys. Rev. B 1996, 54 (16), 11169-11186. https://doi.org/10.1103/PhysRevB.54.11169.

[KRE 96] Kreuer, K.-D. Proton Conductivity: Materials and Applications. Chemistry of Materials 1996, 8 (3), 610-641. https://doi.org/10.1021/cm950192a.

[KVE 01] Kvenvolden K. A., Lorenson T. D., The global occurrence of natural gas hydrates, in Natural Gas Hydrates: Occurrence, Distribution, and Detection, Geophys. Monogr. Ser., vol. 124, edited by C. K. PAULL AND W. P. DILLON, 3-18, AGU, Washington, D. C, 2001.

[LAN 05] Langreth, D. C.; Dion, M.; Rydberg, H.; Schröder, E.; Hyldgaard, P.; Lundqvist, B. I. Van Der Waals Density Functional Theory with Applications: Van Der Waals DFT. Int. J. Quantum Chem. 2005, 101 (5), 599-610. https://doi.org/10.1002/qua.20315.

[MAK 05] Makino, T.; Sugahara, T.; Ohgaki, K. Stability Boundaries of Tetrahydrofuran + Water System. J. Chem. Eng. Data 2005, 50 (6), 2058–2060. https://doi.org/10.1021/je0502694.

[MET 21] Métais, C.; Petuya, C.; Espert, S.; Ollivier, J.; Martin-Gondre, L.; Desmedt, A. Nitrogen Hydrate Cage Occupancy and Bulk Modulus Inferred from Density Functional Theory-Derived Cell Parameters. J. Phys. Chem. C 2021, 125 (11), 6433-6441. https://doi.org/10.1021/acs.jpcc.1c00244.

[MOO 87] Mootz, D.; Oellers, E.-J.; Wiebcke, M. First Examples of Type I Clathrate Hydrates of Strong Acids: Polyhydrates of Hexafluorophosphoric, Tetrafluoroboric, and Perchloric. J. Am. Chem. Soc. 1987, No. 109, 1200-1202.

[MOO 90] Mootz, D.; Seidel, R. Polyhedral Clathrate Hydrates of a Strong Base: Phase Relations and Crystal Structures in the System Tetramethylammonium Hydroxide-Water. J Incl Phenom Macrocycl Chem 1990, 8 (1-2), 139-157. https://doi.org/10.1007/BF01131293.

[PEL 03] Pelletier, M. J. Quantitative Analysis Using Raman Spectrometry. Appl Spectrosc 2003, 57 (1), 20A-42A. https://doi.org/10.1366/000370203321165133.

[PER 96] Perdew, J. P.; Burke, K.; Ernzerhof, M. Generalized Gradient Approximation Made Simple. Phys. Rev. Lett. 1996, 77 (18), 3865-3868. https://doi.org/10.1103/PhysRevLett.77.3865.

[PER 97] Perdew, J. P.; Burke, K.; Ernzerhof, M. Generalized Gradient Approximation Made Simple", Phys. Rev. Lett., 1997, 78, 1396.

[PET 17 a] Pétuya-Poublan, C. "Etude de la stabilité, de l'occupation des cages et de la sélectivité moléculaire des hydrates de gaz par spectroscopie Raman." Chimie-Physique [physics.chem-ph]. Université de Bordeaux. 2017, Français.

[PET 17 b] Petuya, C.; Damay, F.; Talaga, D.; Desmedt, A. Guest Partitioning in Carbon Monoxide Hydrate by Raman Spectroscopy. J. Phys. Chem. C., 2017, 121, 13798-13802.

[PET 19] Pétuya, C.; Martin-Gondre, L.; Aurel, P.; Damay, F.; Desmedt, A. Unraveling the Metastability of the SI and SII Carbon Monoxide Hydrate with a Combined DFT-Neutron Diffraction Investigation. J. Chem. Phys. 2019, 150 (18), 184705. https://doi.org/10.1063/1.5093202.

[PRA 07] Prasad, P. S. R.; Shiva Prasad, K.; Thakur, N. K. Laser Raman Spectroscopy of THF Clathrate Hydrate in the Temperature Range 90-300K. Spectrochim. Acta. A. Mol. Biomol. Spectrosc. 2007, 68 (4), 1096-1100. https://doi.org/10.1016/j.saa.2007.06.049.

[PRE07] Numerical Recipes: The Art of Scientific Computing, 3rd ed.; Press, W. H., Ed.; Cambridge University Press: Cambridge, UK?; New York, 2007.

[PRO 01] Prokopowicz, A.; Opallo, M. Electrical and Electrochemical Processes in Solid Tetrabutylammonium Hydroxide Hydrate. Solid State Ion. 2001, 145 (1-4), 407-413. https://doi.org/10.1016/S0167-2738(01)00937-7.

[RAT 84] Ratcliffe, C. I.; Irish, D. E. Vibrational Spectral Studies of Solutions at Elevated Temperatures and Pressures. VI. Raman Studies of Perchloric Acid. Can. J. Chem. 1984, 62 (6), 1134-1144. https://doi.org/10.1139/v84-187.

[RIP 88] Ripmeester, J. A.; Ratcliffe, C. I.; Tse, J. S. The Nuclear Magnetic Resonance of 129Xe Trapped in Clathrates and Some Other Solids. J. Chem. Soc., Faraday Trans. 1 1988, 84 (11), 3731. https://doi.org/10.1039/f19888403731.

[ROD 10] Rodionova, T.; Komarov, V.; Lipkowski, J.; Kuratieva, N. The Structure of the Ionic Clathrate Hydrate of Tetrabutylammonium Valerate (C4H9)4NC4H9CO2·39.8H2O. New J. Chem. 2010, 34 (3), 432. https://doi.org/10.1039/b9nj00530g.

[ROM 09] Román-Pérez, G.; Soler, J. M. Efficient Implementation of a van Der Waals Density Functional: Application to Double-Wall Carbon Nanotubes. Phys. Rev. Lett. 2009, 103 (9), 096102. https://doi.org/10.1103/PhysRevLett.103.096102.

[ROM 10] Román-Pérez, G.; Moaied, M.; Soler, J. M.; Yndurain, F. Stability, Adsorption, and Diffusion of CH 4 , CO 2 , and H 2 in Clathrate Hydrates. Phys. Rev. Lett. 2010, 105 (14), 145901. https://doi.org/10.1103/PhysRevLett.105.145901.

[SHI 10] Shin, K.; Cha, J.-H.; Seo, Y.; Lee, H. Physicochemical Properties of Ionic Clathrate Hydrates. Chem. - Asian J. 2010, 5, 22 - 34. https://doi.org/10.1002/asia.200900219

[SHI 11] Shin, K.; Lee, W.; Cha, M.; Koh, D.-Y.; Choi, Y. N.; Lee, H.; Son, B. S.; Lee, S.; Lee, H. Thermal Expansivity of Ionic Clathrate Hydrates Including Gaseous Guest Molecules. J. Phys. Chem. B 2011, 115 (5), 958–963. https://doi.org/10.1021/jp110737q.

[SIMUNE] private communications by the SIMUNE group, see also https://www.simuneatomistics.com/siesta-pro/siesta-pseudos-and-basis-database/].

[SLO 03] Sloan, E. D. Fundamental Principles and Applications of Natural Gas Hydrates. Nature 2003, 426 (6964), 353-359. https://doi.org/10.1038/nature02135.

[SLO 08] Sloan, E. D.; Koh, C. A. Clathrate Hydrates of Natural Gases, 3rd ed.; Taylor & Francis-CRC Press: Boca Raton, FL, 2008.

[SLO 98] Sloan, E.D. Gas hydrates: review of physical/chemical properties. Energy & Fuels, 1998, 12, 191-196.

[SOL 02] Soler, J. M.; Artacho, E.; Gale, J. D.; García, A.; Junquera, J.; Ordejón, P.; Sánchez-Portal, D. The SIESTA Method for Ab Initio Order- N Materials Simulation. J. Phys.: Condens. Matter 2002, 14 (11), 2745-2779. https://doi.org/10.1088/0953-8984/14/11/302.

[SUM 09] Sum, A. K.; Koh, C. A.; Sloan, E. D. Clathrate Hydrates: From Laboratory Science to Engineering Practice. Ind. Eng. Chem. Res. 2009, 48 (16), 7457-7465. https://doi.org/10.1021/ie900679m.

[SUM 97] Sum, A. K.; Burruss, R. C.; Sloan, E. D. Measurement of Clathrate Hydrates via Raman Spectroscopy. J. Phys. Chem. B 1997, 101 (38), 7371-7377. https://doi.org/10.1021/jp970768e.

[SUN 17] Sun, N.; Li, Z.; Qiu, N.; Yu, X.; Zhang, X.; Li, Y.; Yang, L.; Luo, K.; Huang, Q.; Du, S. Ab Initio Studies on the Clathrate Hydrates of Some Nitrogen- and Sulfur-Containing Gases. J. Phys. Chem. A 2017, 121 (13), 2620-2626. https://doi.org/10.1021/acs.jpca.6b11850.

[TSE 87] Tse, J. S. Thermal Expansion of the Clathrate Hydrates of Ethylene Oxide and Tetrahydrofuran. J. Phys. Colloques 1987, 48 (C1), C1-543-C1-549. https://doi.org/10.1051/jphyscol:1987174.

[UCH 02] Uchida, T.; Ebinuma, T.; Takeya, S.; Nagao, J.; Narita, H. Effects of Pore Sizes on Dissociation Temperatures and Pressures of Methane, Carbon Dioxide, and Propane Hydrates in Porous Media. J. Phys. Chem. B 2002, 106 (4), 820-826. https://doi.org/10.1021/jp012823w.

[UCH 99] Uchida, T.; Hirano, T.; Ebinuma, T.; Narita, H.; Gohara, K.; Mae, S.; Matsumoto, R. Raman Spectroscopic Determination of Hydration Number of Methane Hydrates. AIChE J. 1999, 45 (12), 2641-2645. https://doi.org/10.1002/aic.690451220.

[VAL 16] Vlasic, T. M.; Servio, P.; Rey, A. D. Atomistic Modeling of Structure II Gas Hydrate Mechanics: Compressibility and Equations of State. AIP Advances 2016, 6 (8), 085317. https://doi.org/10.1063/1.4961728.

[WIE 86] Wiebcke, M.; Mootz, D. Die Isotypen Phasen HEF6 · 5H2O · HF (E = P, As, Sb): Neubestimmung Der Strukturen an Einkristallen. 1986, 177 (1-4), 291-300. https://doi.org/10.1524/zkri.1986.177.14.291.

[WU 05] Wu, C.-C.; Lin, C.-K.; Chang, H.-C.; Jiang, J.-C.; Kuo, J.-L.; Klein, M. L. Protonated

Clathrate Cages Enclosing Neutral Water Molecules: H+(H2O)21 and H+(H2O)28. J. Chem. Phys. 10.

[YAN 19] Yang L., Liu Y., Zhang H., Xiao B., Guo X., Wei R., Xu L., Sun L., Yu B., Leng S., Li Y., The status of exploitation techniques of natural gas hydrate", Chinese J. Chem. Engineering, 2019, 27, 2133-2147.

[ZHA 18] Zhang, X.; Qiu, N.; Huang, Q.; Zha, X.; He, J.; Li, Y.; Du, S. Theoretical Studies on Microstructures, Stabilities and Formation Conditions of Some Sour Gas in the Type I, II, and H Clathrate Hydrates. J. Mol. Struct. 2018, 1153, 292-298. https://doi.org/10.1016/j.molstruc.2017.09.087.

[ZHE 20] Zheng, J.; Yang, M. Experimental Investigation on Novel Desalination System via Gas Hydrate. Desalination 2020, 478, 114284. https://doi.org/10.1016/j.desal.2019.114284.